ESCOLA POLITÉCNICA DA UNIVERSIDADE DE SÃO PAULO
WEIGLE EMANUEL CARVALHO

MODELO PARA ESCOAMENTO BLOCADO DE HEXAFLUORETO DE URÂNIO MONOFÁSICO EM PLACAS DE ORIFÍCIO DE RESTRIÇÃO ESPESSAS DE CANTO VIVO

SÃO PAULO

2023

ESCOLA POLITÉCNICA DA UNIVERSIDADE DE SÃO PAULO

WEIGLE EMANUEL CARVALHO

MODELO PARA ESCOAMENTO BLOCADO DE HEXAFLUORETO DE URÂNIO MONOFÁSICO EM PLACAS DE ORIFÍCIO DE RESTRIÇÃO ESPESSAS DE CANTO VIVO

Versão Original

Dissertação apresentada à Escola Politécnica da Universidade de São Paulo como requisito para obtenção do título de Mestre em Ciências.

SÃO PAULO

2023

ESCOLA POLITÉCNICA DA UNIVERSIDADE DE SÃO PAULO
WEIGLE EMANUEL CARVALHO

MODELO PARA ESCOAMENTO BLOCADO DE HEXAFLUORETO DE URÂNIO MONOFÁSICO EM PLACAS DE ORIFÍCIO DE RESTRIÇÃO ESPESSAS DE CANTO VIVO

Dissertação apresentada à Escola Politécnica da Universidade de São Paulo como requisito para obtenção do título de Mestre em Ciências.

Área de concentração: Engenharia Química

Orientador: Prof. Dr. Cláudio Augusto Oller do Nascimento

Coorientador: Prof. Dr. Ernani Vitillo Volpe

SÃO PAULO
2023

POLYTECHNIC SCHOOL OF THE UNIVERSITY OF SÃO PAULO
WEIGLE EMANUEL CARVALHO

A MODEL FOR CHOKED FLOW OF SINGLE-PHASE URANIUM HEXAFLUORIDE THROUGH THICK SQUARE-EDGED RESTRICTION ORIFICE PLATES

São Paulo

2023

POLYTECHNIC SCHOOL OF THE UNIVERSITY OF SÃO PAULO
WEIGLE EMANUEL CARVALHO

A MODEL FOR CHOKED FLOW OF SINGLE-PHASE URANIUM HEXAFLUORIDE THROUGH THICK SQUARE-EDGED RESTRICTION ORIFICE PLATES

Original Version

Master Dissertation presented to Polytechnic School of University of São Paulo as a requirement to obtain the title of Master of Science.

São Paulo
2023

POLYTECHNIC SCHOOL OF THE UNIVERSITY OF SÃO PAULO
WEIGLE EMANUEL CARVALHO

A MODEL FOR CHOKED FLOW OF SINGLE-PHASE URANIUM HEXAFLUORIDE THROUGH THICK SQUARE-EDGED RESTRICTION ORIFICE PLATES

Master Dissertation presented to Polytechnic School of University of São Paulo as a requirement to obtain the title of Master of Science.

Concentration area: Chemical Engineering

Advisor: Prof. Dr. Cláudio Augusto Oller do Nascimento

Co-advisor: Prof. Dr. Prof. Dr. Ernani Vitillo Volpe

São Paulo
2023

Este exemplar foi revisado e corrigido em relação à versão original, sob responsabilidade única do autor e com a anuência de seu orientador.

São Paulo, 04 de setembro de 2023

Assinatura do autor: Weigle Emanuel Carvalho

Assinatura do orientador:

Catalogação-na-publicação

Carvalho, Weigle
A MODEL FOR CHOKED FLOW OF SINGLE-PHASE URANIUM HEXAFLUORIDE THROUGH THICK SQUARE-EDGED RESTRICTION ORIFICE PLATES / W. Carvalho -- versão corr. -- São Paulo, 2023.
76 p.

Dissertação (Mestrado) - Escola Politécnica da Universidade de São Paulo. Departamento de Engenharia Química.

1.Choked flow 3.Compressible flow 4.Discharge coefficient 5.Computational fluid dynamics I.Universidade de São Paulo. Escola Politécnica. Departamento de Engenharia Química II.t.

For my beloved wife who always encouraged me, believed me, and loved me,

Daniele Rodrigues Brito Carvalho.

AGRADECIMENTOS

A Deus que nos guia a sermos indivíduos melhores.

Ao Prof. Dr. Cláudio Augusto Oller do Nascimento, por aceitar ser meu orientador, pelas ideias inovadoras, demais contribuições e acompanhamento do trabalho.

Ao Prof. Dr. Ernani Vitillo Volpe, pelo conhecimento técnico passado tanto sobre dinâmica dos fluidos computacional quanto sobre de escoamento compressível.

À minha esposa, Daniele Rodrigues Brito Carvalho, pelo amor, compreensão e apoio, minha profunda e eterna gratidão.

À minha filha bebê Helena Brito Carvalho, que me deu mais motivação na vida e na conclusão do mestrado.

Aos meus pais, Jane Carvalho e Nadir Carvalho, e irmã, Mayla Carvalho, pelos ensinamentos da vida que sempre estarão guardados comigo, pelo carinho e companheirismo mesmo à distância e pelos bons momentos juntos.

Aos meus amigos Nikolas Barboza, Antonio Gomes, Ana Carolina Lima e Egle Martins e Erik Brito, que sempre foram fiéis companheiros, me incentivando e apoiando em decisões como esta, além das conversas descontraídas.

À toda equipe do Laboratório de Alta Pressão, em especial aos companheiros Adriana Velosa, Amanda, Andressa Lima, Cleiton Beraldo, Gabriel Bressan, José Curvelo, Lélia Soares, Leonardo de Oliveira, Luis Follegatti, Maria Gomez, Matheus de Holanda, Murilo Alcântara, Pedro Machado, Raquel Costa, Rodrigo Ramos e Victor Sumikawa, que se tornaram colegas ou amigos durante um momento cheio de desafios como o mestrado. A todos agradeço pelo companheirismo e pelas conversas sobre dúvidas minhas no mestrado ou temas descontraídos, muitas vezes acompanhadas de um bom café. Ao Adriano Silvares, ao Cleiton Beraldo, e ao Leonardo de Oliveira mais uma vez, por terem analisado meu trabalho, contribuindo para melhoras deste. Aos Professores Paiva e Ardson, pelos conhecimentos adquiridos das disciplinas por eles ministrados, pela abertura de diálogo e contribuição de ideias. Ao colega engenheiro Natan Patussi pela contribuição de ideias.

Ao Núcleo de Dinâmica e Fluidos da Escola Politécnica da USP pela disponibilização dos recursos computacionais para simulações em dinâmica dos fluidos computacional que foram realizadas durante nesse trabalho.

Para todos os demais parentes e amigos que contribuíram de alguma maneira para a realização deste trabalho de forma direta ou indireta.

Ao Departamento de Engenharia Química da Escola Politécnica da Universidade de São Paulo, pela oportunidade de realização do mestrado.

À Marinha do Brasil, em especial às organizações militares Diretoria de Engenharia Naval (DEN) e Diretoria de Desenvolvimento Nuclear da Marinha (DDNM) e seus respectivos pessoais, pelo desenvolvimento profissional.

“Every brilliant experiment, like every great work of art, starts with an act of imagination.”

(Jonah Lehrer)

RESUMO

Nas principais tecnologias de enriquecimento de urânio, isto é, na separação isotópica deste elemento, este aparece na forma gasosa de hexafluoreto de urânio UF_6. Notaram-se trabalhos envolvendo este fluido que fazem tratamento simplificado sobre o escoamento crítico através de orifícios, seja em elementos restritivos de vazão instalados em cascatas de separação isotópica, na modelagem de escoamento através da estrutura interna de alimentação de ultracentrífugas, ou ainda em casos de estudos de análise de risco envolvendo vazamentos do gás supracitado. O presente trabalho propõe um tratamento mais realista e criterioso sobre este tipo de escoamento, modelando o escoamento para estimar o coeficiente de descarga sob condições de escoamento blocado C_d^* e assim corrigindo a vazão mássica ideal calculada. Dessa forma, aumentando a acurácia de cálculos de vazão nas diversas modelagens possíveis com o UF_6. O objetivo deste trabalho foi o estudo de escoamentos críticos compressíveis e em baixa pressão do gás UF_6 monofásico através de placas de orifício espessas para fins de obtenção de correlação de C_d^*. A dinâmica dos fluidos computacional (*CFD*) foi usada por meio do software Ansys Fluent para resolver numericamente os escoamentos. Dois subconjuntos de 20 modelos geométricos cada foram utilizados. O primeiro subconjunto se refere a escoamentos laminares e o segundo a escoamentos turbulentos com baixo número de Reynolds (maior do que 8000). Assim, um total de 40 casos foram estudados através de 165 simulações, todos em tubulação de diâmetro interno 4,45 cm e com o diâmetro do orifício igual à sua espessura. A variação paramétrica de C_d^* foi guiada pelo planejamento de experimentos computacionais e feita com dois fatores: i) a pressão total a montante do orifício P_0 e ii) a razão entre diâmetro do orifício e diâmetro interno da tubulação β. O modelo de *CFD* proposto pôde ter sua acurácia avaliada indiretamente pela calibração com dados experimentais de casos da literatura similares aos escoamentos estudados, porém com ar como fluido de processo. Além disso as simulações foram testadas quanto à conservação de massa e de entalpia total ao longo do domínio fluido computacional para verificar se a soluções físicas obtidas têm amparo teórico. Para o subconjunto turbulento, C_d^* apresentou comportamento errático periódico em relação ao fator (parâmetro) P_0, o que impossibilitou a obtenção de qualquer ajuste com as funções testadas. Porém, apresentou bom ajuste polinomial quanto ao fator β e foi testado com polinômios de ordens 1 a 8, pelo método dos mínimos quadrados para definição dos parâmetros ótimos. O melhor ajuste foi o polinômio de sexto grau com base no erro padrão de regressão s^2 igual a $7.89 \bullet 10^{-8}$. Mas, para evitar *overfitting*, o polinômio de segundo grau com $s^2 = 28.6 \bullet 10^{-8}$ consistiu na correlação obtida de C_d^* com β.

Palavras-chave: Escoamento blocado; Escoamento compressível; Placa de orifício espessa; Coeficiente de descarga; Dinâmica dos Fluidos Computacional.

ABSTRACT

In the main technologies of uranium enrichment, i.e., the isotopic separation of this element, it appears as gaseous uranium hexafluoride UF_6. Simplified treatment on the critical flow of UF_6 through orifices was noted in several works, either in restrictive flow elements installed in isotopic separation cascades, in the modeling of flow through the internal structure of gas centrifuge feed, or even in cases of analysis studies of risk involving leaks of the gas. The present work proposes a more realistic and careful treatment of this type of flow, by modeling the flow to estimate the discharge coefficient under choked flow conditions C_d^* and thereby correcting the ideal mass flow rate. Thus, increasing the accuracy of flow calculations in the various possible types of modeling with UF_6. The goal of this work was to study the compressible critical flow at low pressure of single-phase UF_6 gas through thick orifice plates in order to obtain a correlation for C_d^*. Computational fluid dynamics (CFD) was used through Ansys Fluent software to solve the flows numerically. Two subsets of 20 different geometric models each were used. The first subset refers to laminar flows and the second to turbulent flows with low Reynolds number (higher than 8000). Thus, a total of 40 cases were studied through 165 simulations. All of the orifice plate models were set in a 4.45 cm internal diameter pipe and had the orifice diameter equal to the orifice thickness. The parametric variation of C_d^* was guided by the design of computer experiments and was performed with two factors: i) the upstream total pressure P_0, and ii) the orifice-to-pipe diameter ratio β. The CFD method herein proposed could have its accuracy indirectly asserted by calibration using literature experimental data from cases similar to the studied flows but with air as the process fluid. In addition, the simulations were tested for the conservation of mass and total enthalpy throughout the computational fluid domain to verify whether the physical solution obtained has theoretical support. For the turbulent subset, C_d^* presented periodic erratic behavior with respect to the P_0 factor (parameter). This resulted in observations without direct method to obtain any proper fitting among the tested functions. C_d^* showed good polynomial fit for the β factor and it was tested with polynomials of degrees 1 to 8. The least-squares method was used to define the optimal parameters. The best fit was the sixth-degree polynomial with minimum squared standard error of the regression s^2 equals to $7.89 \cdot 10^{-8}$. But the second-degree polynomial with $s^2=28.6 \cdot 10^{-8}$ consisted on the actual obtained correlation of C_d^* with β.

Keywords: Choked flow; Compressible flow; Thick orifice plate; Discharge coefficient; Computational fluid dynamics.

LIST OF FIGURES

LIST OF TABLES

LIST OF ABBREVIATIONS AND ACRONYMS

2D	Two-Dimensional
3D	Three-Dimensional
AS	Axisymmetric
ASME	American Society of Mechanical Engineers
AUSM	Advection Upstream Splitting Method
BC	Boundary Condition(s)
CFD	Computational Fluid Dynamics
CTMSP	*Centro Tecnológico da Marinha em São Paulo*, Portuguese abbreviation for "Technology Center of the Brazilian Navy in São Paulo"
DDNM	*Diretoria de Desenvolvimento Nuclear da Marinha*, Portuguese abbreviation for "Directorate of Nuclear Development of the Brazilian Navy"
DACE	Design and Analysis of Computer Experiments
DB	Density-based (Solver)
DNS	Direct Numerical Simulation
DOE	Design of Experiments
FFT	Fast-Fourier Transform
INB	*Indústrias Nucleares do Brasil*, Portuguese abbreviation for "Nuclear Industries of Brazil"
lam	Laminar
LAP	*Laboratório de Alta Pressão,* Portuguese abbreviation for "High Pressure Lab"
LEU	Low-Enriched Uranium
LHS	Latin Hypercube Sampling
NS	Navier-Stokes
PB	Pressure-based (Solver)
RANS	Reynolds-averaged Navier-Stokes
turb	Turbulent
VOF	Volume of Fluid

LIST OF SYMBOLS

$(\overline{\ })$	Superscript denoting it is the time-averaged value of the property
A^*	Critical value of orifice area
AR	Aspect ratio of the cell
c	Speed of sound in the gas
C_d	Discharge coefficient
C_d^*	Discharge coefficient under choked flow conditions
cos	Cosine function
c_P	Specific heat capacity at constant pressure
c_V	Specific heat capacity at constant volume
C^*	Critical value of the coefficient used in discharge equation by Fliegner
D	Internal diameter of the pipe
d	Diameter of the orifice
$\vec{d}_{Pf,i}$	Distance vector from the centroid of owner cell to the centroid of its i-th face
$\vec{d}_{PN,i}$	Distance vector from the centroid of owner cell to the centroid of its closest neighbor through the i-th face of owner cell
e_{21}^{extr}	Extrapolated error based on the fine and medium grids
ES	Equiangle skewness
F	Blending function
f	Grid refinement factor
GCI_{21}	Grid convergence index based on the fine (1) and medium (2) grids
H	Specific enthalpy
h_0	Total enthalpy
K	Specific kinetic energy
k	Thermal conductivity
Kn	Knudsen number
L	Longest side length of the cell
L_c	Characteristic length
L_D	Downstream domain length
L_U	Upstream domain length
M	Molar mass
m	Degree of the fitting polynomial
Ma	Mach number
$\dot{m}$	Mass flow rate

$\dot{m}_{theoretical}$	Theoretical mass flow rate considering isentropic and adiabatic flow
N	Number of sides of the i-th face
n	Number of simulations (cases)
n_d	Number of cells comprising the flow domain
n_f	Number of factors
$\vec{n}_{f,i}$	Normal vector of i-th face of the cell
n_p	Number of cases to be simulated
OQ	Orthogonal quality
P	Static pressure
P_0	Inlet (upstream) total pressure
P_b	Back pressure or static pressure at downstream conditions
P_b/P_0	Back-to-inlet pressure ratio or downstream-to-upstream pressure ratio
P_j	Pressure of the gas jet at the orifice
Q	Heat normal to the wall boundary
q	Order of convergence
R	Universal gas constant
r	Radial coordinate in cylindrical coordinate system
Re	Reynolds number
Re_d	Orifice Reynolds number
r_c	Critical pressure ratio. The maximum pressure ratio P_b/P_0 for choked flow
SST	Shear Stress Transport
S	Shortest side length of the cell
s	Standard error of the regression
T	Absolute temperature
t	Thickness (length) of the orifice
T_0	Inlet total temperature
T_{ef}	Effective temperature.
T_{ref}	Reference temperature
UF_6	Uranium hexafluoride
$\vec{U}$	Local velocity (vector)
V_m	Mean Velocity
u	Velocity axial component
v	Velocity radial component
x	Axial coordinate in cylindrical coordinate system
y	distance to the next surface

Z	Compressibility factor
Greek letters	
α	Coefficient of SST κ-ω model of turbulence
α^*	Coefficient of SST κ-ω model of turbulence
β	Orifice-to-pipe diameter ratio, ($\beta = d/D$)
β^*	Coefficient of SST κ-ω model of turbulence
βi	Coefficient of SST κ-ω model of turbulence
γ	Ratio of specific heats ($\gamma = c_p/c_v$)
ΔS	Entropy change between outlet and inlet of computational flow domain
ε	Error (residual) between C_d^* from simulation and C_d^* from fitting polynomial
θ	Angular or azimuthal coordinate of cylindrical coordinate system
θ_{min}	Minimum internal angle of the i-th face
θ_{max}	Maximum internal angle of the i-th face
$\theta_{\vec{n}_{f,i}\,\vec{d}_{Pf,i}}$	Angle between the $\vec{n}_{f,i}$ and $\vec{d}_{Pf,i}$ vectors
$\theta_{\vec{n}_{f,i}\,\vec{d}_{PN,i}}$	Angle between the $\vec{n}_{f,i}$ and $\vec{d}_{PN,i}$ vectors
κ	Turbulent kinetic energy
λ	Mean free path
μ_0	Reference viscosity
μ	Dynamic viscosity
μ_t	Turbulent viscosity
ρ	Density
ρ_0	Density at conditions of the discharging vessel
ρ_t	Total density
τ	Viscous stress tensor
ω	Specific dissipation rate
σ_κ	Turbulent Prandtl number for κ
σ_ω	Turbulent Prandtl number for ω

SUMMARY

1 INTRODUCTION

Nuclear energy remains worldwide recognized as a clean energy with low emission of carbon dioxide. It is also the energy with the highest ratio of energy per mass of fuel among the currently feasible energy types. Nuclear energy employs uranium fission to the controlled release of energy. However, only uranium isotope U-235 is useful in such energy production, i.e., it is fissile. Other two naturally occurring uranium isotopes are only fissionable: i) the major U-238 (99.2836 % (OECD-NEA & IAEA, 2020) in mass basis), and ii) U-234 (0.0054 % (OECD-NEA & IAEA, 2020)). The difference relies on the required energy of the colliding neutrons – fissionable isotopes require high energy from the colliding neutrons whereas fissile require no energy from them. So that lead to two main problems related to U-235: (a) uranium has very low concentration on earth, and (b) from this content only 0.7110 % (OECD-NEA & IAEA, 2020) consists of U-235.

Therefore, uranium has to be extracted as oxide from the mines, that usually contain less than 20 % of U_3O_8, which is a typical uranium ore. The process of mining just briefly described is only the first on a multistep uranium nuclear fuel open cycle, as presented in Figure 1. The most critical step is that of isotope separation of uranium, also known as uranium enrichment, which is highlighted in red in Figure 1.

Therefore, uranium enrichment consists of separating U-235 from mostly U-238 and traces of U-234, i.e., increasing the concentration of the first and decreasing that of the latter isotopes.

There are several technologies to separate isotopes, and gas diffusion and gas centrifuge processes were the most used to enrich uranium commercially throughout the decades (MAKHIJANI; CHALMERS; SMITH, 2004). Both technologies consist in cascades of separation units. The cascade projects initiated with Cohen when he wrote about the ideal cascade theory (COHEN, 1951). His work was fundamental and theoretical, but it threaded the way to further development in cascade theory. Many authors based their works on Cohen's theory to create cascade modeling closest to real cascades.

One of these many authors was Palkin (1997), who evolved the modeling of isotopic separation cascades. In 2000, another two worth-citing authors Portoghese and Rodrigues (2000) further developed cascade modeling by inputting several experimental parameters in the cascade modeling.

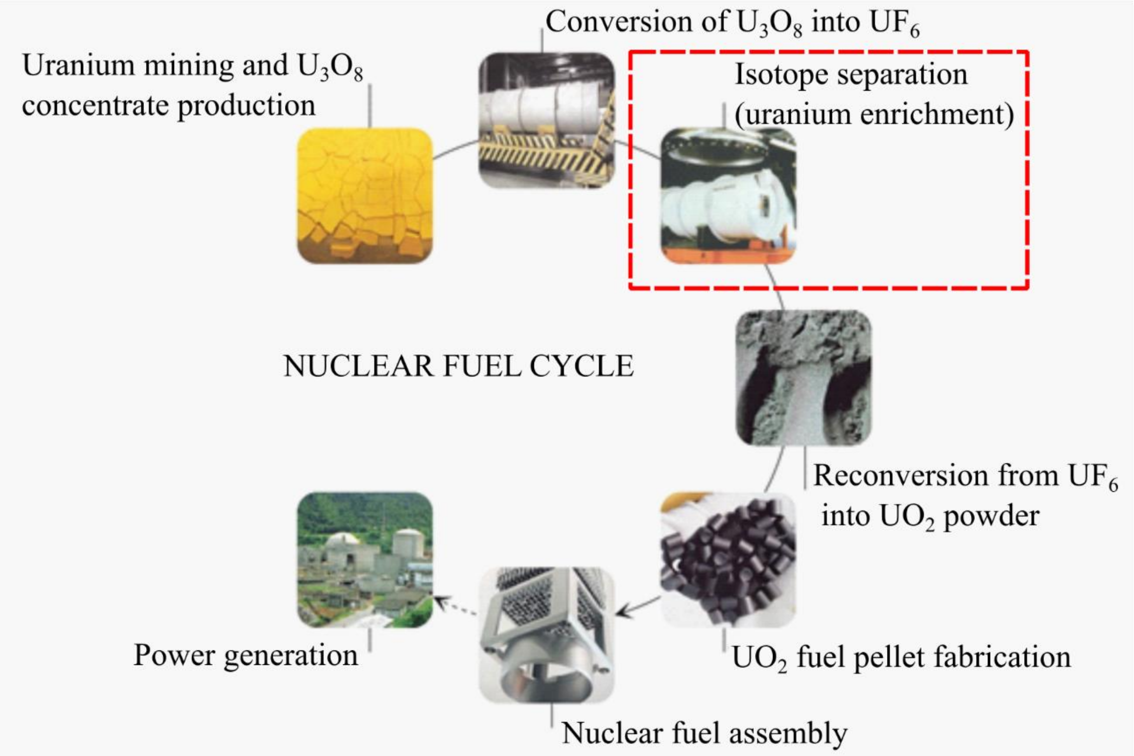

Figure 1 – Nuclear fuel open cycle. Adapted from and with permission of INB (INDÚSTRIAS NUCLEARES DO BRASIL).

One of the latest works on elaborating cascade project calculations was developed by Paula, Migliavacca, and Guardani (2022), and consisted in the modeling of a real-size isotope separation cascade. In this work, each machine was modeled with hydraulic and separation features.

On the background of modeling of isotope separation cascade, many of the works include cascade calculations relating to the flowrate of gaseous UF_6. Furthermore, several of these works also related to C_d^* regarding the flow of the aforementioned gas through orifices. The defining equation for C_d^* shows that it is the ratio between the actual mass flow rate $\dot{m}$ and the isentropic and adiabatic mass flow rate $\dot{m}_{theoretical}$:

$$C_d^* = \frac{\dot{m}}{\dot{m}_{theoretical}} \qquad \text{Equation 1}$$

The foregoing work of Paula, Migliavacca, and Guardani (2022) is such an example as are several other works. But it is noteworthy that the C_d^* of uranium hexafluoride was assumed with little to no criteria, generally considered ideal, i.e., unity. Consequently, the mass flow rate derived from C_d^* could be inaccurate. Also, a recent PhD thesis on more realistic uranium isotope separation cascade calculations (PAULA, 2022) showed that at least a mild gap exists in the literature regarding the determination of C_d^* of UF_6 gas through orifices. In particular, the aforementioned study flow conditions were both compressible and continuous flow under very low pressures.

Thick orifice plates were chosen in this work due to their use throughout isotope separation cascades to provide appreciable pressure drop required in plant operation. Particularly, square-edged orifice plates are the most used in industry due to simplest manufacture. Therefore, thick square-edged orifice plates were used in this study.

2 OBJECTIVES

The main objective of this work is to obtain a correlation for C_d^* of UF_6 gas choked flow through square-edged thick restriction orifices with the following parameters: i) P_0, and ii) β.

The specific objectives of this work are:

- the definition and modeling of the type of flow to be studied regarding rarefaction, compressibility, and flow regime to pass through the orifice.
- the choosing of proper settings of the CFD code regarding the physical process so that the adequate forms of the transport equations and the related boundary conditions (BC) are possible to be numerically solved.
- the calibration of the model with experimental data from similar literature cases to the studied flows asserting the model accuracy.
- the definition of the range of values for the factors so that the studied flows are exactly within the chosen classification with respect to rarefaction, compressibility, and turbulence.
- the performing of a grid refinement study to select a grid with a proper refinement level to be used, resulting in an acceptable discretization error for the calculated C_d^* and minimal computational efforts used.
- the simulation of each case by varying the backpressure P_b so that C_d^* is obtained.
- the fitting of data to obtain a correlation of C_d^* with P_0 and β.

3 LITERATURE REVIEW

3.1 RESTRICTION ELEMENTS

Restrictions consist of a contraction followed by an expansion in the flow area. The flow accelerates during the contraction, causing the pressure to drop. They are subdivided in orifices and nozzles depending on the shape of the inlet.

Types of orifices (a) and nozzles (b) that appear in literature are illustrated Figure 2.

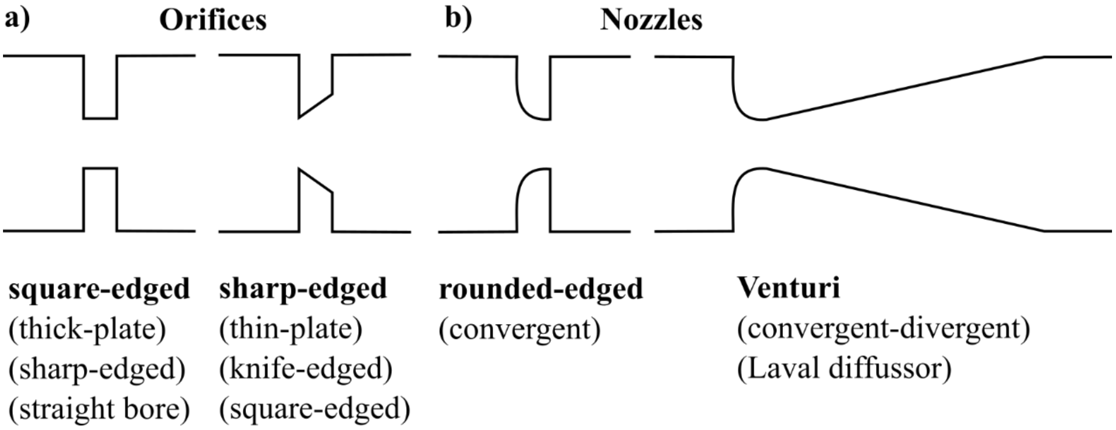

Figure 2 – a) orifices and b) nozzles types in bold with respective synonyms in parentheses. Adapted from on Anderson (1967).

3.2 CHOKED FLOW AND CRITICAL DISCHARGE COEFFICIENT

It might be hard to ascertain who were the pioneer authors regarding the study of choked flow gases through orifices, nozzles, and tubes. In 1839, Saint-Venant and Wantzel (1839) were the first to establish a general form to the equation that describes the discharge of a gas from a reservoir to a lower-pressure receiver through orifices. The authors imposed an adiabatic relation between the pressure and the density of the flowing gas. Hence, they could propose an equation to describe the discharge of the gas through an orifice. The proposed equation was equivalent to Equations 2 and 3, for the mean velocity V_m and mass flow rate $\dot{m}$ of the gas, respectively:

$$\frac{V_m^{2}}{2}=\frac{\gamma}{\gamma-1}\,\frac{P_0}{\rho_0}\left[1-\left(\frac{P_j}{P_0}\right)^{\frac{\gamma-1}{\gamma}}\right]$$ Equation 2

$$\dot{m}=A\sqrt{\frac{2\gamma}{\gamma-1}\,P_0\rho_0\left(\frac{P_j}{P_0}\right)^{\gamma}\left[1-\left(\frac{P_j}{P_0}\right)^{\frac{\gamma-1}{\gamma}}\right]}$$ Equation 3

Where γ is the ratio of specific heats, ρ is density at conditions of the discharging vessel, P_j is the pressure of the jet at the orifice.

The authors also noted that Equation 3 gave the maximum value for the mass flow rate if the pressure in the orifice was that given by Equation 4, i.e., they found the jet-to discharging vessel pressure ratio P that resulted in the maximum flow – the theoretical r_c:

$$r_c=\frac{P_j}{P_0}=\left(\frac{2}{\gamma+1}\right)^{\frac{\gamma}{\gamma-1}} \qquad \text{Equation 4}$$

They also observed that the discharge rate diminished to zero as the pressure of the jet at the orifice exit tended towards zero. This meant the equation predicted no gas would discharge into a vacuum. The origin of such absurd was the use of the erroneous assumption that the pressure of the discharging gas jet was equal to the pressure in the receiving vessel at a distance. The authors also investigated experimentally the air flow through orifices discharging into a receiver maintained at a partial vacuum. The results found include: the gas discharge increased as the downstream-to-upstream pressure ratio P_b/P_0 decreased from 1 to about 0.4, and it remained constant from 0.4 to zero – from that the choked flow was obtained. The authors stressed that, in this last range of P_b/P_0, the pressure of the discharging gas at the orifice exit could not be assumed as equal to the pressure in the receiving vessel. This assumption was generally used in the case of the discharge of water flow into an air-filled reservoir. Rather, they concluded that, as long as the choked flow regime would be maintained, the pressure at the orifice would be about 0.6 times the upstream pressure and would never drop below this value (r_c).

Poncelet (1845) disputed the experimental results of Saint-Venant and Wantzel, as they had the limitation of regarding very small-scale orifices.

Seven years later, Stokes (1846) reviewed the work of Saint-Venant and Wantzel. Stokes agreed with the authors that the pressure at the orifice could not be assumed as equal to the pressure at a distance in the receiving reservoir, if the pressure difference between the reservoirs are considerable.

In 1861, Holtzmann (1861) was apparently the first to discover that the throat velocity at some value of P_b/P_0 was identical in value to that of the local velocity of sound. He also noted that this could be an explanation of the phenomenon of choked flow.

Five years later, Weisbach (1866) did a large amount of work on air flow through orifices and nozzles from pressurized vessels into the atmosphere. Hence, the author could verify experimentally the validity of the observations of Saint-Venant and Wantzel about the stabilization of the flow rate when r_c occurred – the choked flow phenomenon.

Twelve more years, Zeuner (1874) measured the air flow through orifice plates and convergent nozzles in order to test the validity of the theoretical r_c. For the convergent nozzles, the result agreed well with theory. But for the orifice plates, the author did not find any limit in the mass flow rate.

In the same year, Fliegner (1874) added the results of Zeuner to his own results on air flow through thin orifice plates. Hence, he could further prove experimentally the observations of Saint-Venant and Wantzel about choked flow. In addition, Fliegner proposed an empirical equation (Equation 5) based on the total pressure and temperature of the inlet stream, $P_{t,\ inlet}$ and $T_{t,\ inlet}$, and on critical area and coefficient, C*, and A*, respectively. This would only be derived theoretically by Zeuner (1905):

$$\dot{m}=\frac{C_{*}A_{*}P_{t,\ inlet}}{\sqrt{T_{t,\ inlet}}} \qquad \text{Equation 5}$$

In 1877, Fliegner (1877) made experiments on the air flow through a convergent nozzle to determine r_c. The author could measure the pressure at the minimum cross-sectional area in the nozzle using a wall tap. He found that, for constant upstream conditions but varying those downstream, this pressure would remain constant in the supersonic regime. The original observation of Saint-Venant and Wantzel regarding the constancy of the pressure at the orifice during choking was proved correct. The next year, the same author (FLIEGNER, 1878) also experimented several sharp-edged orifices. Fliegner observed that, as the P_b/P_0 decreased, the discharge coefficient C_d increased. The author was probably the first to conjecture that the contracted air jet flowing out from an orifice is not restricted. Unlike the case of a nozzle, the air jet from an orifice is free to expand its cross-sectional area.

In 1885, Wilde (1885) investigated the choked flow of air through square-edged orifice plates with diameter twice the thickness t for two cases. In one case, a reservoir was discharged on a vacuum reservoir. In the second case, the discharge was from a pressurized reservoir to the atmosphere. The author observed that the discharge flow rate in both cases turned constant when the ratio of the pressures of the two reservoirs was about 0.5. Saint-Venant and Wantzel found the reference value of 0.4 for P_b/P_0. The small difference was supposedly due to different manufacturing of the orifices, measuring methods, and systems used. In summary, a further confirmation of the limiting flow phenomenon through orifices and nozzles at low P_b/P_0 had been made by Wilde. Once more the Saint-Venant and Wantzel observation was proven. Therefore, Zeuner, Fliegner and Wilde unanimously confirmed the surprising relationships first pointed out by Saint-

Venant and Wantzel, with results credible enough to be challenged.

Despite researchers performing different experiments since the work of Saint-Venant and Wantzel, no major contribution had been given to the theory of gas flow through orifices until the work of Reynolds (1885). The author analyzed the foregoing work of Wilde and derived equations Equations 2 and 3 for the discharging gas flow through an orifice. He assumed the flow was at steady conditions, so the mass flow rate was constant in any cross-section of a given streamline. Now differently from Saint-Venant and Wantzel, he considered the cross-sectional area variation with pressure along the same streamline. After differentiating Equation 3 with respect to the pressure and using the derivative of the cross-sectional area with the pressure equal to zero, shown on Equation 4, for the theoretical r_c in function of γ. This equation implies that the velocity in the minimum cross-section is equal to that of sound under the conditions of temperature and pressure of the fluid. Therefore, the choked flow of a gas through an orifice can be considered as streams beginning in the discharging vessel. They constrict and cross the minimum section similar to Equations 2 and 3. This implies that Reynolds was not aware of the work of Saint-Venant and Wantzel. Additionally, also probably unaware of the work of Holtzmann, Reynolds deduced that the velocity of the gas at the minimum area was equal to the velocity of sound in the gas.

In 1899, Robert Emden (1899a, 1899b) carried out experimental investigations on characteristics of air jets flowing through circular orifices. He used Dvorak's shadowgraph method to obtain photographs of the air jets. Emden examined the shadowgraphs and noted that, for a given jet velocity, it was possible to visualize a series of equidistant light discs. As the jet velocity increased, the spacing between the discs also increased, until diagonal lines started appearing and connecting their ends. At even higher speeds, the discs gradually developed into a wing-like formation and the diagonals became curved. Emden identified the discs as waves that appeared in the jet when the flow velocity reached the speed of sound in the medium. He also concluded that the space between the discs was a function of P_b/P_0 and that the discs first appeared when the theoretical r_c ratio was obtained. However, the author concluded inaccurately that the sonic velocity could not be exceeded and that the pressure in the emerging jet would be uniform and equal to the environment. These conclusions were later proved erroneous by Lord Rayleigh in 1916.

In the same year, Gutermuth (1904) made experiments on the steam flow through nozzles and orifices and could reassert the existence of choked flow. The author also showed that the experimental r_c depended upon the shape of the nozzle or orifice.

A year later, Zeuner (1905) derived theoretically the empirical equation derived by Fliegner in 1874, but it was apparently not generally accepted.

More than a decade later, Hartshorn (1917) investigated the air flow through different types of constrictions. Amongst the types studied were sharp-edged and square-edged orifices, and rounded (convergent) and Venturi nozzles, the latter with different angles of the conical diverging section. In his study, supercritical discharges were measured from sharp-edged orifices at very low P_b/P_0. The mass discharge attained constancy at P_b/P_0 of about 0.2.

In 1931, Tietjens (1931) studied sonic and supersonic flow through restriction elements. He accomplished it by equations and graphical methods. In the calculations, Tietjens implicitly assumed total properties, through the use of an entrance reservoir for pressure and temperature measurements. However, according to Arnberg (1962), the textbooks and flowmeter industry continued to favor static properties. The result had been a controversy over static and total properties causing considerable confusion on choked flow measurement for decades.

The main knowledge milestones regarding choked flow and the critical discharge coefficient are chronologically synthesized in Figure 3.

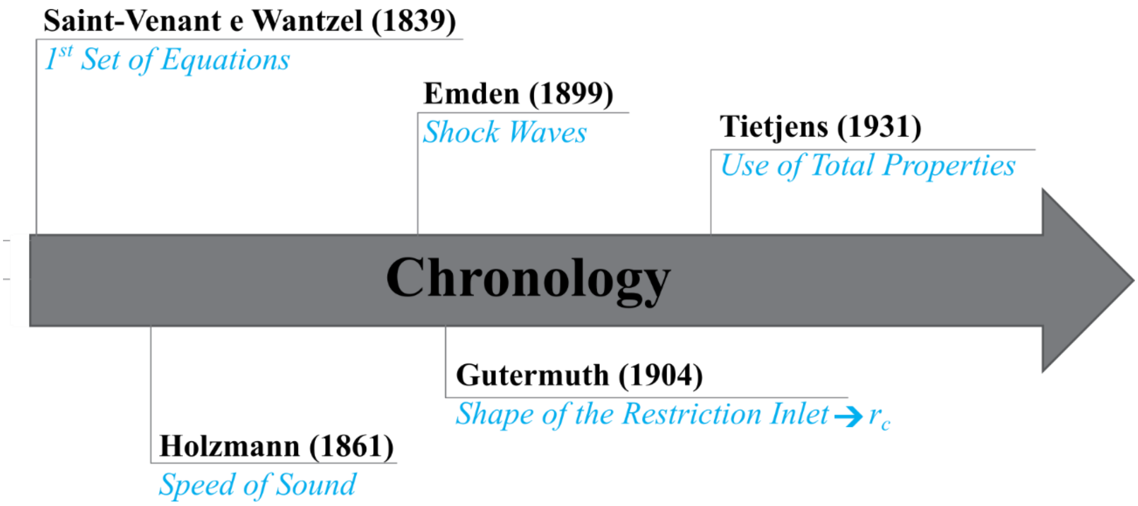

Figure 3 – Chronology of main knowledge milestones regarding choked flow and the critical discharge coefficient.

Almost two decades later, Perry (1949) published the results of the air flow through sharp-edged orifices with 45° beveling. He tested five orifices with diameters from 0.16 to 0.25 inch all set in a 2-inch pipe. The author used pipe taps to calculate C_d^*. He found C_d^* to increase 13 % from theoretical r_c value of 0.528 down to a ratio of 0.20. He compared the flows through orifices and nozzles, and said that it had long been known that the gas flow through a sharp-edged orifice does not follow the pattern that governs an ideal and isentropic flow as it does follow in the case of a nozzle.

In 1951, Grace and Lapple (1951) described precisely the determination of C_d^* and r_c values for the choked flow of air through a square-edged thick orifice plate with the same orifice thickness t and diameter d. The pipe inside diameter D and d were, respectively, 26.64 mm and 1.60 mm. In their work, they also considered nozzles, sharp-edged orifice plates, and thick orifice plates with a squared upstream edge and a 45º beveled downstream edge.

For the square-edged thick plate orifice, they found C_d^* continued to rise after the theoretical r_c, 0.528, was reached. But C_d^* approached a value around 0.83 with further P_b/P_0 reduction. According to the authors, the square-edged thick orifice plate with t equal to d (t/d is unity) presented good repeatability of C_d^* results when under choked flow, even better than the nozzles did.

In 1956, Weir, York, and Morrison (1956) developed an important experimental work on the air choked flow through square-edged orifice plates with circular and rectangular uniform cross-sectional areas. The authors used orifice plates with the same t but different d or height (for the rectangular plates). In the experiments, the authors worked with P_b/P_0 ranging from 0.526 to 0.024. They used a primary standard for the air mass-flow measurements. For the flow visualization, they used the schlieren optical technique to obtain pictures of the upstream region, downstream region, and within the thickness of the orifice plate.

The authors presented evidence that orifices with square edges can be considered as sonic nozzles by using the concept that the air, “turning the corner” of the upstream edge of the orifice plate, in effect would make its own nozzle. The authors believed that this interpretation of the experimental observations was reasonable and in full agreement with the principles of aerodynamics and thermodynamics. The authors concluded that C_d^* was not dependent on P_b/P_0 in the range studied, unlike Reynolds (1885) and Perry (1949) had indicated previously. Weir, York, and Morrison (1956) correlated C_d^* with d through the use of a geometrical parameter that accounted for the contraction of the jet at the inlet of the orifice. The correlation was a two-piece piecewise function with 0.25 inch as the boundary point for the circular square-edged orifice plates.

Arnberg (1962) made a considerably complete review about choked flow through nozzles and orifices in 1962. He addressed the performance characteristics of different types of nozzles and orifices. In the work it was noted that most of the research that had been done on choked flow through nozzles focused at power and propulsion applications, rather than in metering application. The author also stated that the design objectives of the first applications were different than those in the latter. The background of flow measurement by choking principle was, until then, limited to the characteristics derived from the inviscid, one-dimensional flow. These characteristics could determine the relative suitability of the flowmeter for any particular application. However, the effects of deviations from the simple theory became very important when high measurement accuracy was required. The precision with which the coefficients could be correlated to account for these effects then became of primary importance in evaluating the flow measurement method.

Some years later, Jackson (1964) studied five square-edged thick orifice plates of about the same d but with different t. The parameter t/d ranged from 0.33 to 10.6. He also studied a sharp-edged orifice plate with square inlet edge and exit edge with 45° beveling. The orifice plates were set in a one-inch internal diameter pipe. The experiments were performed with constant atmospheric back pressure and varying inlet pressure. This could be the reason, aligned with the small range of P_b/P_0 (0.3 to 0.8), the author could not explain the behavior of the discharge coefficients with the plate thickness. The sharp-edged orifice plate with beveling did not choke in the P_b/P_0 range and its r_c locus formed downstream of the orifice. For the square-edged orifices, the author found 4 of these plates reached choking. When this occurred, the discharge coefficient values ranged from 0.83 to 0.86. The r_c loci formed inside the orifices and choking occurred only in P_b/P_0 bellow r_c. In this respect, the results from Jackson differed from those of Weir, York, and Morrison but agreed with those of Grace and Lapple. Regarding the discharge coefficient of sharp-edged orifice, Jackson’s result was in good agreement with the theoretical results of Bragg.

In 1969, a work about gas flows in the limits of the continuous with the rarefied media was developed by Kemp Jr. and Sreekanth (1969). The authors published results on the compressible laminar flow of rarefied gases through long pipes with high-pressure gradients. The inlet Knudsen number ranged from 0.24 to 0.007, with P_b/P_0 down to 1/90. But the author stated that he could not analyze the data of the cases of extremely high pressures due to the complexity of the resulting flow and the lack of a theoretical model. However, for the flows Kemp Jr. and Sreekanth could analyze, he obtained good agreement between experimental data and the slip flow theoretical model used.

Years later, Brain and Reid (1973) reported the experiments performed with small-diameter orifices with d ranging from 1.23 to 6.41 mm and with t/d ranging from 0.14 to 5.14. Their research aimed to study the effect of parameters like Reynolds number Re, d, P_b/P_0, and t/d in the behavior of the small diameter orifices.

In 1995, Harley et al. (1995) made an experimental and theoretical study, including direct numerical simulations (DNS), on compressible flow through microchannels of simple gases like helium, argon, and nitrogen. The investigated flows were under low Re and subsonic Mach numbers Ma. The authors used silicon microchannels with trapezoidal cross-sections, which resulted in hydraulic diameters ranging from 1 to 36 μm. In the tests carried out, the Knudsen number Kn ranged from 0.001 to 0.38.

Nilpueng and Wongwises (2011) published an experimental work on the choked flow of HFC-134a through thick square-edged orifice plates with t/d ranging between 1.48 and 7.36. The upstream pressure ranged from 145 to 174 psi. The authors concluded the start of choked flow depended on the backpressure, t/d, and the inlet subcooling and short-tube orifices.

Main gas systems coupled with thick square-edged orifice plates found in literature are summarized in Table 1.

Table 1 – Main gas systems coupled with thick square-edged orifice plates.

gas	d [mm]	t/d	P_b/P_0 range	Reference
saturated steam	5.334	2.43	0.11 to 0.34	Gutermuth (1904)
	16.00	0.81	0.34 to 0.58	
air	1.588	1.00	0.18 to 0.42	Grace e Lapple (1951)
air	4.775	1.33	0.025 to 0.528	Weir, York e Morrison (1956)
air	4.757	0.6674	0.3 to 0.8	Jackson (1963)
	4.750	1.003		
HFC-134a	0.686	1.46	0.4 to 0.9	Nilpueng e Wongwises (2011)
	0.474	2.11		

3.3 USE OF CFD ON CHOKED FLOW

In the last decades several studies on choked flow have been developed with the use of CFD.

In 2018, Amnache, Omri, and Fréchette (2018) fabricated silicon-glass rectangular micro-orifices to measure mass flowrate through them. Besides the experimental work, the authors also studied numerically through CFD the flow through the micro-orifices. The design of these flowmeters was mainly based on the discharge coefficient and it was correlated to geometric parameters and Re.

In 2021, Fang et al. (2021) developed a pressure-based (PB) CFD solver to study the cavitating flow of water in Venturi nozzle. Turbulence was modeled with a quasi-DNS method, focusing on the flow characteristics and mechanism of choked flow. The interphase (interface) was tracked using the volume of fluid (VOF) method for immiscible fluids. The simulations correlated well with experimental results from the literature. The authors also made a theoretical analysis, based on fast Fourier transform (FFT), of the flow pulsating characteristics of choked flows and its influencing factors.

3.4 CRITICAL DISCHARGE COEFFICIENT ON UF_6 MODELLING

Several works on UF_6 modelling used the critical discharge coefficient in a simplified way. In 1992, Ruppel described the choked flow through a butterfly-type control valve using the C_d^* as unity (RUPPEL et al., 1992). Two years later, Santeler (1994) used the C_d^* value according to the book of Anderson (1967) to calculate the choked flow of UF_6 through orifices. But the preceding book cited C_d^* of the turbulent flow of air through square-edged orifices of about 0.82, according to Grace and Lapple (1951).

In 1995, Goode Jr et al. modeled the biphasic choked flow of UF_6 leakage at 125 ºC and 7.91 bar through guillotined pipe (GOODE JR et al., 1995). The same year, Wood (1995) modeled the gas centrifuge feed as the choked flow of UF_6 through an orifice. Wood did not need to use C_d^* since he modeled the velocity directly instead of the mass flow rate. Three years later, Malik et al. (1998) simulated the choked discharge of UF_6 from a pipe network into pipes and tanks. The authors assumed the critical pressure ratio r_c equal to 0.5 but did not give any detail on the values of C_d^* used.

In the recent aforementioned work of Paula, Migliavacca, and Guardani (2022), the authors performed two cases of choked flow modeling of UF_6. First, the authors assumed the choked flow through a control valve as if it was through a converging-diverging nozzle - for which the C_d^* is unity. Second, they modeled the choked flow through orifice plates with C_d^* values convenient to the method they used in the isotope separation cascade calculation.

3.5 FINAL CONSIDERATIONS ON THE LITERATURE REVIEW

First, the main restriction elements related to choked flow and critical discharge coefficient studies found on literature were presented. Then, the milestones in science and technology regarding these subjects were described. In the last decades the use of CFD to elucidate choked flow features and to calculate and to optimize flowmeters is increasingly more evident. Finally, several works that used C_d^* with little to no criteria for UF_6 flow modeling were presented.

Therefore, at least a mild gap exists in literature and the present work proposes a methodology to obtain a correlation of C_d^* with factors P_0 and β to issue properly UF_6 flow modeling.

4 MATERIALS AND METHODS

4.1 FLOW CLASSIFICATION AND MODELING

In this work the flow was conveniently classified according to three dimensionless numbers: Kn, Ma, and Re. Kn dictates if the flow behaves within the continuum hypothesis or in the rarefied molecular realm. Ma is used to segregate incompressible from compressible flows. Re is the most used dimensionless number in industrial engineering and classifies the flow regime according to the absence or presence of turbulence. In summary, Kn, Ma, and Re classify the flow in terms of rarefaction, compressibility and turbulence, respectively. Therefore, the present work focused on continuum and compressible flows with respect to Kn and Ma, respectively. Both laminar and turbulent low-Re flows were considered with respect to Re. In the following subsections, each flow classification method is described as well as the respective modeling.

4.1.1 Continuum flow modeling

The lower limit of P_0 range used in the study was determined using Kn to work with flows within the validity of the continuum hypothesis, rather than with rarefied gas flows. The maximum value of Kn for continuum flows usually used is 0.01 (ANDERSON, 2019), which was adopted as threshold. The Kn definition used was based on the hard sphere molecular model- and can be defined in terms of the properties of the fluid (SREEKANTH, 1965):

$$\mathrm{Kn} = \frac{\lambda}{L_c} = \frac{16}{5\sqrt{2\pi}} \frac{\mu}{Pd} [RT]^{1/2} \qquad \text{Equation 6}$$

Where λ is the mean free path of UF_6 molecules, L_c the characteristic length of the flow domain, for which d was conservatively chosen. Additionally, μ is the dynamic viscosity, R the universal gas constant, and T the absolute temperature.

The use of Equation 6 in conjunction with Kn limited to 0.01, the minimum used value of d of $4.45 \cdot 10^{-3}$ m (respective to $\beta=0.1$), the fixed total temperature of 298.15 K at the inlet, and the respective μ ($1.72 \cdot 10^{-5}$ Pa s) resulted in an estimate for the minimum P used of 25 Pa, which occurs inside the orifice. Dividing 25 Pa by the theoretical r_c for UF_6, which is 0.591 (at 298.15 K) (KIRSHENBAUM, 1943), provides an estimate to the minimum P_0 of 42 Pa to be the lower limit of the laminar subset of simulations.

4.1.2 Compressible flow modeling

The dimensionless number Ma was evaluated through its defining equation - Equation 7, which relates the velocity of the fluid $|\vec{U}|$ with that of the sound in that medium under local conditions c:

$$\mathrm{Ma}=\frac{|\vec{U}|}{c}=\frac{|\vec{U}|}{\sqrt{\frac{\gamma RT}{M}}} \qquad \text{Equation 7}$$

Where M is the molar mass of UF_6.The incompressible-compressible flows threshold for UF_6 was checked through Equation 8 to be the same as that for air, i.e., 0.3 (at Mach 0.32 the variation of density is 5 % or less).

$$\frac{\rho_t}{\rho}=\left[1+\left(\frac{\gamma-1}{2}\right)\mathrm{Ma}^2\right]^{\frac{1}{\gamma-1}} \qquad \text{Equation 8}$$

Where ρ_t is the total density.

In the vicinity and within the orifice the flow is compressible, Ma>0.3. On the other hand, the remainder of the flow domain encompasses incompressible flow (Ma<0.3). Therefore, the flow domain is comprised of incompressible and compressible flows as depicted by Figure 4.

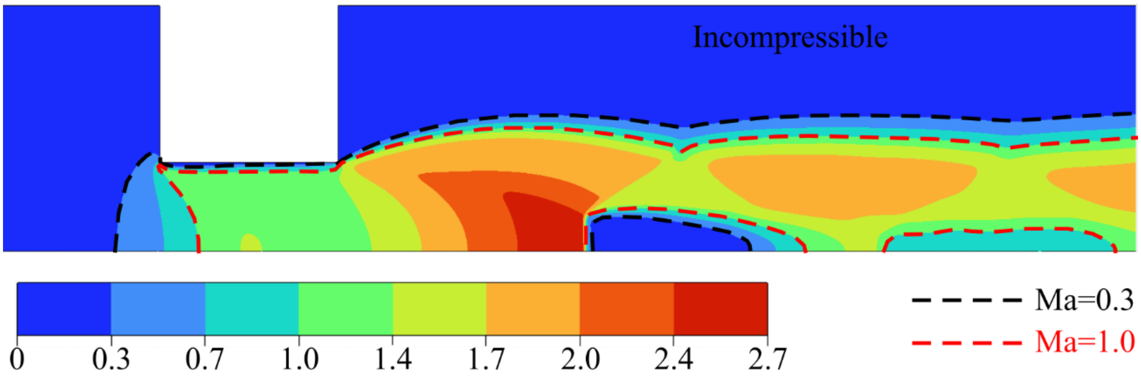

Figure 4 – Contours of Ma with highlights on the incompressible-compressible and sonic (critic) thresholds by black and red dashed contours, respectively.

Additionally, the sonic line (Ma=1) is also presented in Figure 4 and demarcate the *vena contracta* positioning inside the orifice as predicted by the literature (STODOLA, 1924).

4.1.3 Flow regime modeling

The type of flow developed in this work requires pressure BC for the inlet and the outlet regarding the momentum conservation, as described hereafter in 4.4.2. Hence, Re could only be determined after convergence of each simulation. Then, the orifice Reynolds number Re_d could be finally calculated by the post-processing capabilities of ANSYS CFD-Post through Equation 9:

$$Re_d=\frac{4\dot{m}}{\pi d\mu} \qquad \text{Equation 9}$$

Therefore, inspection was performed to determine the maximum value of the inlet total pressure P_0 within the laminar flow regime and the minimum value within the turbulent flow regime. The geometries with minimum and maximum d, i.e., relative to the limits of β, 0.1 and 0.4, were used in the inspection. For Re_d>2300, i.e., out of the laminar range for the (laminar) subset, the simulation would be discarded and another value of P_0 would be set. This iterative process continued until the P_0 chosen corresponded to the laminar threshold Re_d. The value found was 342 Pa.

Analogously, for Re_d<8000, i.e., out of the full turbulent range for the (turbulent) subset, the simulation would be discarded and a higher value of P_0 would be set. This iterative process continued until the P_0 chosen corresponded to the full-turbulent threshold Re_d. The value found was $4.9 \bullet 10^3$ Pa.

Thus, the upper limit of the laminar subset and the lower limit of the turbulent subset were defined as 342 and $4.9 \bullet 10^3$ Pa, respectively.

4.1.4 Single-phase flow regime modeling

For the turbulent flow regime part of the sampling space, the upper limit of P_0 range was chosen to keep UF_6 as a single-phase gas. Therefore, an equation that gives the saturation pressure P_{sat} between gas and solid UF_6, i.e. associated with sublimation and deposition, as a function of temperature was used (OLIVER; MILTON; GRISARD, 1953):

$$P_{sat}=1.33322 \cdot 10^{6.32471 + 0.0075377\ T - 942.76/(T-89.734)} \qquad \text{Equation 10}$$

A factor of 0.995 was further applied to Equation 10 following recommendations of the authors due to the uncertainty level of the equation.

Thus, a saturation pressure field could be generated as function of the temperature field once the simulations converged. The pressure field was subtracted from the saturation pressure field to generate a deposition proximity field. Finally, the deposition proximity field had its lower value inspected. For the positive value, the flow field encompassed only single-phase UF_6 and the simulation was valid. Otherwise, the simulation would be discarded. This process was used in the geometric model with maximum β, i.e. 0.4, to define iteratively the higher limit of P_0 for the turbulent subset. Therefore, maximum P_0 was chosen as $7.9 \bullet 10^3$ Pa for ensuring single-phase UF_6 for at least a range of 0.10 in P_b/P_0.

4.1.5 Ideal gas modeling

For high pressures or low absolute temperatures used in CFD, the modeling with the ideal gas law is unacceptable, which is not the case for UF_6 gas considered in this work, since P_0 considered are low with a maximum value of $7.9 \bullet 10^3$ Pa. Additionally, T_0 is fixed at a moderate value of 298.15 K. Even with the availability of thermodynamic parameters in the literature that would allow the use of more realistic Peng-Robinson state equation (POLING; PRAUSNITZ; O'CONNELL, 2001), the gas under consideration was chosen to be modelled as ideal. The reasons for this decision include: i) to minimize computational time of the simulations, and ii) the compressibility factor, Z, calculated as 0.997 (at 298.15 K and $7.9 \bullet 10^3$ Pa) with Peng-Robinson equation of state, i.e., the gas behaves very close to an ideal gas.

Therefore, the UF_6 density and static pressure P were related by the ideal gas equation of state - Equation 11:

$$P=\frac{\rho RT}{M} \qquad \text{Equation 11}$$

Additionally, the UF_6 gas is considered as pure U-238, since U-235 appears as low as 5 % in low-enriched-uranium (LEU) fuels, which are the most usual for pacific uses. Therefore, M was used as 0.35202 kg mol^{-1}.

4.2 MODEL GEOMETRY

4.2.1 Simplification from 3D to 2D axisymmetric geometry

The model geometries consisted of sets of pipe and orifice plate, which are cylindrical. Additionally, the flowing fluid encompassed by the pipe-and-orifice sets shows symmetry around the centerline that crosses it – a rotational axis. Hence, the geometries used in this study can be modeled as half rectangular cross-sections of the cylindrical flowing fluid volumes. Furthermore, Pianthong et al. (2007) performed CFD simulations of an ejector both in three-dimensional (3D) and two-dimensional (2D) axisymmetric (AXSM). They found 2D AXSM provided accurate results and it was chosen over 3D simulations to perform further CFD studies.

Figure 5 sketches the selection of a half cross-section from the full 3D flow domain inside the pipe-and-orifice set to be an AXSM computational domain that was used in this study. Therefore, the models used are 2D with only axial, x, and radial, r, coordinates, highlighted in red and green, respectively, in Figure 5.

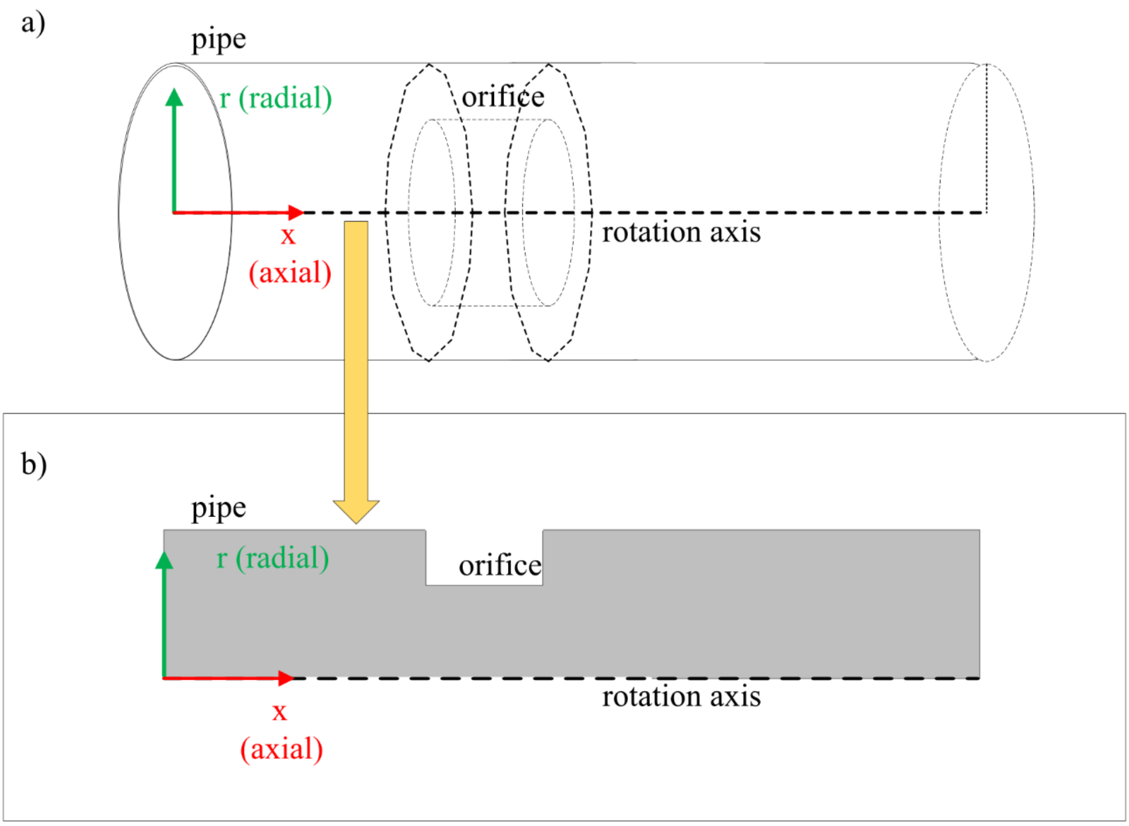

Figure 5 – Selection of a half cross-section from a) the full 3D flow domain to be b) the 2D AXSM computational domain highlighted in gray. The x (axial) and r (radial) coordinates of the cylindrical polar coordinate system are also highlighted in red and green, respectively.

The pipe is the same in all geometries used. Information on dimensions of uranium isotope separation plants are not available, since it is a sensitive matter. But, Close and Pratt (CLOSE; PRATT, 1987) stated these facilities had pipes whose D varied in size from approximately 4.45 to 10.16 cm throughout the world. Additionally, Paula, Migliavacca, and Guardani (2022) modelled choked flow through orifices set in 1-inch pipes. Therefore, a pipe with D of 4.45 cm was chosen as a fixed parameter for all geometries.

4.2.2 Flow domain extent – upstream and downstream lengths

Regarding the axial dimension, the flow domain had to be long enough to avoid locating the inlet and outlet boundaries near zones with recirculation of fluid. The upstream section required only 2 D of length in both subsets. Regarding the downstream length of the domain, the present work used 52 D and 6 D for the laminar and turbulent subsets, respectively. The downstream length difference between laminar and turbulent cases is supported by aerodynamics' boundary layer theory. Once the studied flows comprise adverse pressure gradients downstream the orifice, the turbulent boundary layer with higher mass flow rate resists more the adverse pressure gradients downstream the orifice. Whereas the laminar boundary layer resists less those pressure gradients, thus more downstream length is required to decrease them (BERTIN; CUMMINGS, 2021).

Additionally, multi-section was used to divide the flow domain, contributing to control the grid quality in the different regions, as further explained in section 4.3.

Figure 6 illustrates the flow domain for one of the geometries used (case 20 laminar – item 4.3.5) with the upstream and downstream lengths. The multi-section of the flow domain into three sections: a) upstream, b) orifice, and c) downstream are shown with pale shades of blue, green, and red, respectively, in Figure 6.

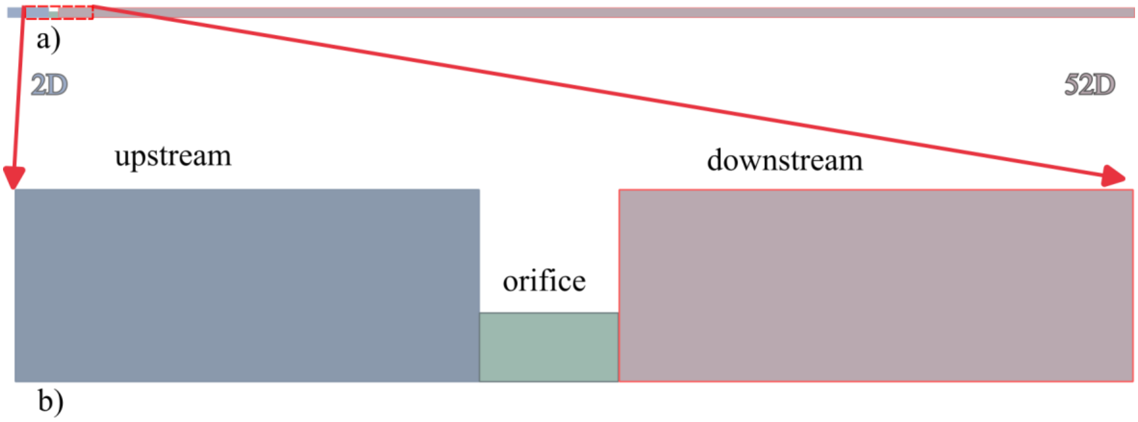

Figure 6 – a) Full computational flow domain b) Focus on the flow domain around the orifice. The multi-section division is shown as different color regions.

4.3 GRID QUALITY, REFINEMENT STUDY, AND DISCRETIZATION ERROR

The grid quality plays a paramount role in the stability and accuracy of the numerical computation. Regardless of the type of grid used, checking its quality is essential. The three most important indicators of grid quality using finite volume method in CFD include:

- Orthogonal quality (OQ);
- Equiangle skewness (ES); and
- Aspect ratio (AR).

Ansys Fluent allows the user to check these indicators, including in histogram form and by maximum and minimum. Next, the three grid quality indicators are described.

4.3.1 Grid quality metrics - orthogonal quality

The main metric which directly affects the stability of the CFD solution is face OQ. Depending on the CFD code, it is designated with different names and defining equations. But, it usually is associated with the alignment of the normal face vector regarding the vector between the centroid of the cell and those of its neighbors.

Ansys Fluent software calculates face OQ as the minimum value given by Equations 12 and 13:

$$\text{Orthogonal quality}_{\text{face, i}}=\frac{\vec{n}_{f,i}\cdot\vec{d}_{PN,i}}{\left|\vec{n}_{f,i}\right|\left|\vec{d}_{PN,i}\right|}=\cos\left(\theta_{\vec{n}_{f,i},\vec{d}_{PN,i}}\right) \qquad \text{Equation 12}$$

$$\text{Orthogonal quality}_{\text{face, i}}=\frac{\vec{n}_{f,i}\cdot\vec{d}_{Pf,i}}{\left|\vec{n}_{f,i}\right|\left|\vec{d}_{Pf,i}\right|}=\cos\left(\theta_{\vec{n}_{f,i},\vec{d}_{Pf,i}}\right) \qquad \text{Equation 13}$$

Where $\vec{n}_{f,i}$ is the normal vector to the i-th face of the cell, $\vec{d}_{PN,i}$ is the distance vector from the owner to the neighbor cell center through the i-th face of the cell, and $\vec{d}_{Pf,i}$ is the distance vector from the owner cell to its i-th face center. Additionally, $\theta_{\vec{n}_{f,i},\vec{d}_{PN,i}}$ is the angle between $\vec{n}_{f,i}$ and $\vec{d}_{PN,i}$ vectors. $\theta_{\vec{n}_{f,i},\vec{d}_{Pf,i}}$ is the angle between $\vec{n}_{f,i}$ and $\vec{d}_{Pf,i}$ vectors.

Therefore, the face OQ consists of the minimum normalized dot product of $\vec{n}_{f,i}$ vector and either $\vec{d}_{PN,i}$ or $\vec{d}_{Pf,i}$ vectors, as can be observed from the middle term in Equations 12 and 13, respectively. Likewise, the face OQ can be interpreted as the minimum cosine of the angles of the $\vec{n}_{f,i}$ vector with either $\vec{d}_{PN,i}$ or $\vec{d}_{Pf,i}$ vectors, as can be seen from the far left term in Equations 12 and 13.

The minimum value that results from applying Equations 12 and 13 for all of the faces is then defined as the cell OQ. Therefore, bad-quality cells have OQ closer to 0 and good-quality cells, which are important for the numerical stability of the solution process, have OQ closer to 1.

Figure 7 shows an example of a triangular cell and three quadrilateral cells which are connected by the shared faces to illustrate OQ calculation process.

Figure 7 depicts the sets of three vectors used to calculate OQ both for the face and the cell: i) the face normal vector, in red, ii) the vector between the owner cell centroid and the shared face center, in green, and iii) the vector between the centroids of the owner and neighbor cells, in blue.

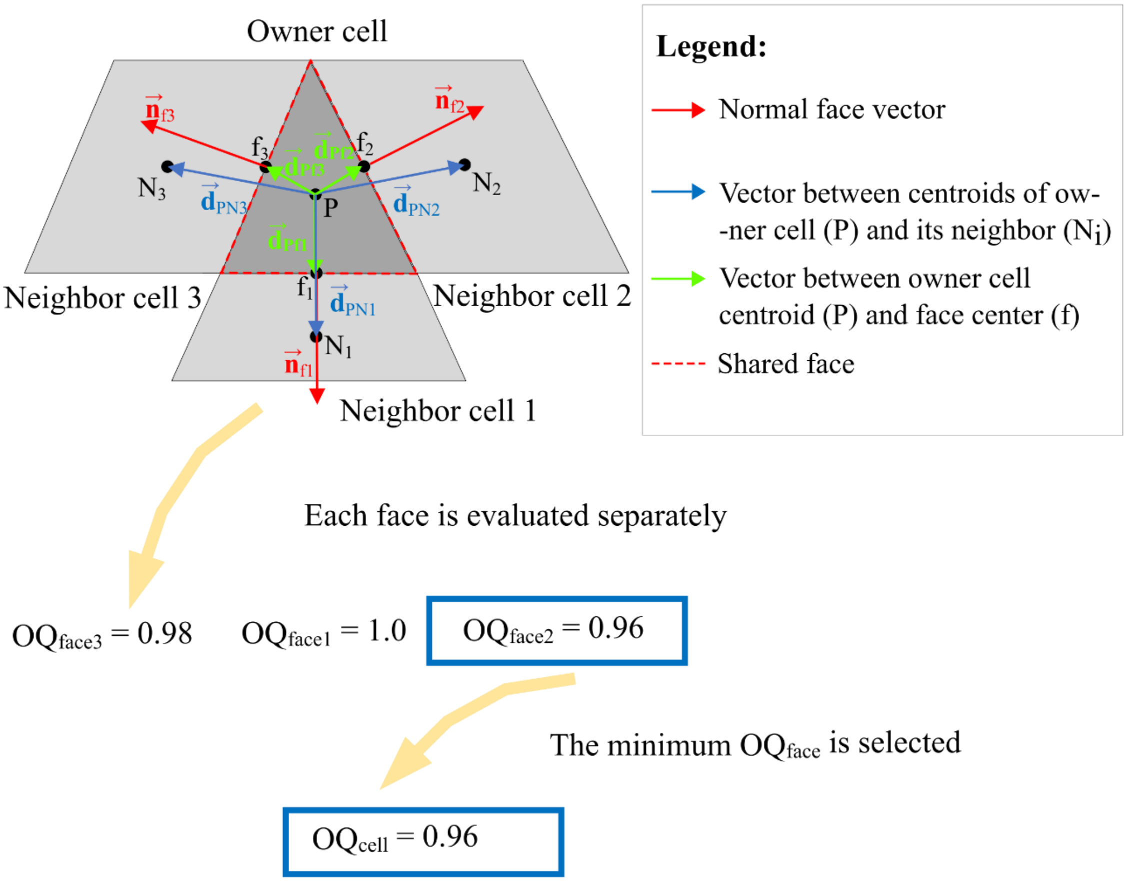

Figure 7 – An example of a triangular cell which is connected to quadrilateral cells across shared faces – each three different color vectors set is used to calculate the OQ of the respective shared face (Eqs. 12 and 13). Then the minimum face OQ is chosen to be the cell OQ.

Since the grids used in this work presented only rectangles, the face and cell OQ for all cells are unity, which means the best value possible. The reason for this is the perfect alignment of the face normal vector with both the vector between the cell and its neighbor centroids and the vector between the cell centroid and the face center. This result is also expected for Cartesian grids, which also contain only rectangular elements.

4.3.2 Grid quality metrics - equiangle skewness

ES is a useful metric that are present in mesh generators to indicate cells which are distorted and likely to have poor OQ. The face ES is the departure of the face shape from a regular polygon with the same number of sides as the face. The equilateral angle can be thought of as the ideal angle of each of the face corners required to create a regular polygon. Any departure from this ideal angle will result in a skewed cell. Therefore, the face ES is defined as the maximum value given by Equations 14 and 15:

$$\text{Equiangle Skewness}_{\text{face, i}} = \frac{\theta_{\max} - \frac{180° \ (N-2)}{N}}{180° - \frac{180° \ (N-2)}{N}} \qquad \text{Equation 14}$$

$$\text{Equiangle Skewness}_{\text{face, i}} = \frac{\frac{180° \ (N-2)}{N} - \theta_{\min}}{\frac{180° \ (N-2)}{N}} \qquad \text{Equation 15}$$

Where N is the number of sides of the face, $\theta_{\min}$ is the minimum and $\theta_{\max}$ is the maximum angle on the face. The applicability of Equations 14 and 15 is general and they are valid for any face with N sides. Once ES is estimated for all the faces of a given cell, the maximum value is selected as the cell ES. Ideally, cells would have ES very close to zero. This is the case for the grid used in the present study.

An example of four hypothetical triangles with different internal angles comprising a tetrahedral cell is shown in Figure 8 to illustrate this calculation process.

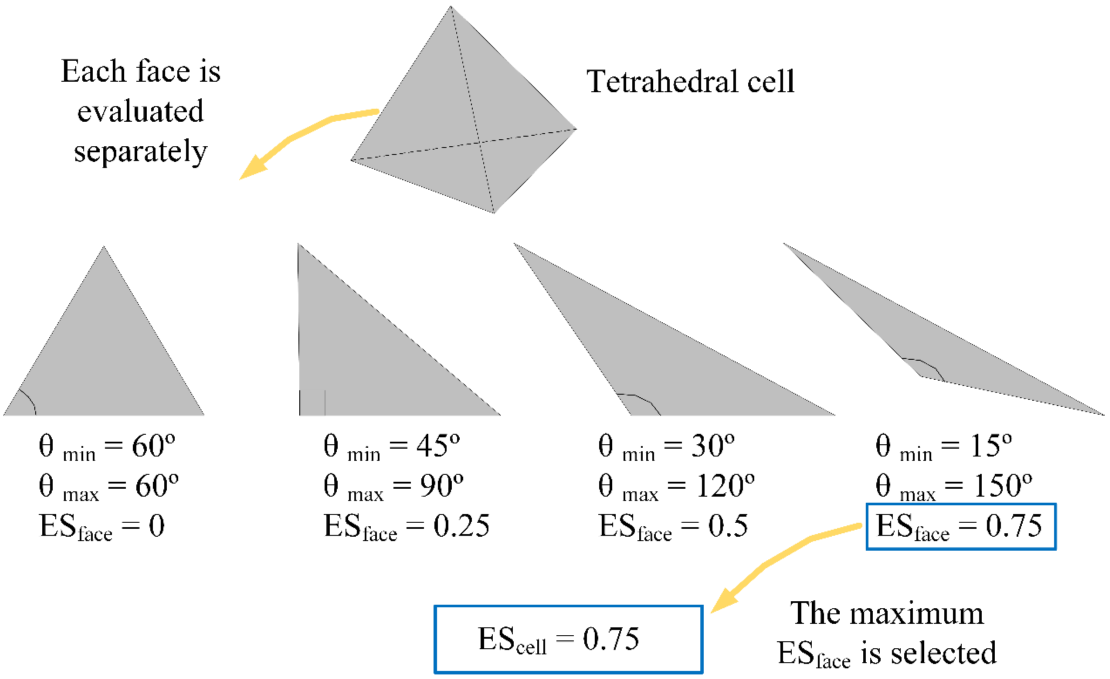

Figure 8 – An example of equiangle skewness calculation for the four triangular faces of a tetrahedral cell.

4.3.3 Grid quality metrics - aspect ratio

AR is a quality mesh indicator that is related to how the cell is spatially distributed in the directions of the ordinate system used. Its defining equations also vary conforms the CFD code used, since it is not trivial nor of singular solution to define a mathematical equation that encompasses its meaning for cells of any shape. Since the cells used in the models are all rectangles, most of CFD codes, including Ansys Fluent, present the following defining equation, Equation 16 for AR (INC., 2013):

$$\text{Aspect Ratio}_{\text{quadrilateral cell}} = \frac{L}{S} \qquad \text{Equation 16}$$

Where L, and S are the longest and shortest side lengths of quadrilateral cells, respectively.

Furthermore, Figure 9 illustrates the meaning of AR for quadrilaterals.

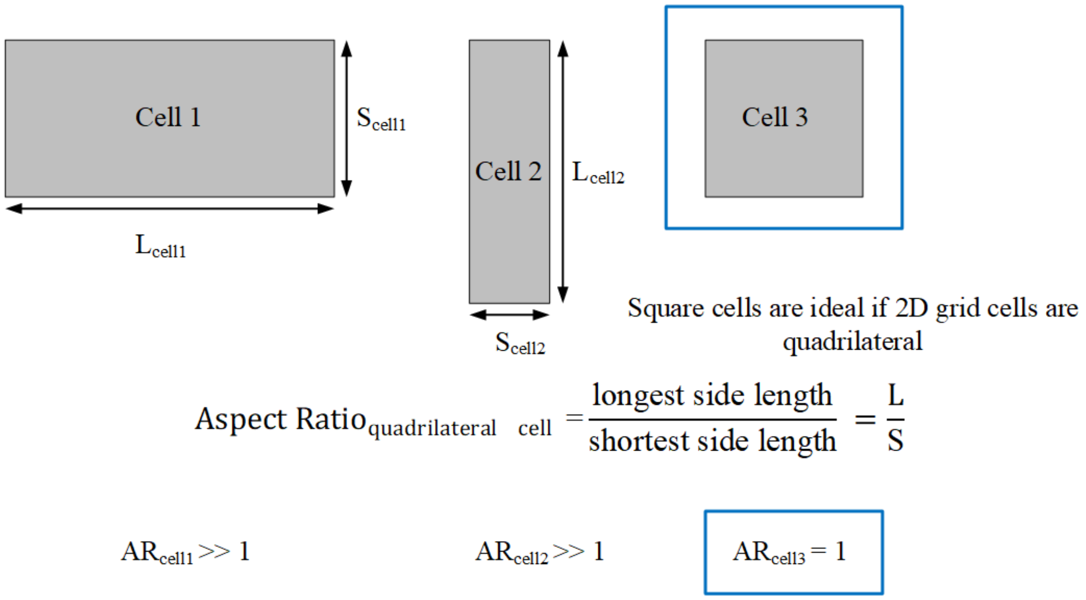

Figure 9 – AR of a regular quadrilateral is the ratio of the longest and shortest side lengths. The ideal quadrilateral cell is a square cell, for which both sides are equal and AR is unity.

4.3.4 Grid quality values

In this study, a structured non-uniform mapped-face 2D AXSM grid was used for all the models. All cells are rectangular in shape but differ in size according to the region they are located. This is shown in Figures 10, which corresponds to a coarse grid used in the refinement study (case 20 used), focusing only on the region next to the orifice.

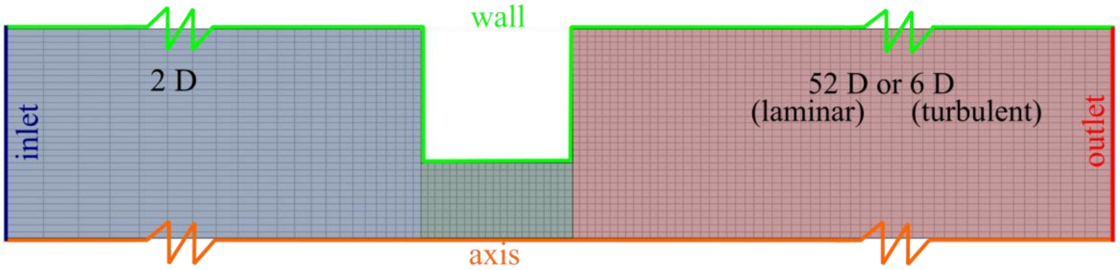

Figure 10 – The central part of the coarse grid used in the refinement study. The different colors correspond to the different subsections of the grid. Additionally, the 4 boundaries of the flow domain are designated and the upstream and downstream lengths are illustrated.

The grid was progressively stretched away from the orifice and the higher clustering was used within the orifice and in its close vicinity region, through the use of the subsections. It was chosen for capturing of expected higher gradients of properties in the aforementioned regions. The subsections are presented with different colors in Figure 10 and the upstream and downstream lengths are also depicted.

The cell ES essentially remained close to their ideal value, 0, for all cells in all grids. Cell ES was less than $1 \bullet 10^{-4}$ and $1 \bullet 10^{-6}$ for laminar and turbulent subsets, respectively. On the other hand, the AR was the only grid quality parameter used that varied considerably throughout the cells. Cell AR was less than 35 and 20 for laminar and turbulent cases, respectively. The minimum, average, and maximum values of ES and AR for the finest grid used in the refinement study (next item – 4.3.5) are shown in Table 2.

Table 2 – The grid metrics ES and AR are exemplified for case 20 (laminar and turbulent subsets), which was used for the grid refinement studies. OQ was optimal for all simulations.

Subset	Grid Metric	minimum	average	maximum
Laminar	ES	$1.31 \bullet 10^{-10}$	$7.17 \bullet 10^{-7}$	$7.84 \bullet 10^{-5}$
	AR	1.05	8.67	34.1
Turbulent	ES	$1.31 \bullet 10^{-10}$	$4.42 \bullet 10^{-7}$	$5.52 \bullet 10^{-5}$
	AR	1.00	4.69	14.9

4.3.5 Grid refinement study

The case numbered 20 in Table 11 (item 4.7.2) was chosen as representative for a grid refinement study performed for both laminar and turbulent subsets of simulations.

A series of 3 different 2D AXSM grids with progressively smaller cell sizes was used: 3) coarse, 2) medium, and 1) fine. Each finer grid had exactly four times the elements (n_d) of the next coarser grid, ranging from 48,044 the coarsest to 768,704 the finest for the laminar case. As for the turbulent case, total cell number varied from 4,752 (coarsest) to 76,032 (finest).

The three grids used in the grid refinement study for the laminar subset are presented in Figure 11 with the respective numbers of cells throughout the domain. It is worth stressing that the grids are depicted with only every other cell division (edge) due to visualization and didactic reasons.

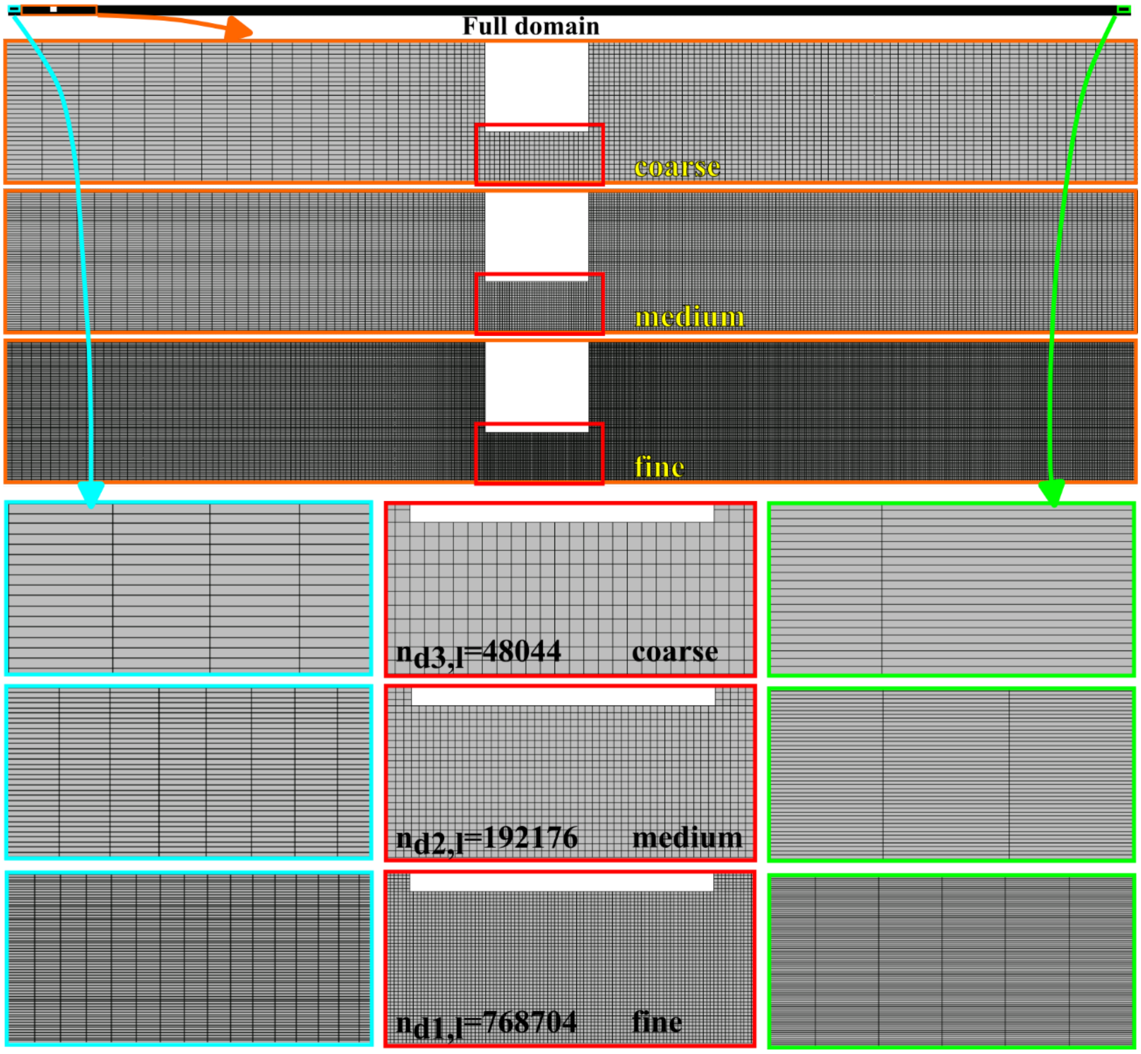

Figure 11 – Images from grids used in the refinement study for laminar case 20. From top to bottom and left to right (last row set) :1) full domain, 2) near-orifice region (orange), 3) inlet wall region (light blue), 4) more zoomed in orifice region (red), and 5) outlet wall region (light green).

Analogously, the three grids used in the refinement study for the turbulent subset are shown in Figure 12. Thus, the grid refinement factor, $f = (n_{d1}/n_{d2})^{1/2} = (n_{d2}/n_{d3})^{1/2}$, used is uniform and equal to 2 as can be checked on Figures 11 and 12.

That is in agreement with the minimum 1.3 based on experience, proposed by Celik et al. (2008).

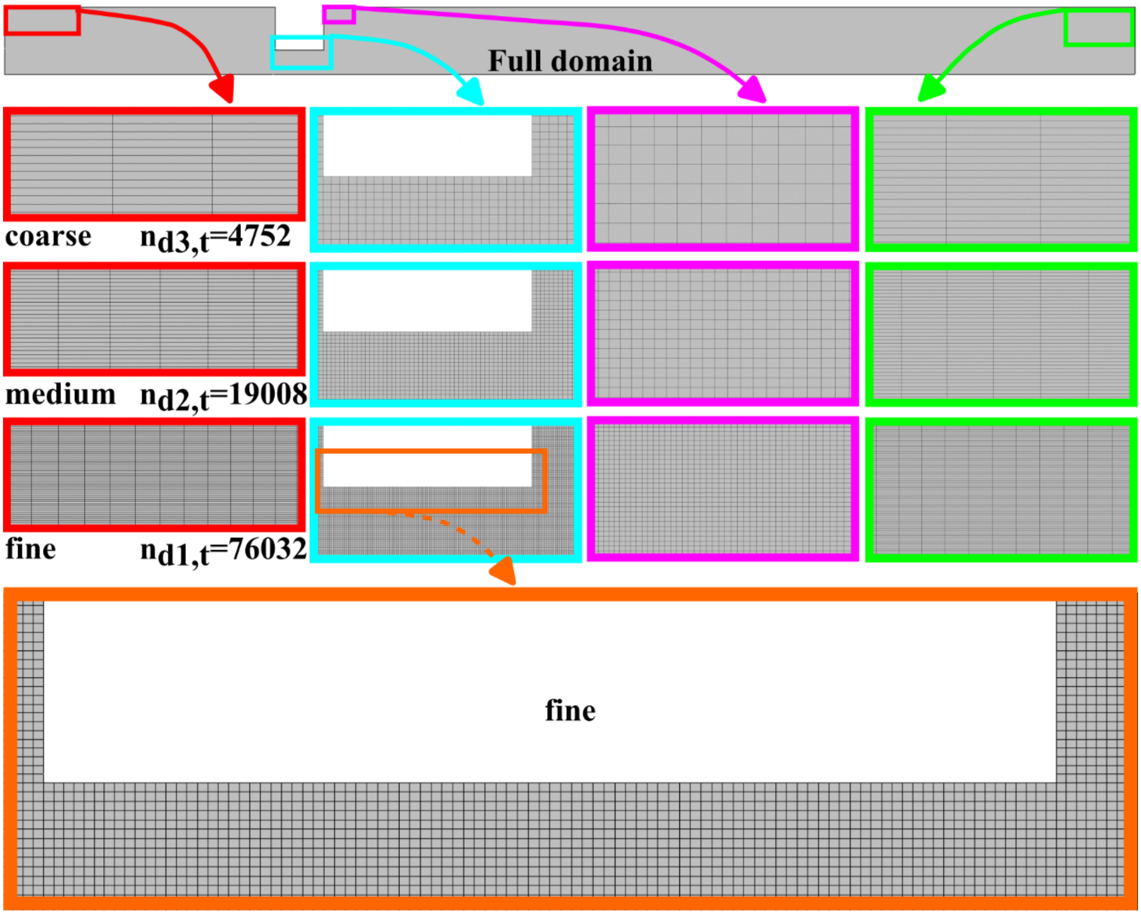

Figure 12 – Grids used in the refinement study for turbulent case 20. From top to bottom and left to right (last row set) :1) full domain, 2) inlet wall region (red), 3) near-orifice region (light blue), 4) wall outlet of the orifice region (pink), 5) outlet wall region (light green), and 6) more zoomed in orifice region for finest grid (orange).

4.3.6 Determination of the discretization error

Then, the values of C_d^* for coarse, medium, and fine grids, respectively, $(C_d^*)_3$, $(C_d^*)_2$, and $(C_d^*)_1$, can be calculated with Equation 1 in conjunction with Equation 58 (4.5 subsection).

Sequentially, the order of convergence q could be calculated through Equation 18 (CELIK et al., 2008):

$$q=\frac{1}{\ln f}\left|\ln\left|\frac{(C_d^*)_3-(C_d^*)_2}{(C_d^*)_2-(C_d^*)_1}\right|\right| \qquad \text{Equation 17}$$

The next step consisted in the estimation of C_d^* for the theoretical infinitely fine grid $(C_d^*)_0$, using Equation 19:

$$(C_d^*)_0=\frac{f^q(C_d^*)_1-(C_d^*)_2}{f^q-1} \qquad \text{Equation 18}$$

Finally, the discretization error was estimated in two ways: i) as the extrapolated relative error $e^{ext}{}_{21}$, based on Richardson extrapolation (RICHARDSON, 1910; RICHARDSON; GAUNT, 1927), and ii) as the grid convergence index (GCI_{21}), based on Roache (1994), respectively by Equations 20 and 21:

$$e_{21}^{extr}=\left|\frac{(C_d{}^*)_1-(C_d{}^*)_0}{(C_{d*})_0}\right| \qquad \text{Equation 19}$$

$$GCI_{21}=1.25\left|\frac{(C_d{}^*)_1-(C_d{}^*)_2}{(f^q-1)(C_d{}^*)_1}\right| \qquad \text{Equation 20}$$

Figure 13 synthesizes the grid refinement study for the laminar subset by presenting the values of $C_d{}^*$ against l with the projection of $(C_d{}^*)_0$ (in orange).

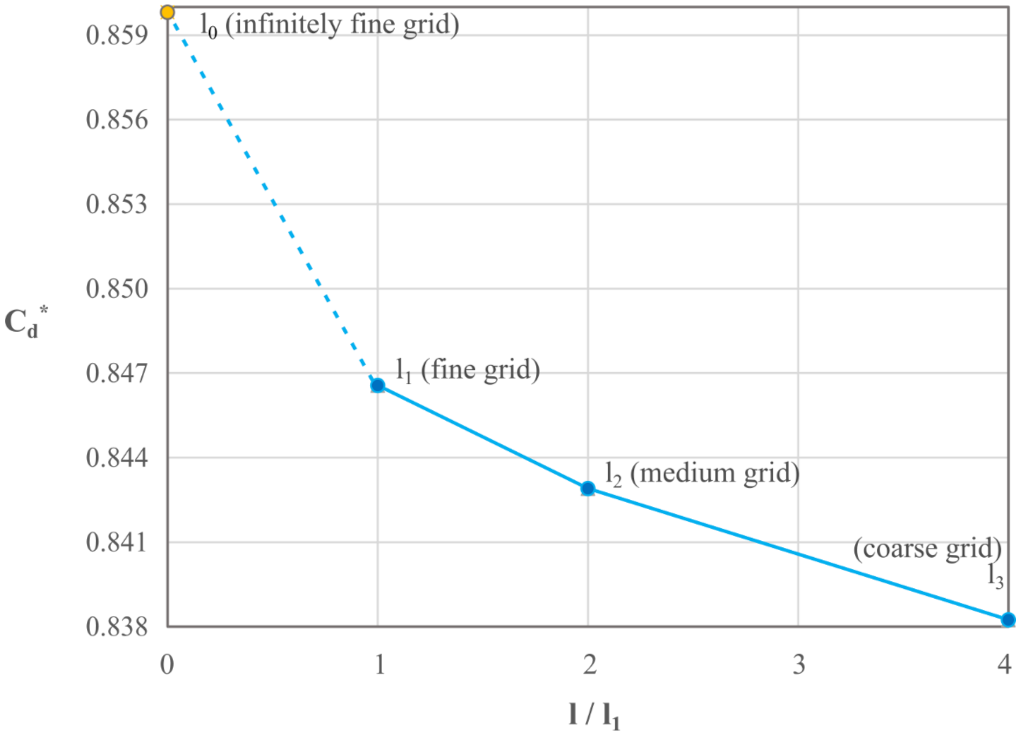

Figure 13 – The monotonic convergence of $C_d{}^*$ against l in the grid refinement study performed with case 20 (laminar). $(C_d{}^*)_0$ is projected on the ordinate axis as an orange circle.

Analogously, Figure 14 synthesizes the grid refinement study for the turbulent subset.

GCI_{32} is computed analogously to GCI_{21}. Then, GCI32 is also calculated by Equation 21 to further confirm that the obtained solution to the grid refinement study is within asymptotic range of convergence in case the values are approximately equal:

$$GCI_{32}=f^q\ GCI_{21} \qquad \text{Equation 21}$$

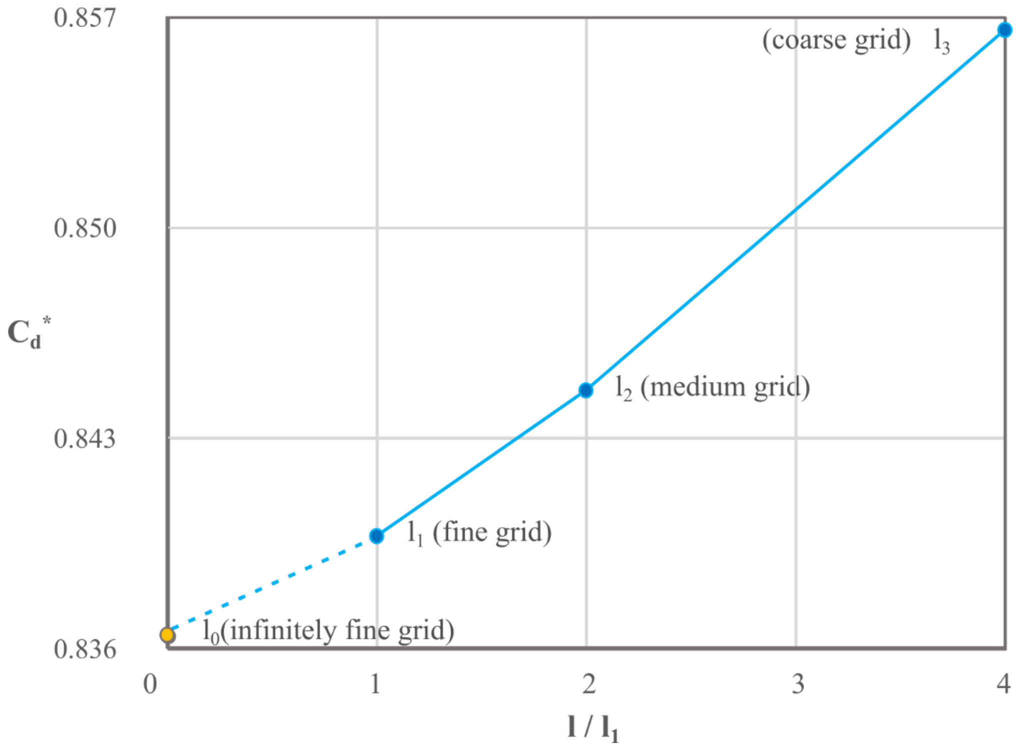

Figure 14 – The monotonic convergence of C_d^* against l in the grid refinement study performed with case 20 (turbulent). The $(C_d^*)_0$ is projected on the ordinate axis as an orange circle.

Partial and final outputs for grid refinement studies of laminar and turbulent subsets are summarized in Table 3.

Table 3 – The values of $(C_d^*)_3$, $(C_d^*)_2$, and $(C_d^*)_1$, q, $(C_d^*)_0$, e^{ext}_{21}, and GCI_{21} are synthesized for case 20 (laminar and turbulent subsets).

Subset	$(C_d^*)_3$	$(C_d^*)_2$	$(C_d^*)_1$	q	$(C_d^*)_0$	e^{ext}_{21} (%)	GCI_{21} (%)	GCI_{32} (%)
Laminar	0.838	0.843	0.847	0.351	0.859	1.54	1.96	2.51
Turbulent	0.856	0.844	0.839	1.31	0.836	0.394	0.490	1.21

For the simulation of the other 19 turbulent cases, grids similar to the finest grids (1) presented in this item were used, with n_d ranging from 74340 to 77721. But for the other 19 laminar cases, grids similar to the medium grids were selected to avoid excessive computational effort and the number of cells throughout the domain, n_d, varied from 192512 to 196077. Therefore, a cell size approximately uniform was aimed throughout all grids used in each set, since the total area of flow domain was nearly constant.

Thus, the discretization errors found are lower than 0.5 % (GCI_{21}) and should have little impact on the C_d^* results from the simulations for the turbulent cases. As for laminar cases, the discretization errors are 2.5 % (GCI_{32}), which is considerably higher than for the turbulent subset.

4.4 MODEL SOLVING – SETTING THE CFD SOLVER

4.4.1 Transport equations modeling for the laminar cases

Since the model is 2D AXSM, all derivatives with respect to the azimuthal direction are zero. Furthermore, the azimuthal component of velocity is also zero, because the flow is not expected to present any swirl. Additionally, the fluid is considered Newtonian and under steady-state conditions.

The simplifying assumptions considered in the modeling of the transport equations are summarized as follows:

- Steady-state conditions;
- All derivatives with respect to the azimuthal coordinate are zero;
- Zero azimuthal component of the velocity; and
- UF_6 behaves like a Newtonian fluid.

Therefore, the transport equations can be framed by a 2D cylindrical polar coordinate system to describe the conservation of the properties of the studied fluid. The continuity, total energy, Navier-Stokes (NS) momentum equations for the radial and axial components of velocity are, respectively (BIRD; STEWART; LIGHTFOOT, 2002; BLAZEK, 2015; FERZIGER; PERIC'; STREET, 2020; FLUENT, 2013):

$$\frac{\partial\rho}{\partial t}+\frac{\partial(\rho u)}{\partial x}+\frac{1}{r}\frac{\partial(\rho r v)}{\partial r}=0 \qquad \text{Equation 22}$$

$$\frac{\partial[\rho(h+K)]}{\partial t}+\frac{\partial[\rho u(h+K)]}{\partial x}+\frac{\partial[\rho v(h+K)]}{\partial r}+\frac{\rho v}{r}(h+K)=\frac{\partial\left[k\left(\frac{\partial T}{\partial x}\right)+u\tau_{xx}+v\tau_{xr}\right]}{\partial x}$$

$$+\frac{\partial\left[k\left(\frac{\partial T}{\partial r}\right)+u\tau_{rx}+v\tau_{rr}\right]}{\partial r}+\frac{1}{r}\left(k\frac{\partial T}{\partial r}+u\tau_{rx}+v\tau_{rr}\right) \qquad \text{Equation 23}$$

$$\frac{\partial(\rho u)}{\partial t}+\frac{\partial\left(\rho u^2\right)}{\partial x}+\frac{1}{r}\frac{\partial(\rho r v u)}{\partial r}=-\frac{\partial P}{\partial x}+\frac{\partial\tau_{xx}}{\partial x}+\frac{1}{r}\frac{\partial(r\tau_{xr})}{\partial r} \qquad \text{Equation 24}$$

$$\frac{\partial(\rho v)}{\partial t}+\frac{\partial(\rho u v)}{\partial x}+\frac{1}{r}\frac{\partial\left(\rho r v^2\right)}{\partial r}=-\frac{\partial P}{\partial r}+\frac{\partial\tau_{rx}}{\partial x}+\frac{1}{r}\frac{\partial(r\tau_{rr})}{\partial r}-\frac{\partial\tau_{\theta\theta}}{r} \qquad \text{Equation 25}$$

The four aforementioned non-zero components of the viscous stress tensor used both in NS and total energy equations are (BIRD; STEWART; LIGHTFOOT, 2002):

$$\tau_{xx}=2\mu\frac{\partial u}{\partial x}-\frac{2}{3}\mu\left(\frac{\partial u}{\partial x}+\frac{\partial v}{\partial r}+\frac{v}{r}\right) \qquad \text{Equation 26}$$

$$\tau_{xr}=\tau_{rx}=\mu\left(\frac{\partial v}{\partial x}+\frac{\partial u}{\partial r}\right) \qquad \text{Equation 27}$$

$$\tau_{rr}=2\mu\frac{\partial v}{\partial r}-\frac{2}{3}\mu\left(\frac{\partial u}{\partial x}+\frac{\partial v}{\partial r}+\frac{v}{r}\right)$$ Equation 28

$$\tau_{\theta\theta}=2\mu\frac{v}{r}-\frac{2}{3}\mu\left(\frac{\partial u}{\partial x}+\frac{\partial v}{\partial r}+\frac{v}{r}\right)$$ Equation 29

Another further definition is that of the specific kinetic energy of the fluid, K:

$$K=\frac{\left|\vec{U}\right|^2}{2}=\frac{u^2+v^2}{2}$$ Equation 30

Although the solution to the studied flows refers to steady-state conditions, the governing equations (Equations 22 to 25) present a transient term. The transient terms stabilize the solution process. This is the so-called pseudo-transient approach to solve the problem.

Furthermore, the aforementioned ideal gas equation (Equation 11) was used along with the conserved properties equations to solve the model.

4.4.2 BC for the laminar cases

The inlet BC is set to be total pressure P_0 and total temperature T_0, that is, these properties are fixed at the inlet. The outlet BC is set to be static backpressure P_b, what relates to this property being fixed at the outlet. For the pipe and orifice walls, the no-slip BC are set for the velocity. It assumes zero velocity at the walls. Lastly, the axis is set the axis BC, which impose the radial derivatives of the properties are zero. Table 4 synthesizes all BC used with the respective mathematical relations imposed. Additionally, Figure 10 illustrates the grid with the four boundaries.

Table 4 – BC used for laminar simulations.

BC surface*	Relations imposed
Inlet	$v=0$ (equivalent to velocity being normal to the inlet boundary), P_0=constant, and $T_0=298.15$ K
Outlet	P=constant, and $\partial u/\partial x=\partial v/\partial x=0$
Wall	$u=v=0$, and $Q=\partial T/\partial r=\partial p/\partial r=0$
Axis	$v=0$, and $\partial u/\partial r=\partial T/\partial r=\partial p/\partial r=0$

* The term “surface” pertains to the surfaces or axis of the full 3D model that could have been used. In the 2D AXSM models used, it refers only to the edges of the geometry that represent the surfaces (and pipe axis) of the real 3D models.

Where u is the velocity axial component, v is the velocity radial component, and Q is the heat normal to the wall.

4.4.3 Transport equations modeling for the turbulent cases

The simplifying assumptions considered in the modeling of the governing transport equations are the same as those for the laminar cases. The turbulence is modeled with the Shear-Stress Transport Kappa-Omega (SST κ-ω) model, which belongs to the family of turbulence models known as the Reynolds-averaged Navier-Stokes (RANS). Thus, the main differences in the modeling are those regarding the use of time-averaged properties including the turbulent quantities: turbulent kinetic energy (κ) and specific dissipation rate (ω).

Analogous to the laminar cases, the governing transport equations can also be framed by a 2D cylindrical polar coordinate system to describe the conservation of the time-averaged properties, represented with a superscript ($^{-}$), of the studied fluid. The mean continuity, mean total energy, mean NS momentum equations for the mean radial and axial components of velocity ($\bar{u}$ and $\bar{v}$, respectively), κ, and ω are, respectively (BIRD; STEWART; LIGHTFOOT, 2002; BLAZEK, 2015; FERZIGER; PERIC'; STREET, 2020; FLUENT, 2013):

$$\frac{\partial\rho}{\partial t}+\frac{\partial(\rho\bar{u})}{\partial x}+\frac{1}{r}\frac{\partial(\rho r\bar{v})}{\partial r}=0 \qquad \text{Equation 31}$$

$$\frac{\partial\left[\rho\left(\bar{h}+\bar{K}\right)\right]}{\partial t}+\frac{\partial\left[\rho\bar{u}\left(\bar{h}+\bar{K}\right)\right]}{\partial x}+\frac{\partial\left[\rho\bar{v}\left(\bar{h}+\bar{K}\right)\right]}{\partial r}+\frac{\rho\bar{v}}{r}\left(\bar{h}+\bar{K}\right)=\frac{1}{r}\left[\left(k+\frac{c_p\mu_t}{Pr_t}\right)\frac{\partial\bar{T}}{\partial r}+\bar{u}\bar{\tau}_{rx}+\bar{v}\bar{\tau}_{rr}\right]$$

$$\frac{\partial\left[\left(k+\frac{c_p\mu_t}{Pr_t}\right)\left(\frac{\partial\bar{T}}{\partial r}\right)+\bar{u}\bar{\tau}_{rx}+\bar{v}\bar{\tau}_{rr}\right]}{\partial r}+\frac{\partial\left[\left(k+\frac{c_p\mu_t}{Pr_t}\right)\left(\frac{\partial\bar{T}}{\partial x}\right)+\bar{u}\bar{\tau}_{xx}+\bar{v}\bar{\tau}_{xr}\right]}{\partial x} \qquad \text{Equation 32}$$

$$\frac{\partial(\rho\bar{u})}{\partial t}+\frac{\partial\left(\rho\bar{u}^2\right)}{\partial x}+\frac{1}{r}\frac{\partial(\rho r\bar{v}\bar{u})}{\partial r}=-\frac{\partial\bar{P}}{\partial x}+\frac{\partial\bar{\tau}_{xx}}{\partial x}+\frac{1}{r}\frac{\partial(r\bar{\tau}_{xr})}{\partial r} \qquad \text{Equation 33}$$

$$\frac{\partial(\rho\bar{v})}{\partial t}+\frac{\partial(\rho\bar{u}\bar{v})}{\partial x}+\frac{1}{r}\frac{\partial\left(\rho r\bar{v}^2\right)}{\partial r}=-\frac{\partial\bar{P}}{\partial r}+\frac{\partial\bar{\tau}_{rx}}{\partial x}+\frac{1}{r}\frac{\partial(r\bar{\tau}_{rr})}{\partial r}-\frac{\partial\bar{\tau}_{\theta\theta}}{r} \qquad \text{Equation 34}$$

$$\frac{\partial(\rho\kappa)}{\partial t}+\frac{\partial(\rho\bar{u}\kappa)}{\partial x}+\frac{1}{r}\frac{\partial(\rho r\bar{v}\kappa)}{\partial r}=\frac{\partial}{\partial x}\left[\left(\mu+\frac{\mu_t}{\sigma_\kappa}\right)\frac{\partial\kappa}{\partial x}\right]+\frac{1}{r}\frac{\partial}{\partial r}\left[\left(\mu+\frac{\mu_t}{\sigma_\kappa}\right)r\frac{\partial\kappa}{\partial r}\right]-\rho\beta^*\kappa\omega$$

$$+\min\left\{\mu_t\left[2\left(\frac{\partial\bar{u}}{\partial x}\right)^2+2\left(\frac{\partial\bar{v}}{\partial r}\right)^2+\left(\frac{\partial\bar{v}}{\partial x}+\frac{\partial\bar{u}}{\partial r}\right)^2\right],\ C_{lim}\rho\beta^*_\infty\kappa\omega\right\} \qquad \text{Equation 35}$$

$$\frac{\partial(\rho\omega)}{\partial t}+\frac{\partial(\rho\bar{u}\omega)}{\partial x}+\frac{1}{r}\frac{\partial(\rho r\bar{v}\omega)}{\partial r}=\frac{\partial}{\partial x}\left[\left(\mu+\frac{\mu_t}{\sigma_\omega}\right)\frac{\partial\omega}{\partial x}\right]+\frac{1}{r}\frac{\partial}{\partial r}\left[\left(\mu+\frac{\mu_t}{\sigma_\omega}\right)r\frac{\partial\omega}{\partial r}\right]-\rho\beta\omega^2$$

$$+\alpha\alpha^*\rho\left[2\left(\frac{\partial\bar{u}}{\partial x}\right)^2+2\left(\frac{\partial\bar{v}}{\partial r}\right)^2+\left(\frac{\partial\bar{v}}{\partial x}+\frac{\partial\bar{u}}{\partial r}\right)^2\right]+\frac{2(1-F_1)\rho}{\omega\sigma_{\omega,2}}\left(\frac{\partial\kappa}{\partial x}\frac{\partial\omega}{\partial x}+\frac{\partial\kappa}{\partial r}\frac{\partial\omega}{\partial r}\right) \qquad \text{Equation 36}$$

The four aforementioned non-zero components of the mean viscous stress tensor used both in NS and total energy equations are (BIRD; STEWART; LIGHTFOOT, 2002):

$$\bar{\tau}_{xx}=2\left(\mu+\mu_t\right)\frac{\partial\bar{u}}{\partial x}-\frac{2}{3}\left(\mu+\mu_t\right)\left(\frac{\partial\bar{u}}{\partial x}+\frac{\partial\bar{v}}{\partial r}+\frac{\bar{v}}{r}\right)$$ Equation 37

$$\bar{\tau}_{xr}=\bar{\tau}_{rx}=\left(\mu+\mu_t\right)\left(\frac{\partial\bar{v}}{\partial x}+\frac{\partial\bar{u}}{\partial r}\right)$$ Equation 38

$$\bar{\tau}_{rr}=2\left(\mu+\mu_t\right)\frac{\partial\bar{v}}{\partial r}-\frac{2}{3}\left(\mu+\mu_t\right)\left(\frac{\partial\bar{u}}{\partial x}+\frac{\partial\bar{v}}{\partial r}+\frac{\bar{v}}{r}\right)$$ Equation 39

$$\bar{\tau}_{\theta\theta}=2\left(\mu+\mu_t\right)\frac{\bar{v}}{r}-\frac{2}{3}\left(\mu+\mu_t\right)\left(\frac{\partial\bar{u}}{\partial x}+\frac{\partial\bar{v}}{\partial r}+\frac{\bar{v}}{r}\right)$$ Equation 40

Another further definition is that of the mean specific kinetic energy of the fluid, $\bar{K}$:

$$\bar{K}=\frac{\bar{u}^2+\bar{v}^2}{2}$$ Equation 41

Where the turbulent viscosity μ_t, the turbulent Prandtl number for κ (σ_κ) and ω (σ_ω), α, α^*, β, β^*, β_i, blending function F_1, Φ_1, D_ω^+, blending function F_2, and Φ_2 are defined by Equations 42 through 54 (FLUENT, 2013):

$$\mu_t=\frac{\rho\kappa}{\omega}\frac{1}{\max\left[\frac{1}{a^*},\frac{\sqrt{2\left(\frac{\partial\bar{u}}{\partial x}\right)^2+2\left(\frac{\partial\bar{v}}{\partial r}\right)^2+\left(\frac{\partial\bar{v}}{\partial x}+\frac{\partial\bar{u}}{\partial r}\right)^2}\ F_2}{a_1\ \omega}\right]}$$ Equation 42

$$\sigma_\kappa=\frac{1}{\frac{F_1}{\sigma_{\kappa,1}}+\frac{(1-F_1)}{\sigma_{\kappa,2}}}$$ Equation 43

$$\sigma_\omega=\frac{1}{\frac{F_1}{\sigma_{\omega,1}}+\frac{(1-F_1)}{\sigma_{\omega,2}}}$$ Equation 44

$$\alpha^*=\alpha_\infty^*\left(\frac{\frac{0.024}{3}+\frac{\rho\kappa}{\mu\omega R_\kappa}}{1+\frac{\rho\kappa}{\mu\omega R_\kappa}}\right)$$ Equation 45

$$\alpha=\frac{\alpha_\infty}{\alpha^*}\left(\frac{\alpha_0+\frac{\rho\kappa}{\mu\omega R_\omega}}{1+\frac{\rho\kappa}{\mu\omega R_\omega}}\right)$$ Equation 46

$$\beta^*=\beta_\infty^*\left[\frac{\frac{4}{15}+\left(\frac{\rho\kappa}{\mu\omega R_\beta}\right)^4}{1+\left(\frac{\rho\kappa}{\mu\omega R_\beta}\right)^4}\right]\left[1+\zeta^*\max\left(\frac{2k}{\gamma RT}-M_{t0}{}^2,0\right)\right]$$ Equation 47

$$\beta=\beta_i\left\{1-\beta_\infty^*\left[\frac{\frac{4}{15}+\left(\frac{\rho\kappa}{\mu\omega R_\beta}\right)^4}{1+\left(\frac{\rho\kappa}{\mu\omega R_\beta}\right)^4}\right]\frac{\zeta^*}{\beta_i}\max\left(\frac{2k}{\gamma RT}-M_{t0}{}^2,0\right)\right\}$$ Equation 48

$$\beta_i=F_1\beta_{i,1}+(1-F_1)\beta_{i,2}$$ Equation 49

$$F_1=\tanh\left(\Phi_1^4\right)$$ Equation 50

$$\Phi_1=\min\left[\max\left(\frac{\sqrt{\kappa}}{0.09\ \omega y},\frac{500\mu}{\rho y^2\omega}\right),\ \frac{4\rho\kappa}{\sigma_{\omega,2}D_{\omega}^{+}y^2}\right]$$ Equation 51

$$D_{\omega}^{+}=\max\left[\frac{2\rho\kappa}{\sigma_{\omega,2}\omega}\left(\frac{\partial\kappa}{\partial x}\frac{\partial\omega}{\partial x}+\frac{\partial\kappa}{\partial r}\frac{\partial\omega}{\partial r}\right),10^{-10}\right]$$ Equation 52

$$F_2=\tanh\left(\Phi_2^2\right)$$ Equation 53

$$\Phi_2=\max\left[2\frac{\sqrt{\kappa}}{0.09\ \omega y},\frac{500\mu}{\rho y^2\omega}\right]$$ Equation 54

Where y is the distance to the next surface. The values of constants used in the aforementioned equations are presented in Table 5 (FLUENT, 2013).

Table 5 – The constants used in SST κ-ω turbulence modeling.

a_1	M_{t0}	$\mathbf{Pr_t}$	$\mathbf{C_{lim}}$	$\boldsymbol{\alpha^*_\infty}$	$\boldsymbol{\alpha_\infty}$
0.31	0.25	0.85	10	1	0.52

$\boldsymbol{\alpha_0}$	$\boldsymbol{\beta^*_\infty}$	$\boldsymbol{\beta_{i,1}}$	$\boldsymbol{\beta_{i,2}}$	ζ^*	$\boldsymbol{\sigma_{\kappa,1}}$
0.11111	0.09	0.075	0.0828	1.5	1.176

$\boldsymbol{\sigma_{\omega,1}}$	$\boldsymbol{\sigma_{\kappa,2}}$	$\boldsymbol{\sigma_{\omega,2}}$	$\mathbf{R_\beta}$	$\mathbf{R_\kappa}$	$\mathbf{R_\omega}$
2.0	1.0	1.168	8	6	2.95

4.4.4 BC for the turbulent cases

The BC are analogous to those used for the laminar case subset, with the difference that exact-value properties are replaced by mean-value properties. Moreover, there are the BC for the turbulence quantities κ and ω, which are described hereafter. For the inlet BC, κ is given as function of the mean inlet velocity and the turbulence intensity I, which is chosen as 5% as can be seen in Equation 55.

$$\kappa=\frac{3}{2}(I\ \bar{u})^2$$ Equation 55

Whereas for ω at the inlet, the turbulent-to-laminar viscosity ratio μ_t/μ was used as 10 in Equation 56.

$$\omega=\frac{\rho\kappa}{\mu}\left(\frac{\mu_t}{\mu}\right)^{-1}$$ Equation 56

For the walls, κ is zero and ω is defined according to Equation 57:

$$\omega = 10\frac{6\,\mu}{\rho\beta_i y^2}$$ Equation 57

Additionally, κ and ω are extrapolated from interior cells at the outlet BC, which means the axial derivatives of κ and ω are zero. Finally, the radial derivatives of κ and ω are zero at the axis BC. Table 6 synthesizes all BC used with the respective mathematical relations imposed.

Table 6 – BC used for turbulent simulations.

BC surface	Relations imposed
Inlet	$\kappa=\frac{3}{2}(I\,\bar{u})^2$, $\omega=\frac{\rho\kappa}{\mu}\left(\frac{\mu_t}{\mu}\right)^{-1}$, $\bar{v}=0$, $\bar{P}_0$ =constant, and $\overline{T_0}$ =298.15 K
Outlet	$\bar{P}$ =constant, and $\partial\kappa/\partial x=\partial\omega/\partial x=\partial\bar{u}/\partial x=\partial\bar{v}/\partial x=0$
Wall	$\kappa=\bar{u}=\bar{v}=0$, $\omega=10\frac{6\,\mu}{\rho\beta_i y^2}$, and $\bar{Q}=\partial\bar{T}/\partial r=\partial\bar{P}/\partial r=0$
Axis	$\bar{v}=0$, and $\partial\kappa/\partial r=\partial\omega/\partial r=\partial\bar{u}/\partial r=\partial\bar{T}/\partial r=\partial\bar{P}/\partial r=0$

Where $\bar{Q}$ is the mean heat normal to the walls.

4.5 POST PROCESSING – DISCHARGE COEFFICIENT CALCULATION

After each simulation attained convergence, the discharge coefficient was calculated with Ansys CFD-Post by Equation 1 in conjunction with the defining equation of theoretical (isentropic and adiabatic) mass flow rate – Equation 58 (SHAPIRO, 1953):

$$\dot{m}_{\mathrm{theoretical}}=\frac{\pi d^2}{4}P_0\sqrt{\frac{\gamma M}{RT_0}\left(\frac{2}{\gamma+1}\right)^{(\gamma+1)/(\gamma-1)}}$$ Equation 58

The upstream and downstream pressures, P_0 and P_b were same values used in the inlet and outlet boundaries of the computational flow domain.

4.6 MODEL CALIBRATION

The verification of the code is first considered by the robustness of the internal codes of the Ansys Fluent. Then, by means of checking if correct BC, type of solver, discretization schemes, physical models used, along with proper conditions of convergence, as can be seen from Tables 6 and 7.

Table 8 presents the analogous solver settings for the turbulent subset of simulations.

Table 7 – Solver settings for laminar simulations.

Setting	Choice
Solver type	Density-based (DB) (implicit), double precision, 2D axisymmetric
Fluid	UF_6(g) with properties given by last 5 lines of Table 9
Viscous Model	Laminar
Formulation of the solver	Implicit (DB)
Flow type	Advection upstream splitting method (AUSM)
Gradient discretization	Least Squares Cell Based
Flow discretization	Second Order Upwind
Additional information	High order term relation (on) and convergence acceleration for stretched meshes (on)
Convergence Criteria	The simulations ran until inlet and outlet mass flow rates were equal up to the fifth non-zero digit
BC	According to Table 4

Table 8 – Solver settings for the turbulent simulations.

Setting	Choice
Solver type	DB (implicit), double precision, 2D AXSM
Fluid	UF_6(g) with properties given by last 5 lines of Table 9
Viscous Model	SST κ-ω, with corrections to the coefficients regarding: low Re, compressibility effects, and production limiter
Formulation of the solver	Implicit (DB)
Flow type	AUSM
Gradient discretization	Least Squares Cell Based
Flow discretization	Second Order Upwind
Turbulent kinetic energy and Specific dissipation rate discretization	Second Order Upwind
Additional information	High order term relaxation (on) and convergence acceleration for stretched meshes (on)
Convergence Criteria	The simulations ran until inlet and outlet mass flow rates were equal up to the fifth non-zero digit and the total temperature at the outlet section was equal to that of the inlet down to a difference of 0.01
BC	According to Table 6

There are two major types of solver: PB and DB. The first was initially designed to solve only incompressible flows. The latter was designed to solve compressible flows. As solvers evolved along the decades and nowadays both can solve a wide range of flows from incompressible to low-Ma supersonic flows. Therefore, DB solver was chosen for the simulations, since it is more appropriate if transonic and considerably higher supersonic flows are expected, which comprehend the cases studied in this work.

In general terms, DB solvers are notably more difficult to converge than PB. Hence, preliminary simulations were done using PB.

Then, DB was used with first-order discretization schemes. Convergence was unfeasible considering the computational resources available. Finally, DB solver with second-order discretization schemes were performed with feasible convergence thanks to an algebraic multigrid method of initialization. The initialization method provided a preliminary solution for the Euler version of the governing equations, i.e., through inviscid flow hypothesis.

The convergence of each simulation was assured by checking of mass and total temperature conservation throughout the computational flow domain as given by Equations 59 and 60, respectively.

$$\dot{m}_{inlet}=\dot{m}_{outlet} \qquad \text{Equation 59}$$

$$(T_0)_{inlet}=(T_0)_{outlet} \qquad \text{Equation 60}$$

Consequently, the residuals of the equations decreased at least three orders of magnitude for most simulations. Nonetheless, they were not considered essential for convergence. Two graphs of the residuals against the number of iterations of case 20 (laminar and turbulent) are presented in Figure 15 for didactic purposes.

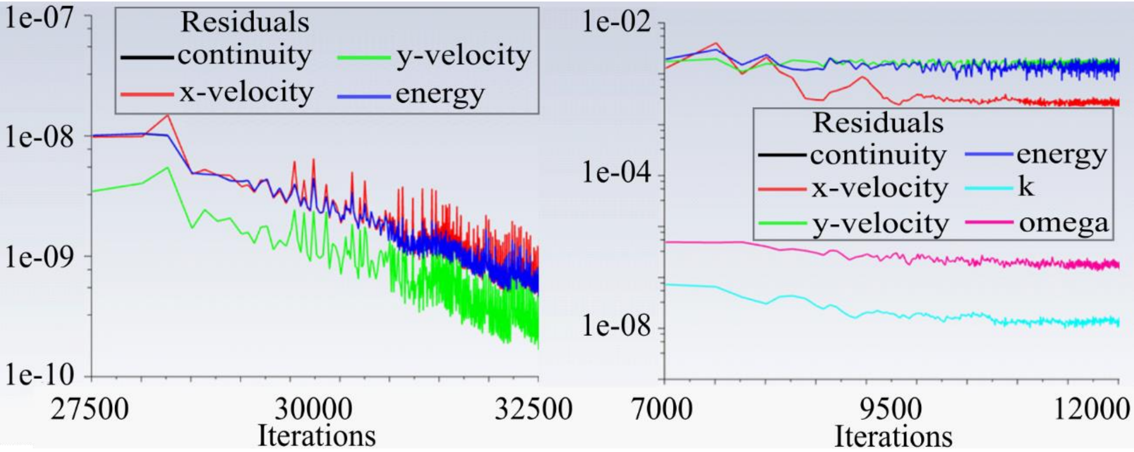

Figure 15 – Residuals of the field variables against number of iterations for case 20. On the left, laminar case with P_b/P_0 = 0.10. On the right, turbulent case with P_b/P_0 = 0.26.

Once the verification was complete, the next step consists of performing the validation of the model. However, the working fluid UF_6 is a controlled non-available material related to a sensitive matter so that the model could not be directly validated with physical experiments. The alternative route is to calibrate the model with experimental data from literature cases the most similar possible to assure the validity of the model regarding the physical process.

The results of Jackson (1964b) were used to calibrate the model. In particular, the results of the thick plate orifice III, which has unity t/d value. P_b/P_0 was selected as 0.4 and 0.3 for the minimum of two unity simulations regarding this calibration case. Table 9 synthesizes the settings of the calibration case.

Table 9 – Settings table for the calibration case. The P_0 varied for the two unity simulations. All other parameters remain in a fixed setting.

Parameter		**Min**	**Fixed**	**Max**	**Unit**
Upstream pressure	P_0	$2.50 \bullet 10^5$		$3.33 \bullet 10^5$	Pa
Downstream pressure	P_b		$1.00 \bullet 10^5$		Pa
Orifice-to-pipe diameter ratio	β		0.176		[ ]
Pipe internal diameter	D		26.924		mm
Orifice thickness-to-diameter ratio	t/d		1.003		[ ]
Upstream domain length	L_U		13.462		mm
Downstream domain length	L_D		107.696		mm
Inlet total temperature	T_0		298.15		K
Heat capacity ratio	γ		1.4		[ ]
Specific heat capacity at constant pressure	c_p		1006.43		$J\ kg^{-1}\ K^{-1}$
Thermal conductivity	k		0.0242		$J\ (m\ s\ K)^{-1}$
Viscosity	μ		Sutherland with μ_0: $1.716 \bullet 10^{-5}$ Pa s, T_0: 273.11 K, and T_{ef}:110.56 K		Pa s
Density	ρ		According to ideal gas law		$kg\ m^{-3}$
Molecular mass	M		28.966		$g\ mol^{-1}$

Where μ_0 is the reference viscosity, T_{ref} is the reference temperature, and T_{ef} is the effective temperature.

4.7 DESIGN OF COMPUTER EXPERIMENTS

4.7.1 Limiting values of the factors and fixed parameters

As stated in Section 3 - Objectives, the present work focuses on obtaining a correlation of C_d^* for the single-phase UF_6 choked flow through thick plate orifices under 298.15 K with two factors: P_0, and β.

The factor β, which controls the variation of d, ranged from 0.10 and 0.40. Since t/d chosen for the orifice plates was unity, t was equal to d and varied along with it.

The factor P_0 ranged from 42 to 342 Pa in the laminar subset, as described in items 4.1.1 and 4.1.3, respectively.

In the turbulent subset, P_0 ranged from $4.9 \cdot 10^3$ to $7.9 \cdot 10^3$ Pa according to the criteria described in 4.1.3 and 4.1.4, respectively.

All factors and parameters with their ranges and fixed values, respectively, are presented in Table 10.

Table 10 – Settings table for the planning of case studies. The P_0 and β varied as factors. All other parameters remain in a fixed setting.

Factor/Parameter		Min	Fixed	Max	Unit
Upstream pressure (laminar cases)	P_0	42		342	Pa
Upstream pressure (turbulent cases)	P_0	$4.9 \cdot 10^3$		$7.9 \cdot 10^3$	Pa
Orifice-to-pipe diameter ratio	β	0.10		0.40	[ ]
Pipe internal diameter	D		44.5		mm
Orifice thickness-to-diameter ratio	t/d		1		[ ]
Upstream domain length	L_U		0.089		m
Downstream domain length (lam)	$L_{D,L}$		2.314		m
Downstream domain length (turb)	$L_{D,T}$		0.267		m
Inlet total temperature	T_0		298.15		K
Heat capacity ratio	γ		1.068		[ ]
Specific heat capacity at constant pressure	c_p		371 (KIRSHENBAUM, 1943)		$J\ kg^{-1}\ K^{-1}$
Thermal conductivity	k		$-9.0 \times 10^{-4} + 2.57 \times 10^{-5}\ T$ (DEWITT, 1960)		$J\ (m\ s\ K)^{-1}$
Viscosity	μ		$3.91 \times 10^{-6} + 3.83 \times 10^{-8} T + 2.78 \times 10^{-11} T^2 - 2.10 \times 10^{-14} T^3$ (MIGLIORINI, 2016)		Pa s
Density	ρ		According to ideal gas law		$kg\ m^{-3}$
Molecular mass	M		352.02		$g\ mol^{-1}$

4.7.2 Cases selection – Latin hypercube sampling (LHS)

For the design of physical experiments a consolidated literature of Design of Experiments (DOE) is available, as gathered in many books (BOX; HUNTER; HUNTER, 2005; RODRIGUES; IEMMA, 2014). Additionally, DOE statistical methods can also be used for CFD simulations, as pointed out and exemplified by Cervantes and Engström (2004). Besides, in the last decades a more specific branch of the literature has been gaining space and proving itself as a more adequate approach to the design and analysis of deterministic computer experiments, as stressed by Viana (2016). Many of the Design and Analysis of Computer Experiments (DACE) literature can be found collectively in the two textbooks (KLEIJNEN, 2018; SANTNER; WILLIAMS; NOTZ, 2018). Therefore, a Latin hypercube sampling (LHS) method within the DACE framework instead of a DOE classical sampling method was chosen as the space-filling method, i.e., to guide effectively the parameter variation throughout the cases to be simulated.

The number of cases to be simulated n_p was estimated using Equation 61, according to guidance of Loeppky. Sacks, and Welch (2009):

$$n_p=10n_f \qquad \text{Equation 61}$$

Where n_f is the number of factors.

Therefore, a minimum of 20 simulations had to be performed for each subset. The setup of each of the 20 pair of values for factors (P_0, β), i.e., the sampling was made according to an algorithm proposed by van Dam et al. (2007). The algorithm consists of a distance-optimized type of LHS method. The method, besides accounting for the point distribution in a Sudoku-like fashion, also assures radial coverage of each point through the factor space. These features can be observed in Figure 16 by the fitting of each point in the grid rectangles and blue circles, respectively.

Figure 16 shows graphically the sampling of all 20 pairs of values of the factors P_0 and β for the respective cases. The abscissa from Figure 16 is both for the laminar (in green) and the turbulent cases (in blue). The exact values are shown in Table 11.

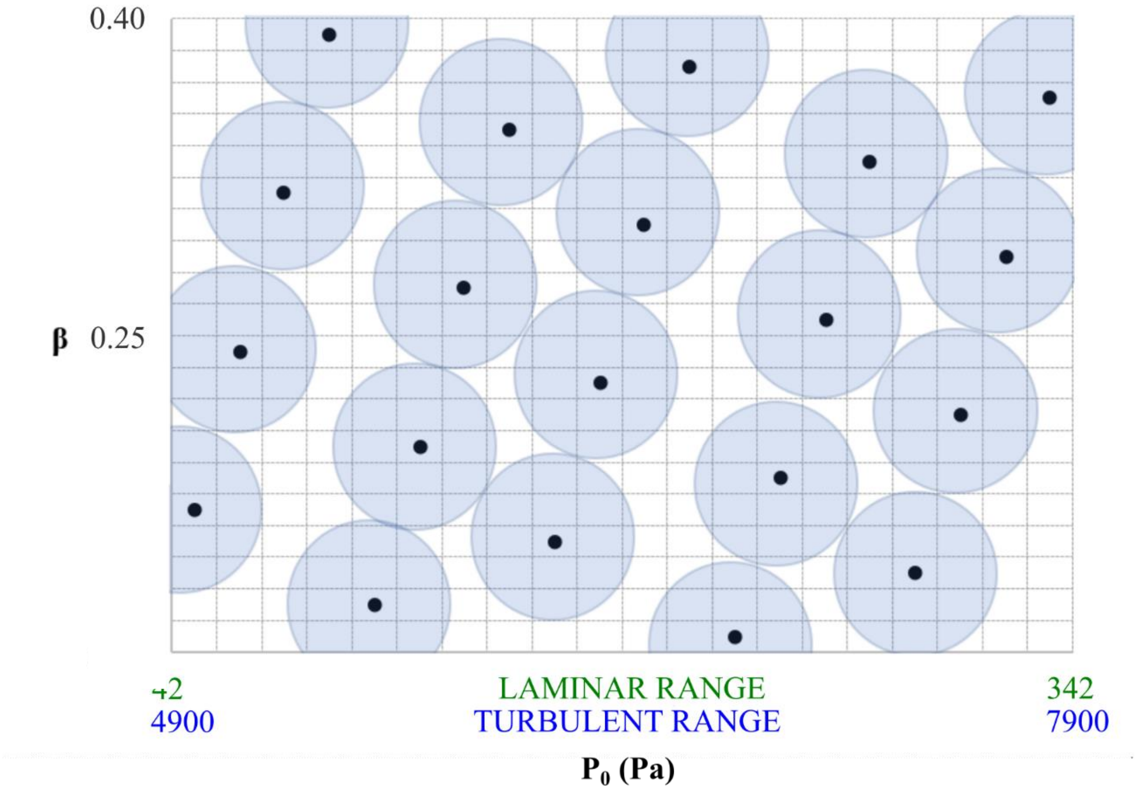

Figure 16 – Distribution of points in the factor space, according to LHS proposed by van Dam et al. (2007). Abscissa limits with different colors are due to the partition of cases between laminar (green) and turbulent (blue) regimes.

Table 11 – The 20 simulations sampled by Latin hypercube method with values of the 2 factors considered for the 20 laminar and turbulent cases.

Nº	**β**	**Laminar P_0 (Pa)**	**Turbulent P_0 (Pa)**
1	0.1675	49.5	4975
2	0.2425	64.5	5125
3	0.3175	79.5	5275
4	0.3925	94.5	5425
5	0.1225	109.5	5575
6	0.1975	124.5	5725
7	0.2725	139.5	5875
8	0.3475	154.5	6025
9	0.1525	169.5	6175
10	0.2275	184.5	6325
11	0.3025	199.5	6475
12	0.3775	214.5	6625
13	0.1075	229.5	6775
14	0.1825	244.5	6925
15	0.2575	259.5	7075
16	0.3325	274.5	7225
17	0.1375	289.5	7375
18	0.2125	304.5	7525
19	0.2875	319.5	7675
20	0.3625	334.5	7825

However, each of the 20 cases (laminar and turbulent) was planned to be simulated by five unity simulations. For each case, P_0 was kept constant and P_b varied such that

P_b/P_0 decreased from 0.5 to 0.1 in 0.1 intervals. The theoretical r_c, which is 0.591 at 25 ºC, was used to restrict P_b/P_0 in the aforementioned range. The result was a curve of C_d (C_d^*) against P_b/P_0.

4.8 CORRELATION

4.8.1 Data fitting

With the simulation results, a correlation was obtained to fit the behavior of C_d^* with P_0 and β factors through a mean response curve with minimal deviations from the simulation data. Polynomial regression was used for the fitting process.

4.8.2 Correlation assessment by new simulated point in sampling space

Finally, the correlation had its accuracy assessed by comparing the prediction it gave for a new simulation with the output of that simulation. In the sampling factor space, a point was chosen with P_0=6775 Pa and β=0.34. The remaining setting was the same as given by Table 10.

5 RESULTS AND DISCUSSIONS

5.1 CALIBRATION RESULTS

The calibration simulations with P_b/P_0=0.4 and P_b/P_0=0.3 yielded C_d^* equal to 0.814 and 0.817, respectively which is less than 3 % of error with experiments (JACKSON, 1964b). Thus, the flow did not reach choking but C_d^* increased slowly with decreasing P_b/P_0 similarly to that presented by Jackson (1964b).

Ma contours with abundant shock waves are presented by Figure 17.

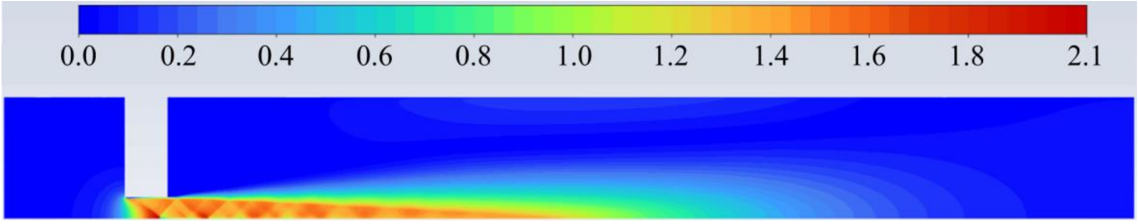

Figure 17 – Mach number contours of the calibration case (turbulent with P_b/P_0 = 0.30) to illustrate the shock wave structures formed downstream of the orifice.

Figure 18 shows constricted flow in the orifice by the streamlines. Additional flow structures like the recirculation flows are also present upwards and downwards with respect to the orifice.

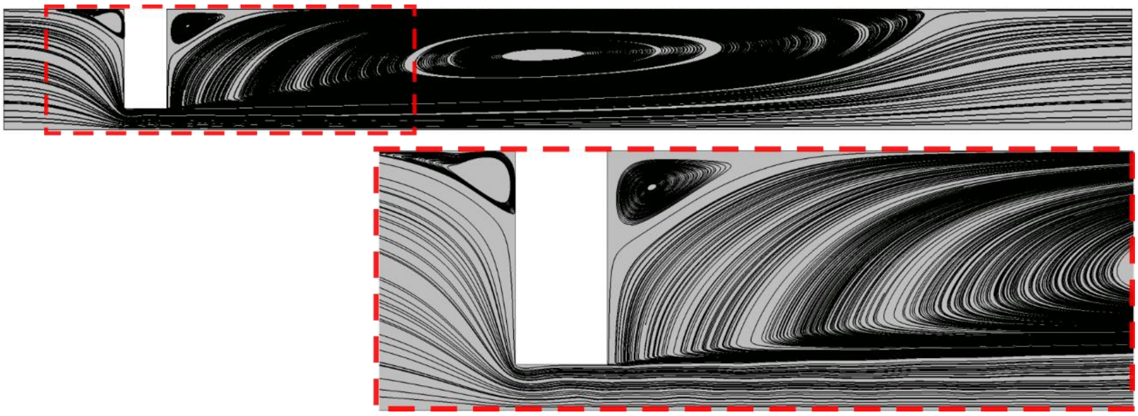

Figure 18 – Streamlines of case 1 (turbulent with P_b/P_0 = 0.30).

Total temperature contours are presented in Figure 19 to illustrate the constancy of total temperature and total enthalpy throughout the domain.

Some diffusion of the properties can be observed at the region of the shock waves. Due to the full NS solution of the problem, which encompasses thermal conductivity and viscosity, the total temperature stratification is an acceptable solution.

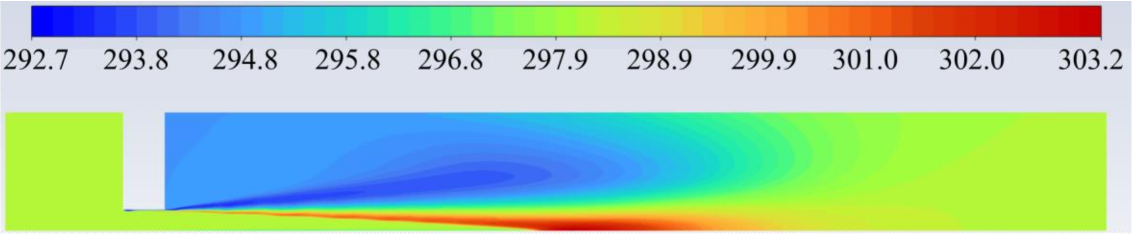

Figure 19 – Total temperature contours of case 1 (turbulent with P_b/P_0 = 0.30).

Total pressure contours are presented in Figure 20 to depict the decrease of total pressure and total entropy at the limits of shock waves in the jet. It can be used to infer the flow is not isentropic.

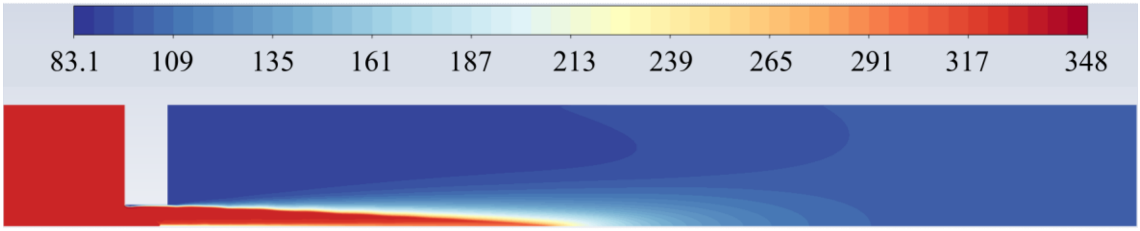

Figure 20 – Total pressure contours of calibration case (turbulent with P_b/P_0 = 0.30).

5.2 PRESENTATION OF GRAPHICAL RESULTS FOR LIMITING CASES

The contour graphs of the field variables chosen to be presented in this section are those from the cases with maximum and minimum values of the studied factors: cases 1, 4, 13, and 20. Along with the graphical results of the limiting cases some physical explanation is available.

The field variables chosen to be shown for the 4 foregoing cases are Mach number, total pressure, and total temperature. Moreover, the streamlines are presented for all 4 cases. To ensure single-phase for the studied flows the deposition proximity contours are also presented for the turbulent subset, since turbulent cases reach closer to saturation conditions for the studied range of P_b/P_0. Conversely, only case 20 of the laminar subset showed deposition within the P_b/P_0 range studied. Therefore, deposition proximity contours are presented only for case 20.

Mach number contours are important to depicture the transonic and supersonic flow structures like shock waves, and Prandtl-Meyer expansion fans in terms of the velocity scaled to the local speed of sound. Additionally, the streamline graphs further depict the constriction of the flow streamlines in the orifice region and show the secondary flow structures such as recirculation zones. The contours of total temperature and total pressure are graphical representations of the first and second laws of thermodynamics, respectively.

The conjunction of adiabatic walls, no machine work (only fluid work), and steady-state conditions imply the constancy of the total enthalpy flux throughout the flow domain (BERTIN; CUMMINGS, 2021):

$$(\dot{m}h_0)_{inlet}=(\dot{m}h_0)_{outlet} \qquad \text{Equation 62}$$

Where h_0 is total enthalpy.

Furthermore, the gas is considered to be perfect and consequently its specific heats are constant. Hence, the total temperature is proportional to the total enthalpy. Consequently, total temperature is also constant throughout the domain as seen in Equation 60. The constancy of both properties can be observed as a predominant color in total temperature contours.

Complementarily, total pressure contours can be used to assure the applicability of thermodynamics’ second law throughout the flow domain according to Equation 63:

$$\Delta S=R\ln\left[\frac{(P_0)_{inlet}}{(P_0)_{outlet}}\right] \qquad \text{Equation 63}$$

Where ΔS is the entropy change between outlet and inlet.

Therefore, some decrease in total pressure is expected along the boundary layer and shock waves since the flow is not isentropic.

5.2.1 Case 1 - Laminar

The contours and streamlines for the geometric case 1 with laminar flow regime are presented next. The chosen P_b/P_0 is 0.10 and choked flow was not achieved.

Discontinuities in Ma field associated mainly to oblique shock waves and Prandtl-Meyer fan expansions can be inferred from Figure 21.

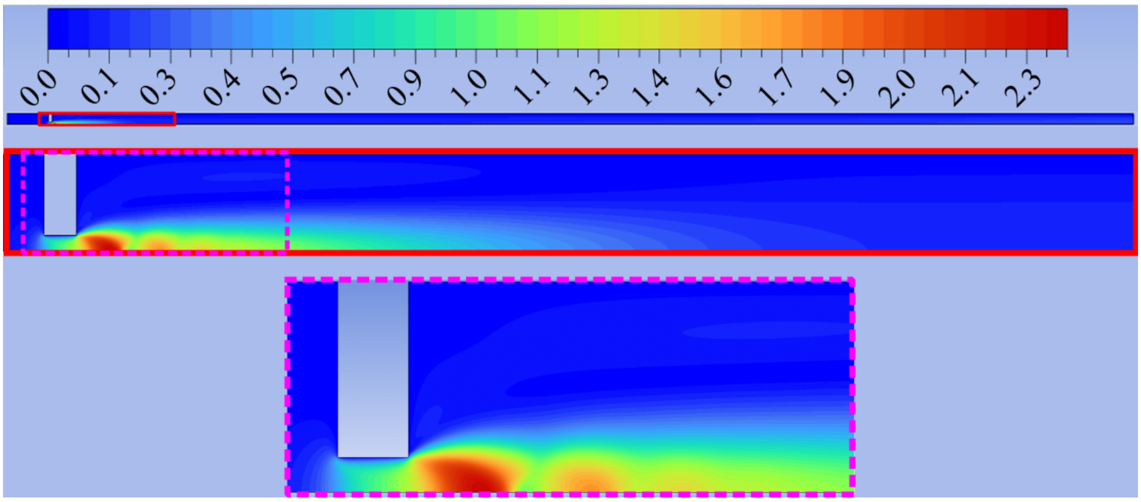

Figure 21 – Mach number contours of case 1 (laminar with $P_b/P_0 = 0.10$) to illustrate the shock wave structures formed downstream of the orifice.

Figure 22 shows constricted flow in the orifice by the streamlines. Additional flow structures like the recirculation flows are also present.

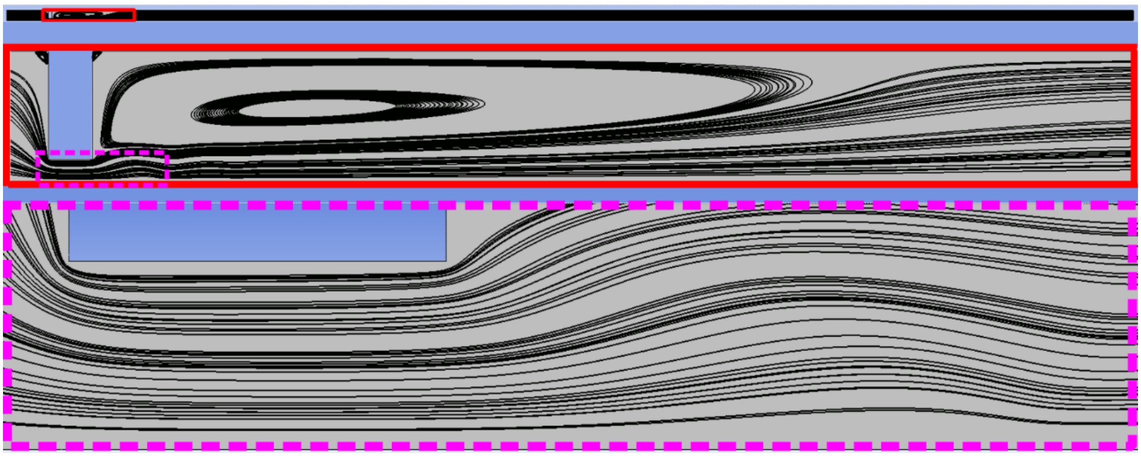

Figure 22 – Streamlines of case 1 (laminar with $P_b/P_0 = 0.10$).

The total temperature contours are presented in Figure 23 to illustrate the constancy of total temperature and total enthalpy throughout the domain.

Some diffusion of the properties can be observed at the region of the shock waves. Due to the full NS solution of the problem, which encompasses thermal conductivity and viscosity, the total temperature stratification is an acceptable solution.

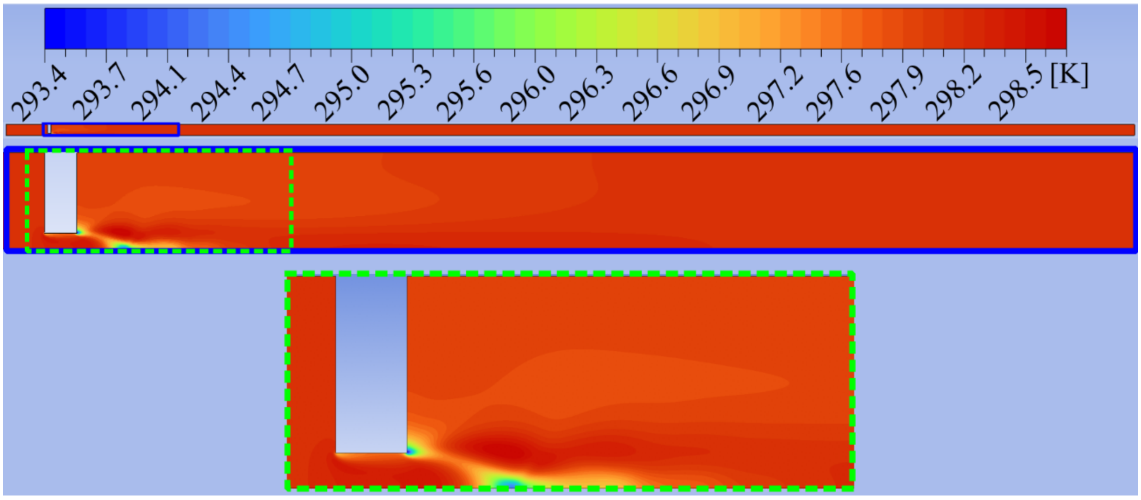

Figure 23 – Total temperature contours of case 1 (laminar with $P_b/P_0 = 0.10$).

Total pressure contours are presented in Figure 24 to depict the decrease of total pressure and total entropy at the limits of shock waves in the jet. It can be used to infer the flow is not isentropic.

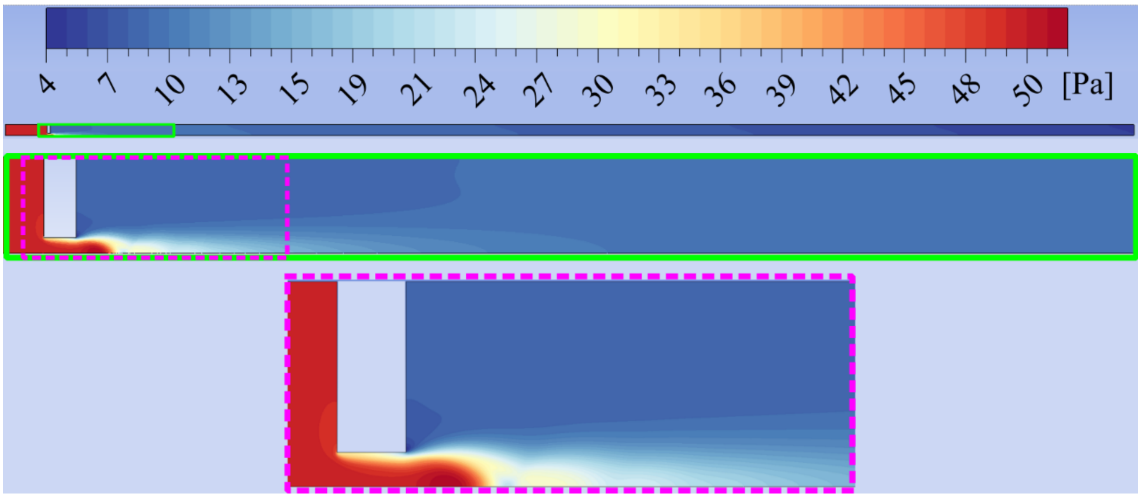

Figure 24 – Total pressure contours of case 1 (laminar with $P_b/P_0 = 0.10$).

5.2.2 Case 1 - Turbulent

The contours and streamlines for the geometric case 1 with turbulent conditions are presented next. The chosen P_b/P_0 is 0.26, which is the lower P_b/P_0 considering two digits for single-phase UF_6. Additionally, the flow is choked.

Besides the conventional contours used for laminar cases, the deposition proximity is also shown for all turbulent cases to illustrate how the choked flow is close to saturation conditions.

Therefore, for the flow conditions, Figure 25 shows how UF_6 is close to deposition saturation.

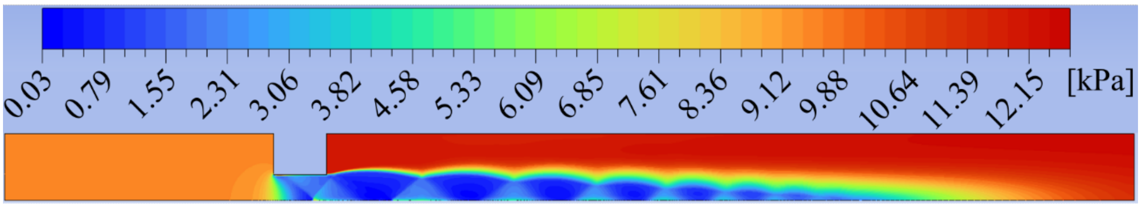

Figure 25 – Deposition proximity contours of case 1 (turbulent with P_b/P_0 = 0.26).

The closest to gas-solid equilibrium can be checked by the leftmost extreme of the pressure scale, i.e., 30 Pa. Moreover, the regions of the flow closest to saturation are that of Prandtl-Meyer expansion fans. Thus, P_b/P_0 cannot be lowered more if single-phase is required.

Oblique shock waves and Prandtl-Meyer expansions are presented by Figure 26 through Mach number contours.

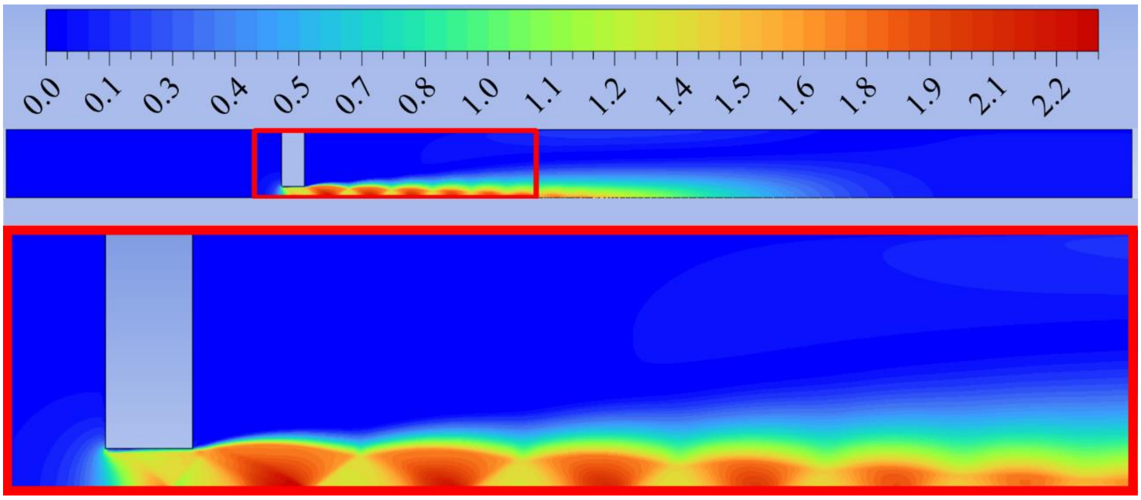

Figure 26 – Mach number contours of case 1 (turbulent with P_b/P_0 = 0.26).

Correspondingly, the flow is depicted through streamlines in Figure 27.

Moreover, recirculation flow is present upstream and downstream of the orifice likewise the laminar case. These secondary flow structures are more intense and bigger than the laminar counterparts.

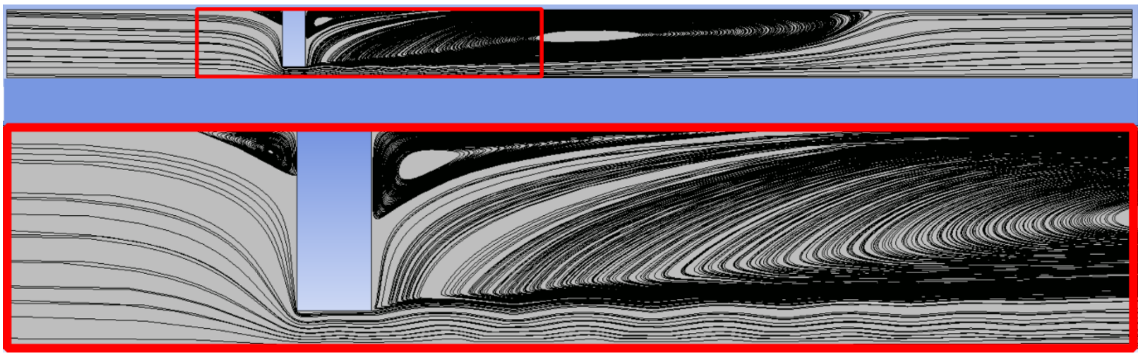

Figure 27 – Streamlines of case 1 (turbulent with $P_b/P_0 = 0.26$).

Total temperature contours approximately constant around predominant green (298.15 K) are shown in Figure 28. The stratification of total temperature downstream of the orifice is higher than for the laminar counterpart since effective diffusivities are increased by turbulence.

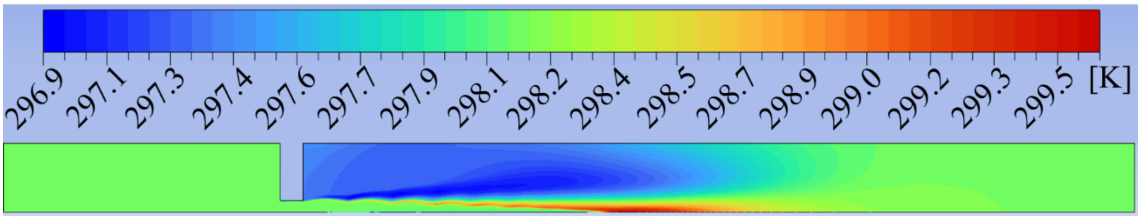

Figure 28 – Total temperature contours of case 1 (turbulent with $P_b/P_0 = 0.26$).

Total pressure contours are presented by Figure 29.

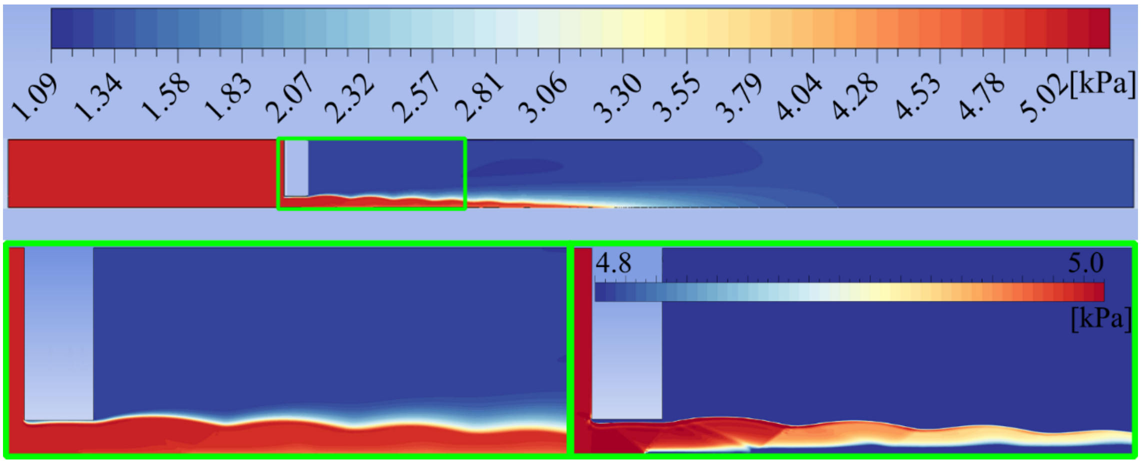

Figure 29 – Total Pressure contours of case 1 (turbulent with $P_b/P_0 = 0.26$).

The area near the orifice highlighted in green is zoomed in on the down-left part of the graph. This zoomed in area had its color scale changed to correspond to a lower pressure range as showed on the down-right part of Figure 29. The scale change reveals total pressure changes related to the oblique waves shown in the Mach number contours of Figure 26.

5.2.3 Case 4 - Laminar

The contours and streamlines for the geometric case 4 with laminar conditions are presented next. The chosen P_b/P_0 is 0.20 and the choked flow was reached.

Mach number contours are depicted by Figure 30, where flow structures like Prandtl-Meyer expansions, oblique shock waves, and a small normal shock wave as can be noted in the left-down part of the pink zoomed in area as a light blue color.

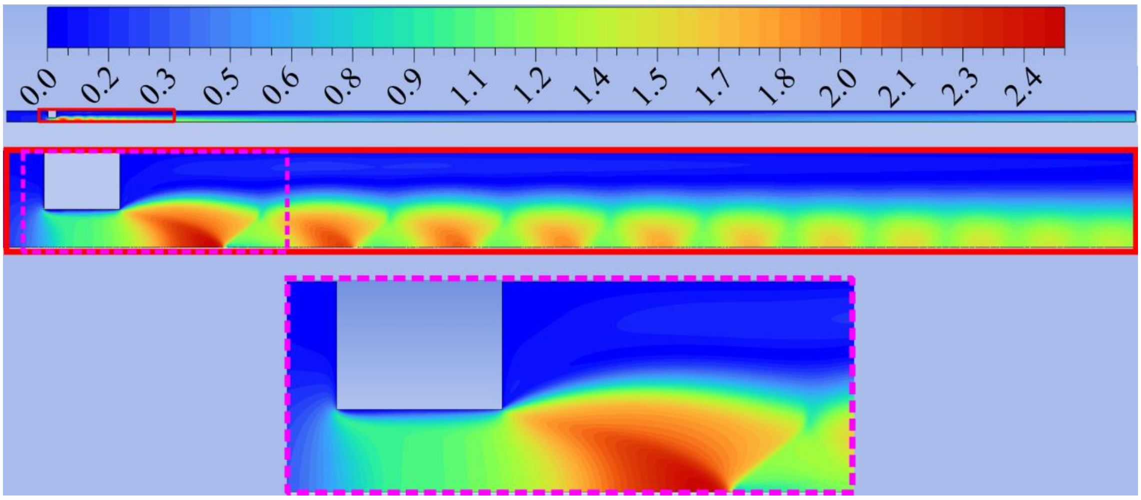

Figure 30 – Mach number contours of case 4 (laminar with P_b/P_0 = 0.20, choked).

The streamlines showed in Figure 31 complement the velocity information about the flow.

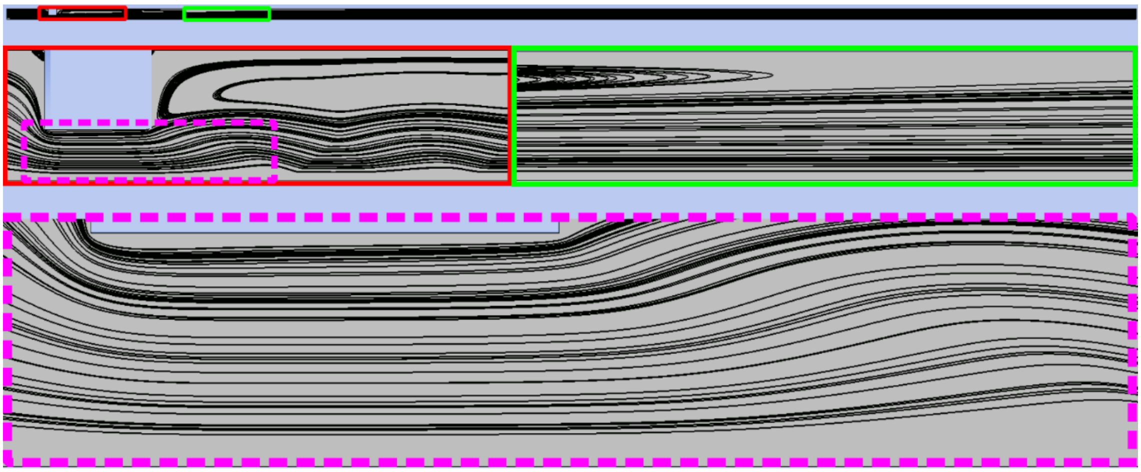

Figure 31 – Streamlines of case 4 (laminar with P_b/P_0 = 0.20, choked).

Total temperature contours are presented in Figure 32. Since the flow is laminar, the diffusion of this property is considerably subtle and the color is close to homogeneous orange. Some discontinuities can be noted and associated with that from the shock waves presented in Figure 30.

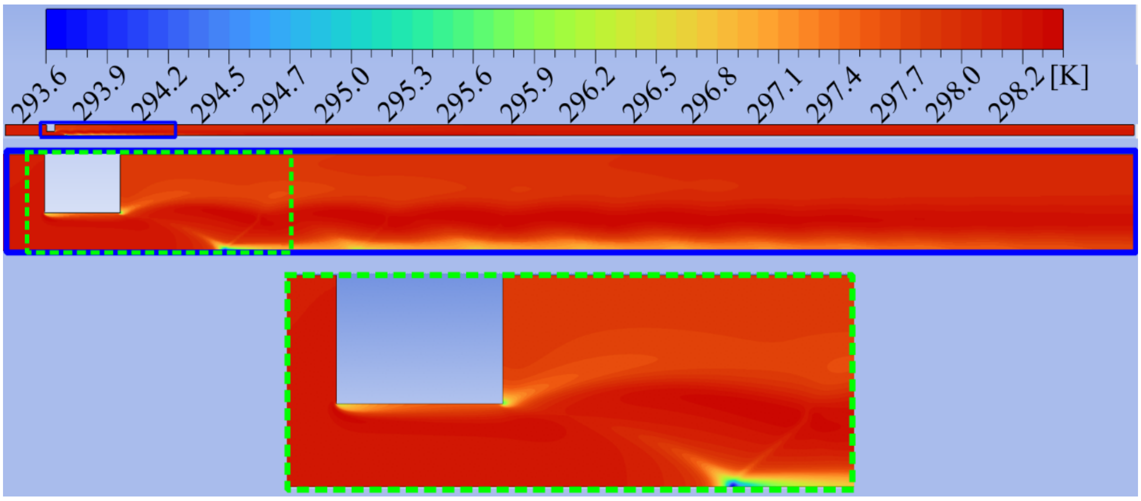

Figure 32 – Total temperature contours of case 4 (laminar with P_b/P_0 = 0.20, choked).

The same correspondence for the shock waves can be noted in Figure 33, as regards the total pressure.

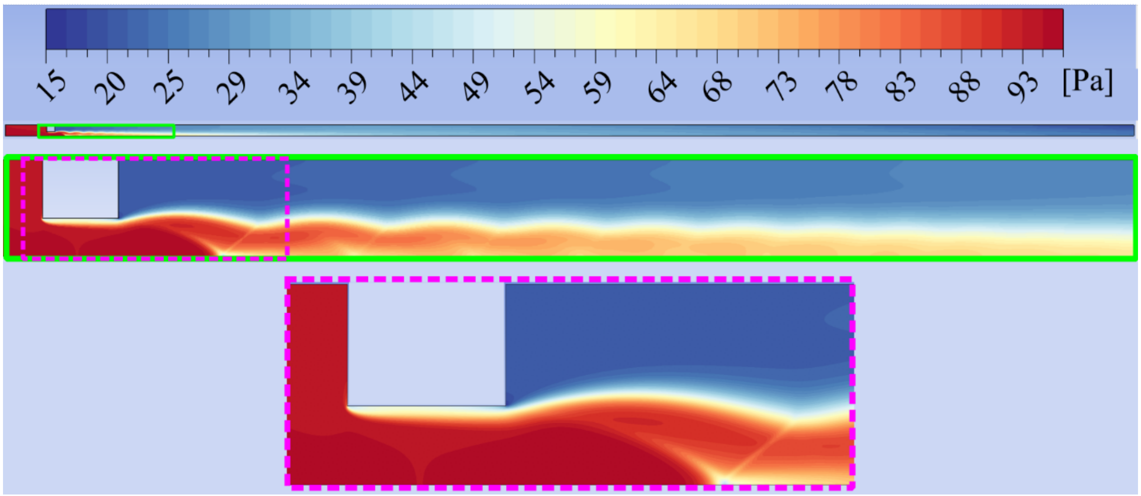

Figure 33 – Total pressure contours of case 4 (laminar with P_b/P_0 = 0.20, choked).

5.2.4 Case 4 - Turbulent

The contours and streamlines for the geometric case 4 with turbulent conditions are presented next. The chosen P_b/P_0 is 0.36, which is the lower P_b/P_0 considering two digits for single-phase UF_6 with choked flow.

Figure 34 shows how the flow filed is close to deposition saturation in the lower P_b/P_0. It was performed by the unity simulations with respect to case 4 (turbulent).

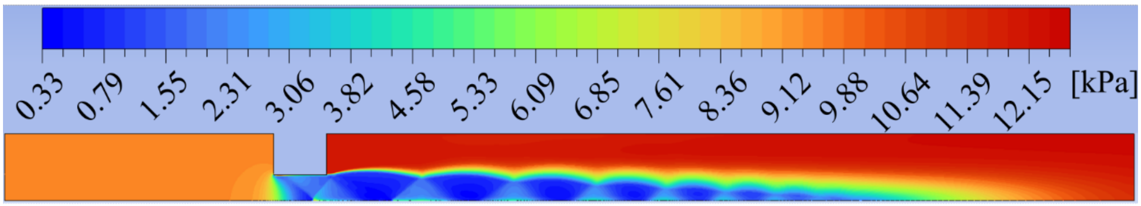

Figure 34 – Deposition proximity contours of case 4 (turbulent with P_b/P_0 = 0.36, choked).

As mentioned before, Prandtl-Meyer expansions, oblique shock waves and a small normal shock wave can be observed through Mach contours in Figure 35.

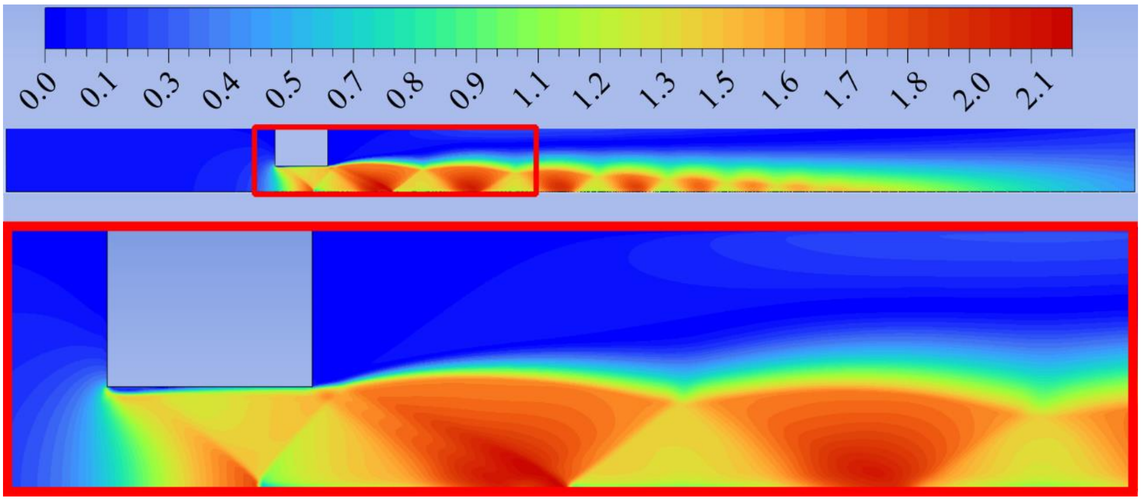

Figure 35 – Mach number contours of case 4 (turbulent with P_b/P_0 = 0.36, choked).

Besides the restricted main flow in the orifice, recirculation flow structures can be seen through the streamlines of Figure 36.

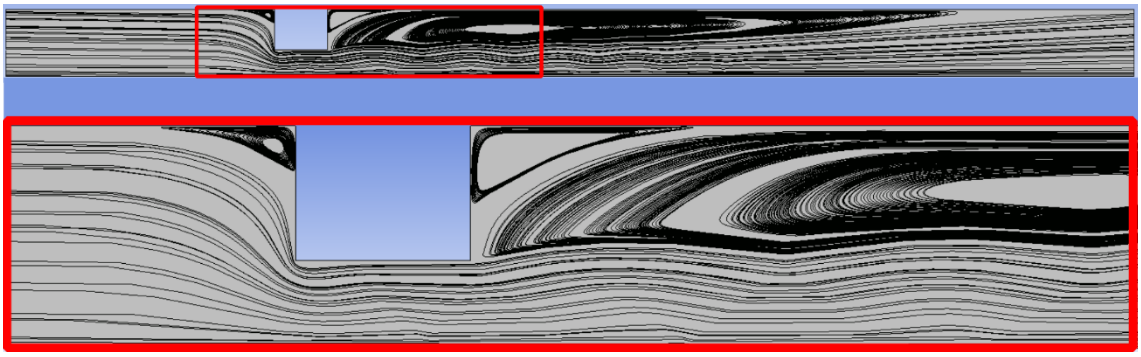

Figure 36 – Streamlines of case 4 (turbulent with P_b/P_0 = 0.36, choked).

Total temperature contours of Figure 37 depict the near constancy of this property throughout the domain, even though considerable stratification is present due to effective diffusivity of turbulence.

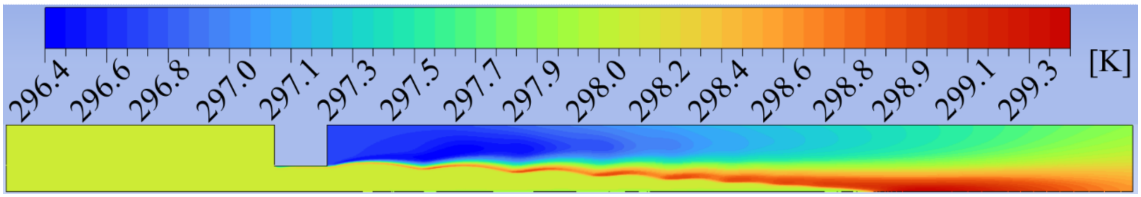

Figure 37 – Total temperature contours of case 4 (turbulent with P_b/P_0 = 0.36, choked).

Total pressure contours are presented by Figure 38. The shortening of the total pressure scale was used in the down-right part of Figure 38 to emphasize the discontinuities related to shock waves as shown in Figure 35.

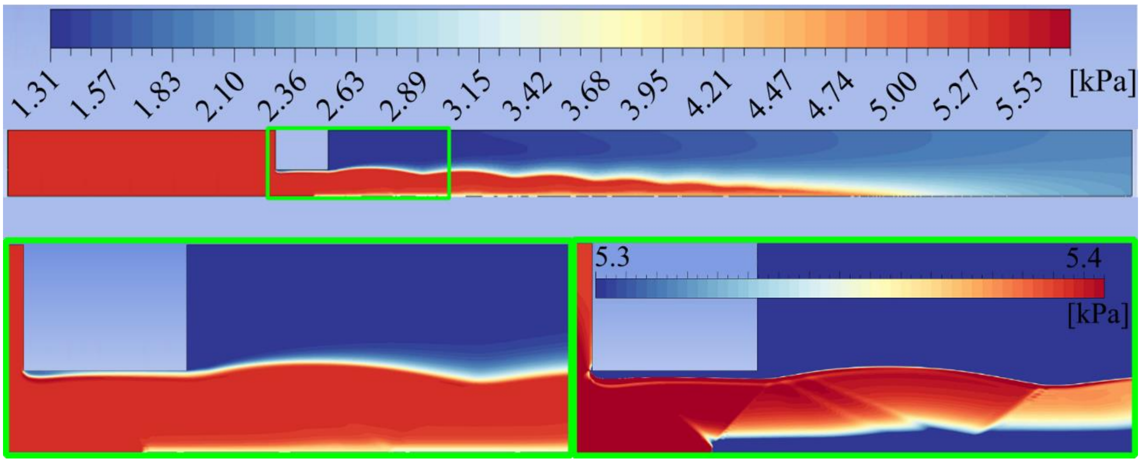

Figure 38 – Total pressure contours of case 4 (turbulent with P_b/P_0 = 0.36, choked).

5.2.5 Case 13 - Laminar

The contours and streamlines for the geometric case 13 with laminar conditions are presented next. The chosen P_b/P_0 is 0.40 and choked flow was not achieved yet. Choking was noticed only when P_b/P_0 was further reduced (0.20 – 0.10 range).

Mach number contours are presented by Figure 39, on which red and dark orange regions represent Prandtl-Meyer expansion fans. Oblique shock waves are present as well.

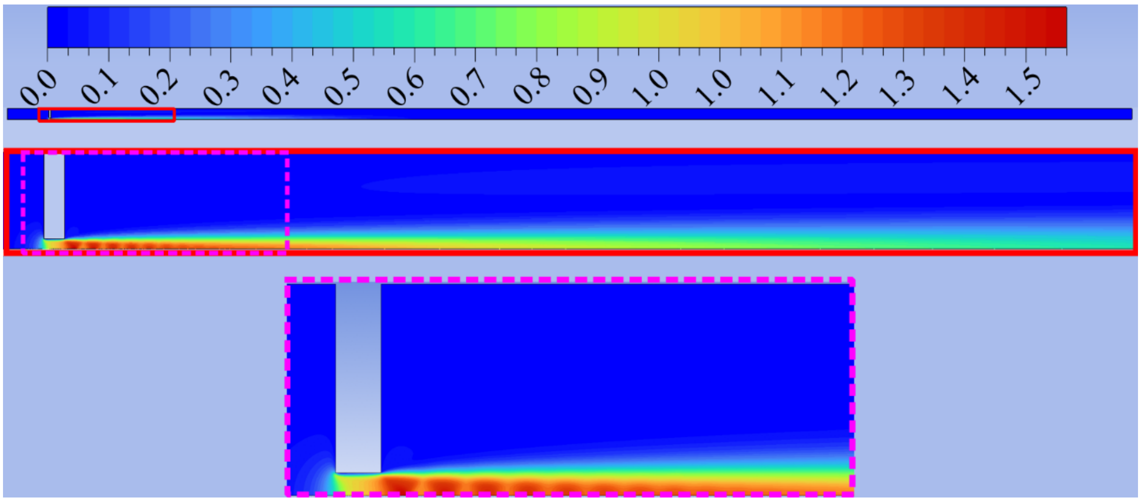

Figure 39 – Mach number contours of case 13 (laminar with P_b/P_0 = 0.40, not choked yet – only with further reduction of P_b/P_0).

Complementary to Figure 39, Figure 40 shows the constriction of the streamlines as well as extensive recirculation flows since the flow is laminar.

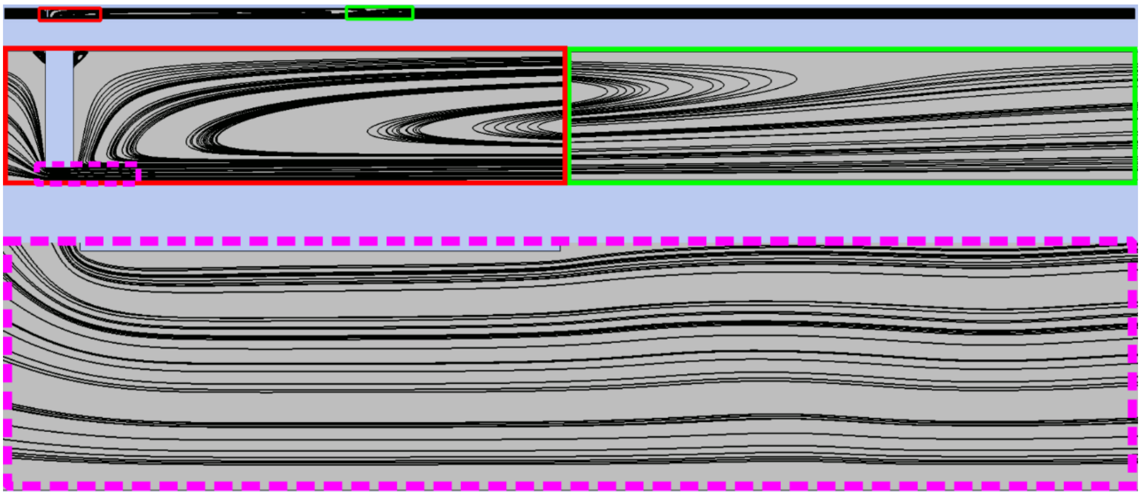

Figure 40 – Streamlines of case 13 (laminar with P_b/P_0 = 0.40, not choked yet – only with further reduction of P_b/P_0).

Total temperature contours of almost uniform color are shown in Figure 41 to validate the solution in terms of thermodynamics' first law.

Total pressure decreasing and subtle discontinuities can be noted in the jet region of Figure 42. These discontinuities correlate to the oblique shock waves in Figure 39.

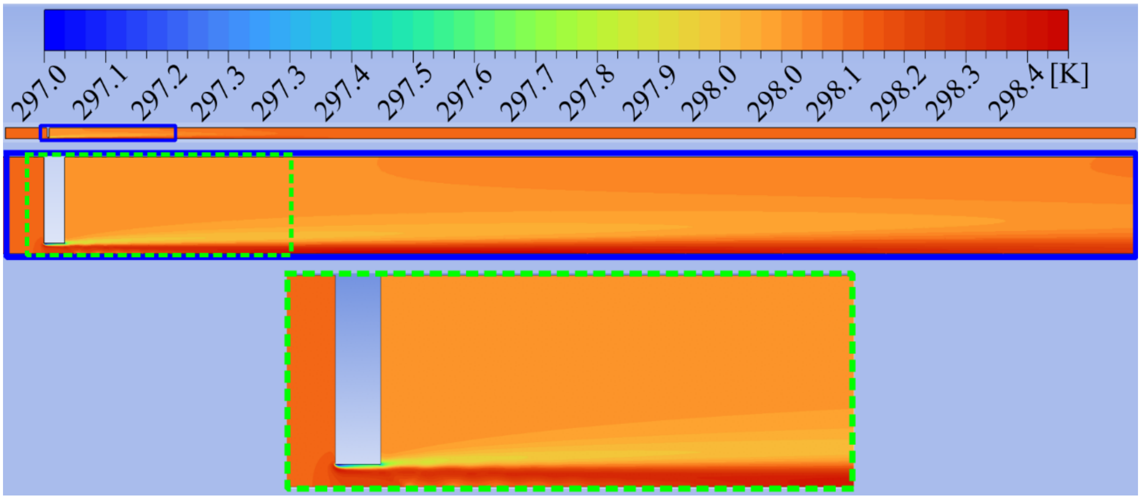

Figure 41 – Total temperature contours of case 13 (laminar with $P_b/P_0 = 0.40$, not choked yet – only with further reduction of P_b/P_0).

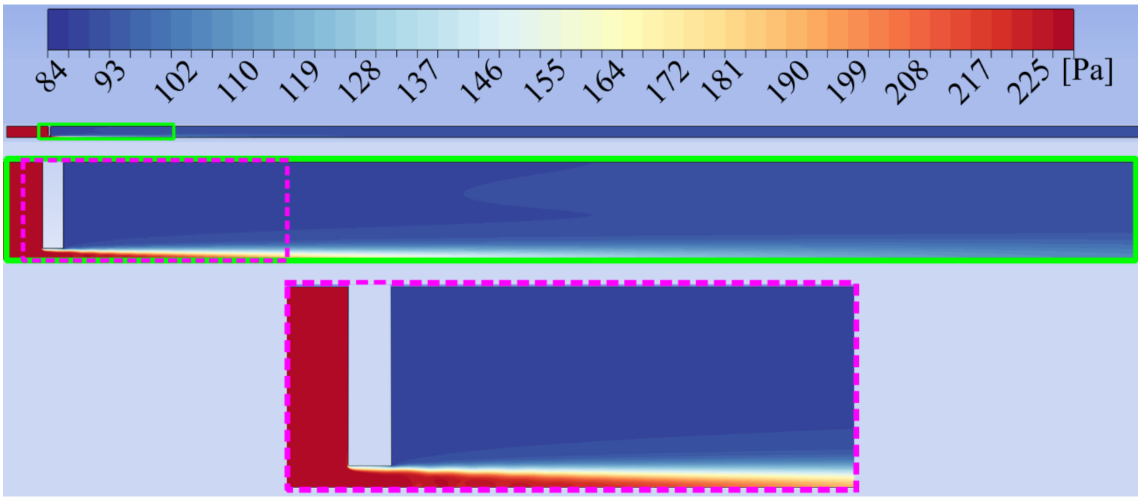

Figure 42 – Total pressure contours of case 13 (laminar with $P_b/P_0 = 0.40$, not choked yet – only with further reduction of P_b/P_0).

5.2.6 Case 13 - Turbulent

The contours and streamlines for the geometric case 13 with turbulent conditions are presented next, where the flow is choked. The chosen P_b/P_0 is 0.40, which is the lower P_b/P_0 considering two digits for single-phase UF_6.

Saturation proximity pressure field is shown by Figure 43.

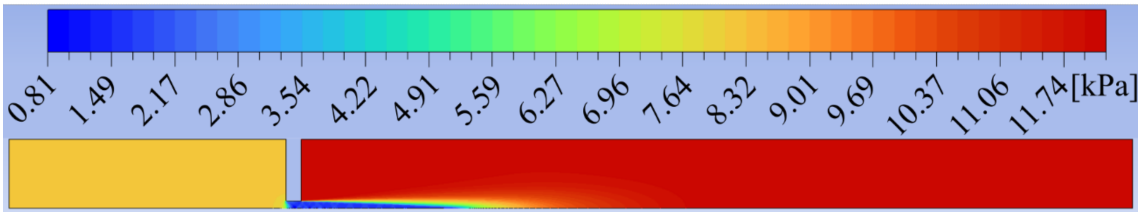

Figure 43 – Deposition proximity contours of case 13 (turbulent with $P_b/P_0 = 0.40$, choked).

Several oblique shock waves are represented by means of Mach number contours of Figure 44.

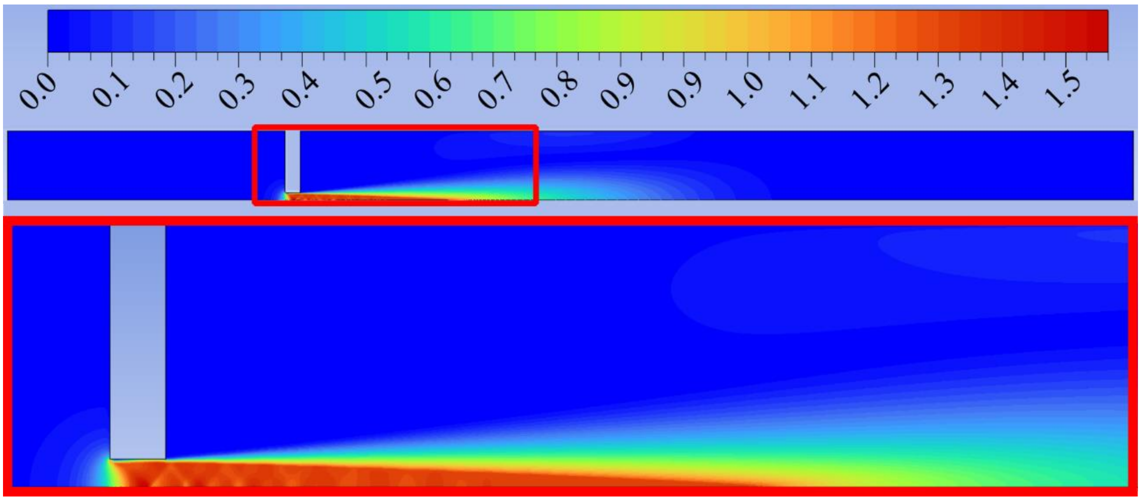

Figure 44 – Mach number contours of case 13 (turbulent with P_b/P_0 = 0.40, choked).

Complementarily, streamlines depict main and secondary flows in Figure 45.

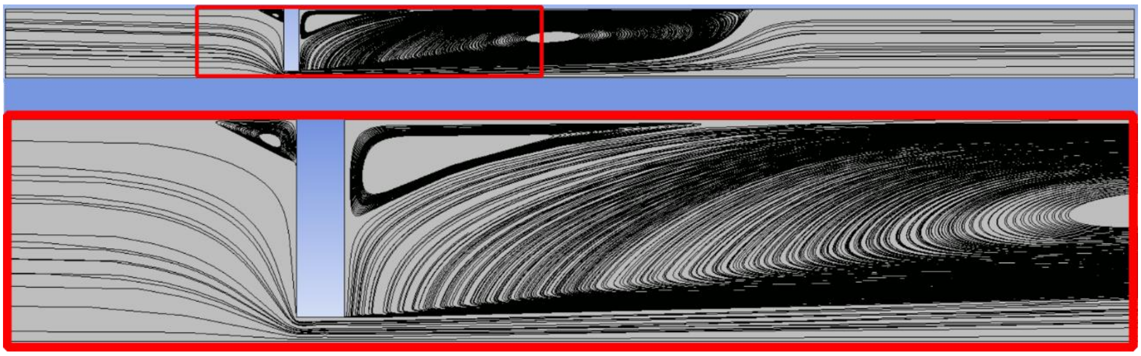

Figure 45 – Streamlines of case 13 (turbulent with P_b/P_0 = 0.40, choked).

Total temperature contours of Figure 46 depicted well the energy balance by the uniform light blue tone with little diffusivity around the jet.

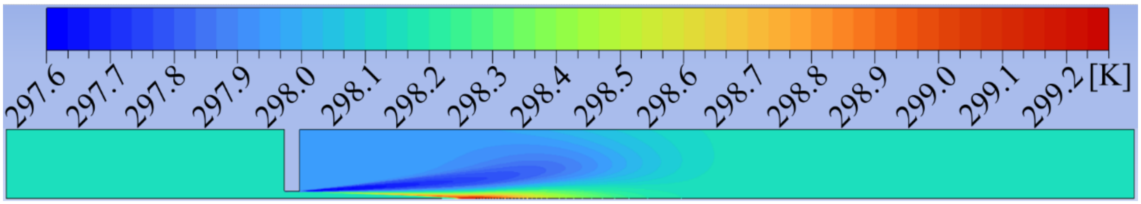

Figure 46 – Total temperature contours of case 13 (turbulent with P_b/P_0 = 0.40, choked).

Shortening of the total pressure scale was used in the down-right of Figure 47 to reveal discontinuities related to shock wave structures as depicted by Figure 44.

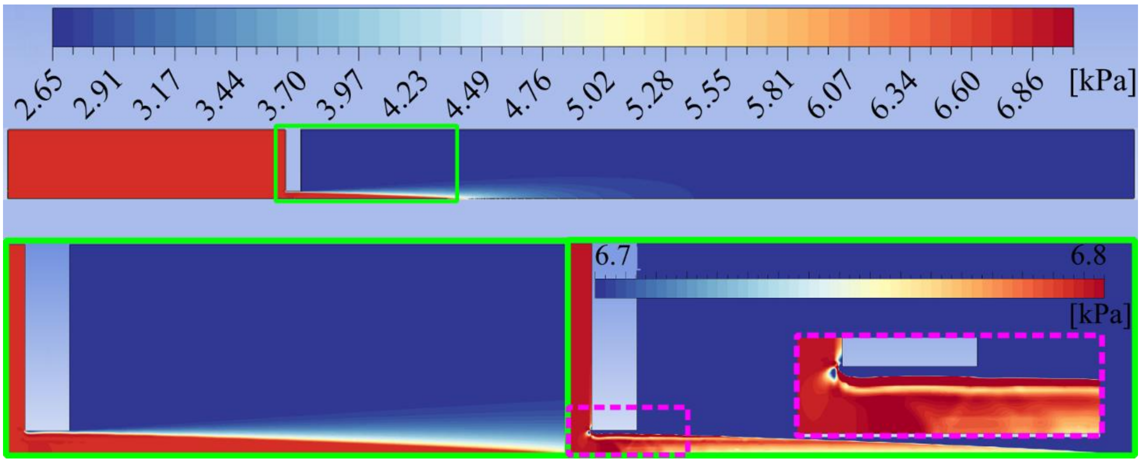

Figure 47 – Total pressure contours of case 13 (turbulent with $P_b/P_0 = 0.40$, choked).

5.2.7 Case 20 - Laminar

The contours and streamlines for the geometric case 20 with laminar conditions are presented next. The chosen P_b/P_0 is 0.30 and choked flow was achieved.

As already stated, laminar counterpart of Case 20 was the only laminar simulation to present deposition for the studied P_b/P_0 range. Thus, Figure 48 is useful to depict how the flow field is close to saturation. Dark blue regions are the flow regions closest to deposition.

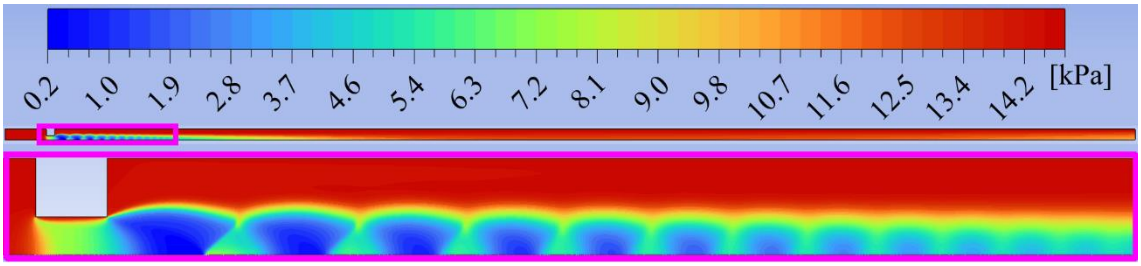

Figure 48 – Deposition proximity contours of case 20 (laminar with $P_b/P_0 = 0.30$, choked).

Flow structures like Prandtl-Meyer expansions and oblique shock waves are presented by Figure 49 through Mach number contours.

A normal shock wave can also be observed downstream of the orifice as the yellow line between the red and blue (maximum and minimum on the color scale) regions along the centerline of the pipe-orifice set in Figure 49.

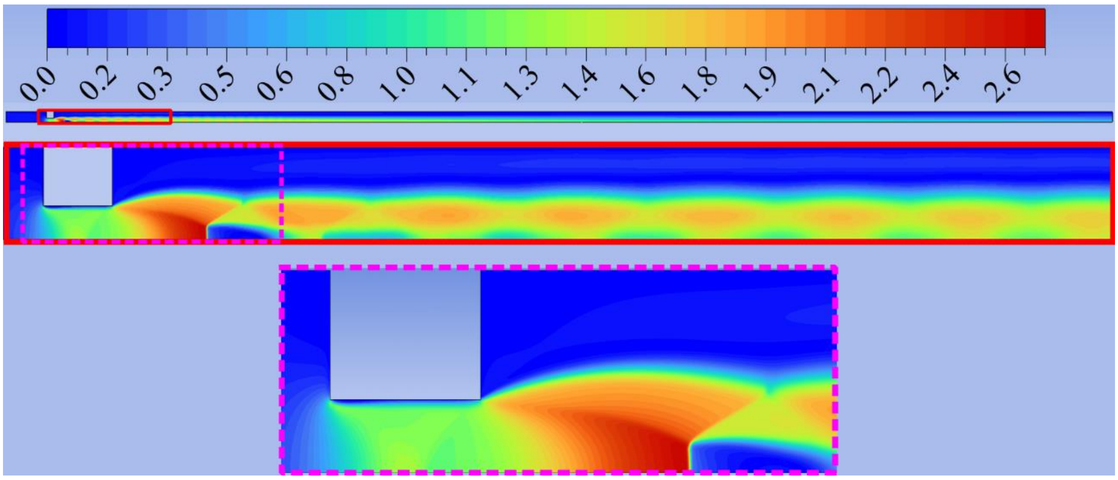

Figure 49 – Mach number contours of case 20 (laminar with P_b/P_0 = 0.30, choked).

The change in properties across this type of shock wave might be considerably high. The Mach number, for example, cannot decrease more than the predicted by Equation 64 (ANDERSON, 2017), which relates the Mach number in front of and behind the normal shock wave, respectively, Ma_1 and Ma_2, as follows:

$$Ma_2^2=\frac{1+[(\gamma-1)/2]Ma_1^2}{\gamma Ma_1^2-(\gamma-1)/2} \qquad \text{Equation 64}$$

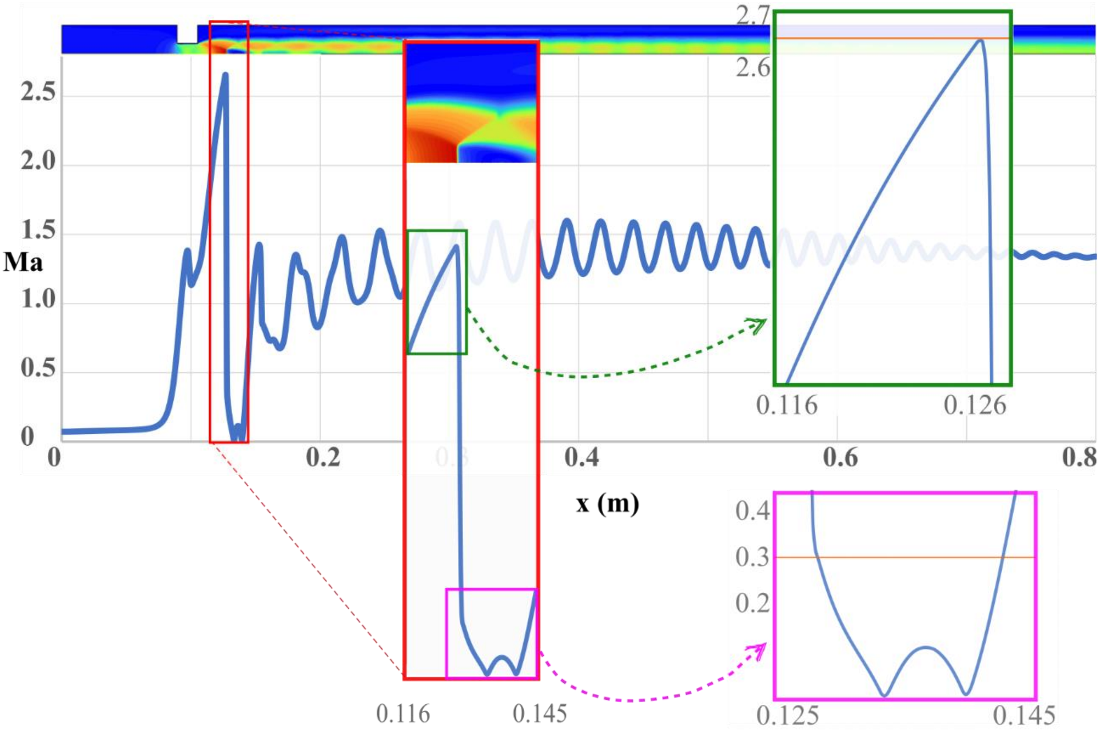

Figure 50 – Mach number of case 20 (laminar with P_b/P_0 = 0.30, choked) varying along the centerline r=0 to highlight the change of Ma through a normal shock wave, bounded by

Equation 64.

Figure 50 shows the Mach number plotted following the pipe-orifice centerline in a way both Ma_1 (2.66) and Ma_2 (approximately 0.30) can be observed for the aforementioned normal shock wave through orange horizontal lines. If Ma_1 value is plugged into Equation 64, the estimated Ma_2 found is 0.33. Thus, Ma_2 observed in the line plot should not be higher than this value, which is the case.

Therefore, the solution of laminar case 20 could be further checked by complying with the limit imposed by Equation 64.

Streamlines depicting primary and secondary flow structures are shown in Figure 51.

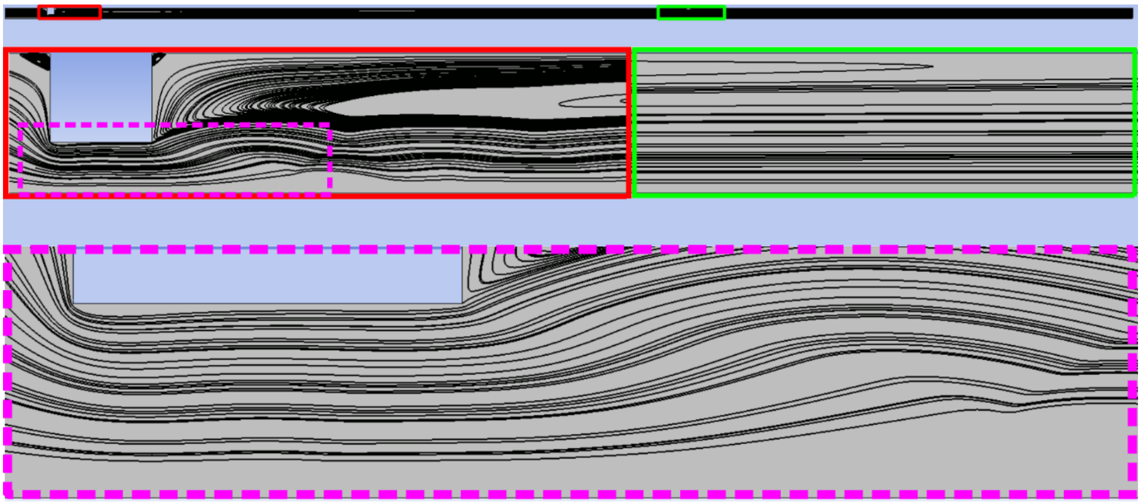

Figure 51 – Streamlines of case 20 (laminar with $P_b/P_0 = 0.30$, choked).

Total temperature contours are relatively homogeneous in color throughout the domain as seen in the top part of Figure 52. Some stratification of total temperature can be noted downstream of the orifice as a result of the diffusion of this property. Additionally, total temperature discontinuities can be seen in central and down parts of Figure 52 and correlate well with discontinuities of Figures 49 and 53.

Figure 53 shows the total pressure decrease downstream of the orifice. Additionally, normal and oblique shock waves can be seen and correspond with those shown by Mach number and total temperature contours.

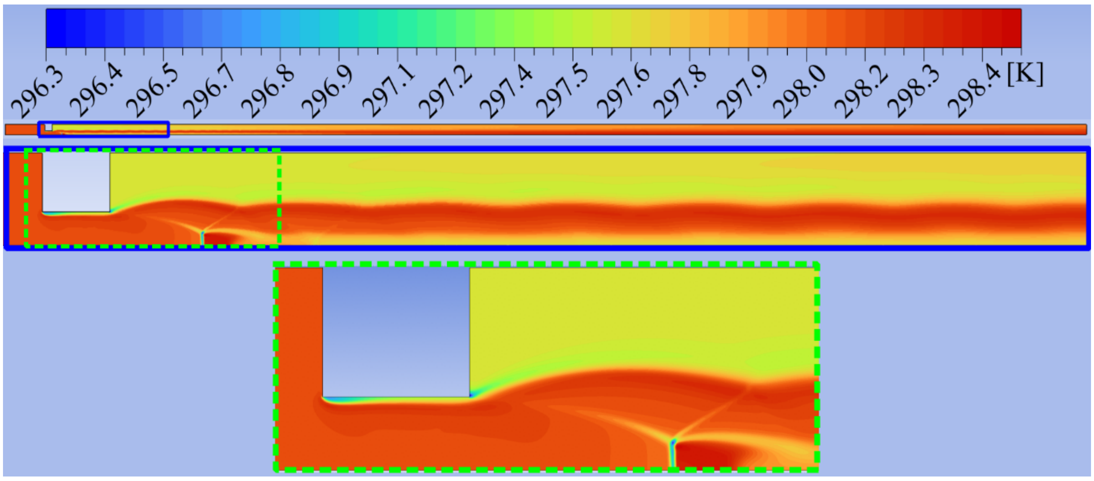

Figure 52 – Total temperature contours of case 20 (laminar with $P_b/P_0 = 0.30$, choked).

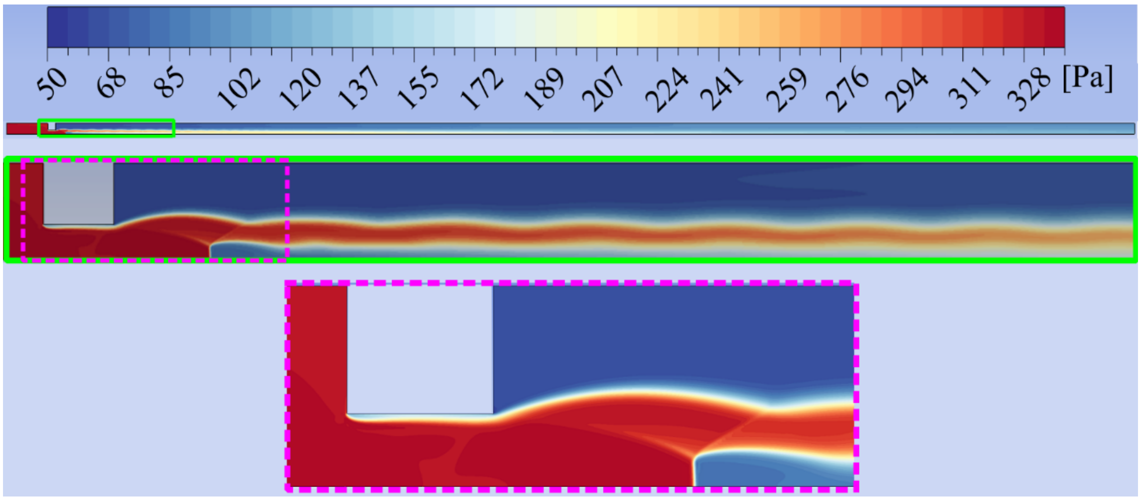

Figure 53 – Total pressure contours of case 20 (laminar with $P_b/P_0 = 0.30$, choked).

5.2.8 Case 20 - Turbulent

The contours and streamlines for the geometric case 20 with turbulent conditions are presented next, where the flow is choked. The chosen P_b/P_0 is 0.50, which is the lower P_b/P_0 considering two digits for single-phase UF_6.

The deposition proximity pressure field is presented by Figure 54.

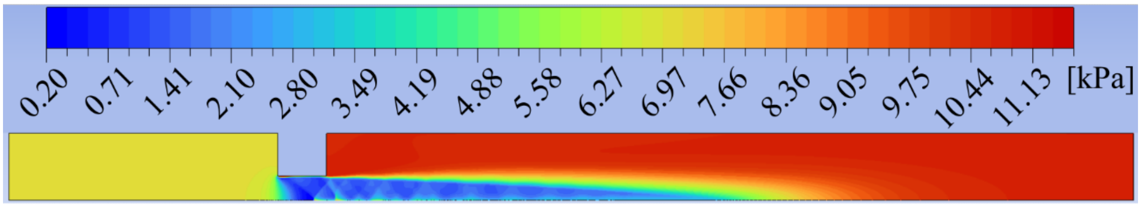

Figure 54 – Deposition proximity contours of case 20 (turbulent with $P_b/P_0 = 0.50$, choked).

Many oblique and some normal shock waves are shown downstream of the orifice by Figure 55.

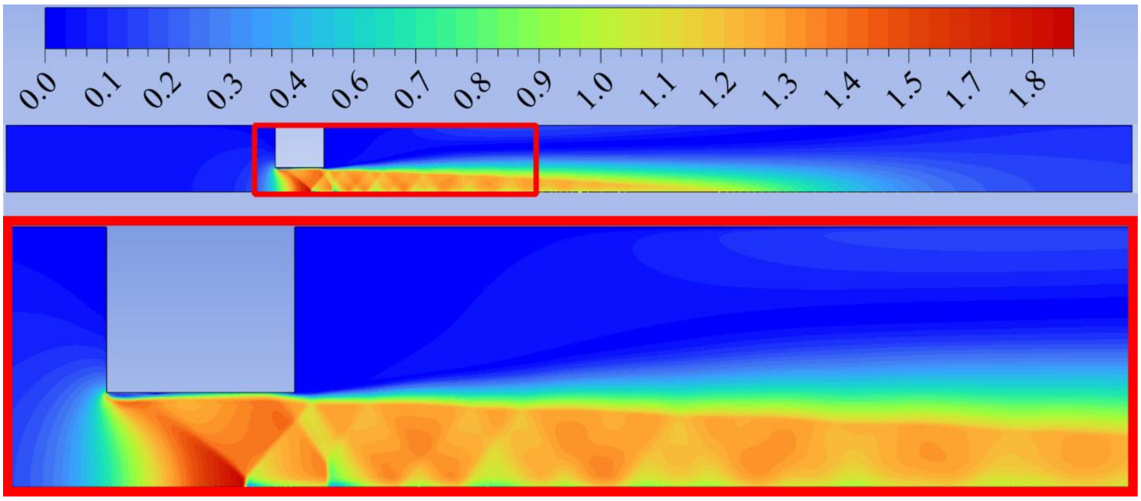

Figure 55 – Mach number contours of case 20 (turbulent with P_b/P_0 = 0.50, choked).

The streamlines as regards turbulent case 20 are shown by Figure 56.

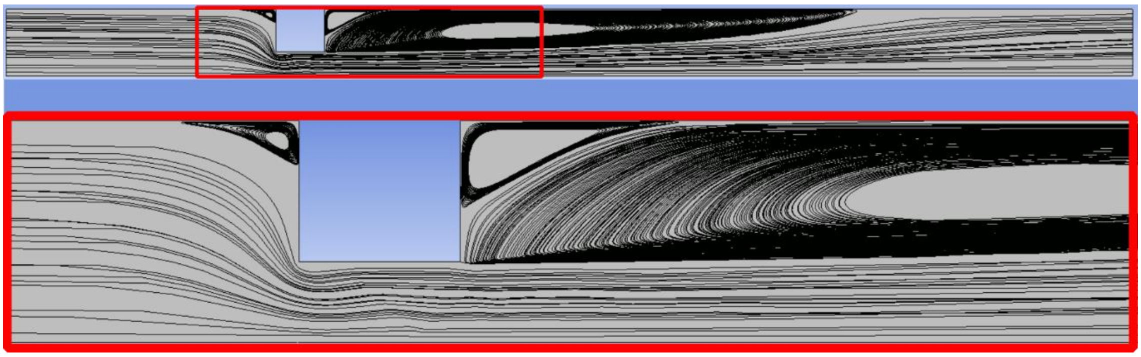

Figure 56 – Streamlines of case 20 (turbulent with P_b/P_0 = 0.50, choked).

Total temperature contours serve to illustrate thermodynamics' first law in Figure 57. In addition, considerable diffusion of total temperature is observed downstream the orifice as seen for the other turbulent cases.

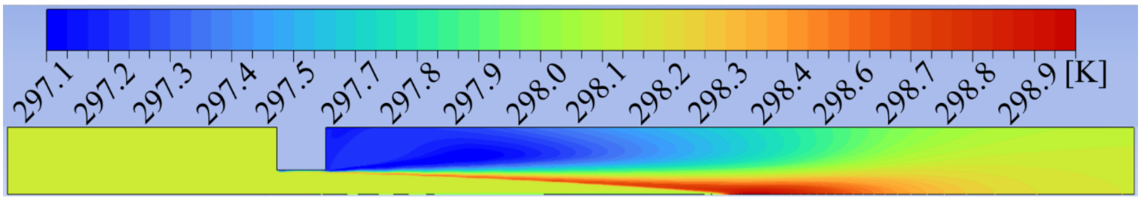

Figure 57 – Total temperature contours of case 20 (turbulent with P_b/P_0 = 0.50, choked).

Shortening of the total pressure scale was used in the down-right of Figure 58, so that total pressure discontinuities related to shock waves shown in Figure 55 are highlighted.

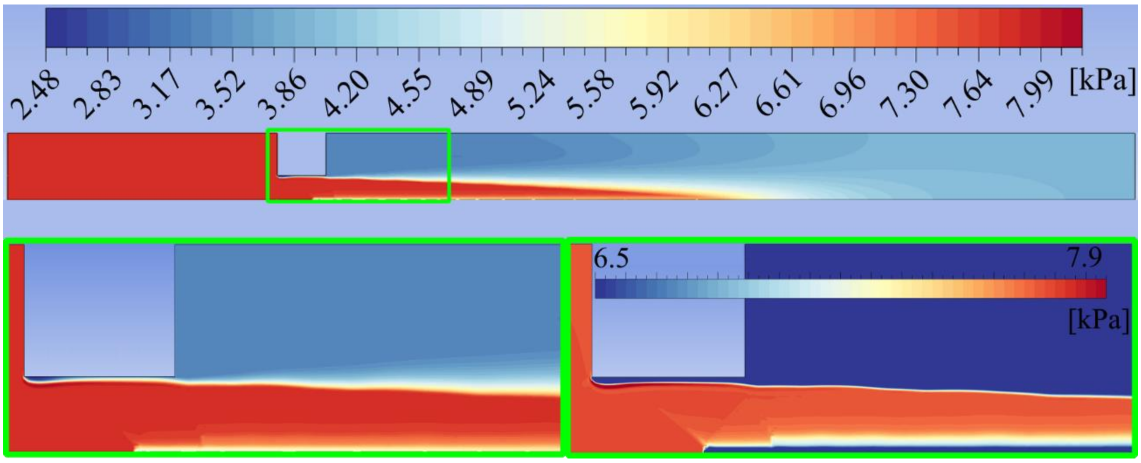

Figure 58 – Total pressure contours of case 20 (turbulent with P_b/P_0 = 0.50, choked).

5.3 DISCHARGE COEFFICIENTS OBTAINED

For each laminar case at least 5 simulations were performed with P_b/P_0 values of 0.50, 0.40, 0.30, 0.20, and 0.10. The observed behavior throughout the laminar cases is that they choke for lower P_b/P_0 than turbulent cases where only eighteen cases showed choking. Regarding the proximity of the deposition condition, only case 20 presented it for the P_b/P_0 range studied. Therefore, additional unity simulations were performed for case 20 to inspect the minimum working P_b/P_0 with precision of two digits, which was 0.18. Cases 1 and 20 are given as examples in Figure 59 to illustrate laminar and turbulent subset results.

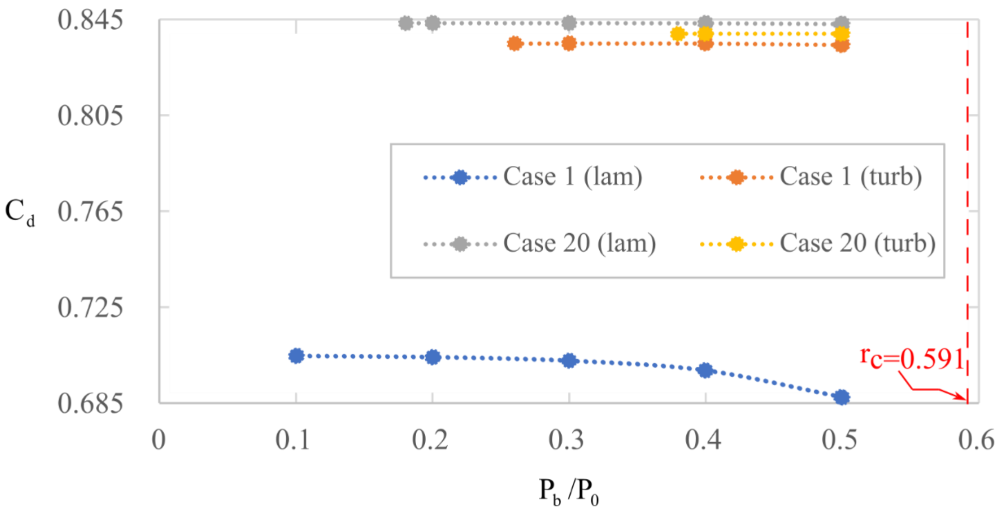

Figure 59 – Results of cases 1 and 20 for laminar and turbulent subsets.

Laminar cases spanned all planned unity simulations for P_b/P_0 from 0.1 to 0.5, except for case 20, which presented deposition. Laminar case 1 spanned the complete P_b/P_0 range, but did not resulted in choking. All results regarding the laminar cases are shown in Table 12.

Table 12 – The results for the 20 laminar cases: C_d values for each case evaluated for P_b/P_0 values of 0.5, 0.4, 0.3, 0.2, and 0.1*.

Case number	**P_b/P_0**					**Choked mass flow rate [kg/s]**
	0.5	**0.4**	**0.3**	**0.2**	**0.1***	
1	0.687	0.699	0.703	0.704	0.705	0.0000113**
2	0.749	0.757	0.759	0.760	0.760	0.0000332
3	0.787	0.792	0.793	0.794	0.794	0.0000733
4	0.813	0.816	0.816	0.817	0.817	0.000137
5	0.736	0.744	0.747	0.748	0.748	0.0000142
6	0.782	0.788	0.789	0.790	0.790	0.0000442
7	0.809	0.812	0.813	0.813	0.813	0.0000970
8	0.827	0.829	0.829	0.829	0.829	0.000178
9	0.784	0.790	0.791	0.791	0.792	0.0000359**
10	0.813	0.816	0.816	0.817	0.817	0.0000898
11	0.829	0.831	0.831	0.831	0.831	0.000175
12	0.840	0.841	0.841	0.841	0.841	0.000296
13	0.779	0.785	0.787	0.788	0.788	0.0000241
14	0.812	0.816	0.817	0.817	0.817	0.0000766
15	0.829	0.831	0.831	0.831	0.831	0.000165
16	0.840	0.840	0.841	0.841	0.841	0.000294
17	0.805	0.810	0.811	0.811	0.811	0.0000512
18	0.825	0.828	0.829	0.829	0.829	0.000131
19	0.836	0.837	0.837	0.837	0.837	0.000255
20	0.843	0.844	0.844	0.844	0.844*	0.000427

* Case 20 would present deposition in the lower range of P_b/P_0. The actual lower P_b/P_0 (up to two-digit decimal) studied regarding UF_6 as a single-phase gas was 0.18. **Cases 1 and 9 did not choke under the pressure ratio range studied, so that these values are the related maximum mass flow rate.

As shown in Table 12, only case 9 also did not achieved choking for the P_b/P_0 range studied of the laminar cases.

The single-phase working range was considerably shorter for the turbulent cases, since deposition was achieved for higher values of P_b/P_0, that is, from 0.26-0.39. All cases presented choking and its range was far wider with at least 0.10 for all cases and at least 0.20 for five cases. This behavior is depicted by cases 20 and 1, respectively, in Figure 59.

At least four unity simulations were performed for each of the turbulent cases and the lower single-phase P_b/P_0 was also determined with two-digits precision. The results for the turbulent cases are shown in Table 13.

Table 13 – The results for the 20 turbulent cases: C_d values for each case evaluated for P_b/P_0 values of 0.5, 0.4, 0.3, and 0.2.

Case number	**P_b/P_0**				**Choked mass flow rate [kg/s]**	**Lower single-phase P_b/P_0**
	0.5	**0.4**	**0.3***	**0.2***		
1	0.835	0.835	0.835	0.835*	0.00134	0.26
2	0.836	0.836	0.836	0.836*	0.00290	0.28
3	0.838	0.838	0.838*	-	0.00513	0.32
4	0.841	0.841	0.841*	-	0.00810	0.36
5	0.833	0.836	0.836	0.836*	0.00081	0.27
6	0.835	0.835	0.835	0.835*	0.00215	0.28
7	0.836	0.836	0.836*	-	0.00420	0.31
8	0.839	0.839	0.839*	-	0.00703	0.35
9	0.834	0.835	0.835	0.835*	0.00138	0.28
10	0.835	0.835	0.835	-	0.00315	0.30
11	0.837	0.837	0.837*	-	0.00572	0.34
12	0.840	0.840	0.840*	-	0.00914	0.37
13	0.835	0.838	0.838	-	0.00076	0.30
14	0.835	0.835	0.835	-	0.00222	0.30
15	0.836	0.836	0.836*	-	0.00452	0.33
16	0.838	0.838	0.838*	-	0.00771	0.37
17	0.835	0.835	0.835*	-	0.00134	0.31
18	0.835	0.835	0.835*	-	0.00327	0.33
19	0.837	0.837	0.837*	-	0.00611	0.39
20	0.839	0.839	0.839*	-	0.00994	0.38

* The actual lower P_b/P_0 (up to two-digit decimal) studied regarding UF_6 as a single-phase gas was that given by the last (rightmost) column.

5.4 CORRELATION OF THE CRITICAL DISCHARGE COEFFICIENT

5.4.1 The obtaining of a correlation

The simulations for the laminar subset served only as illustrative work since data are not available even for common working fluids such as air. Thus, graphs of C_d (and C_d^*) against the two studied factors are presented to illustrate the lack of fitting function for the laminar subset. The graph of C_d (and C_d^*) against P_0 is shown in Figure 60.

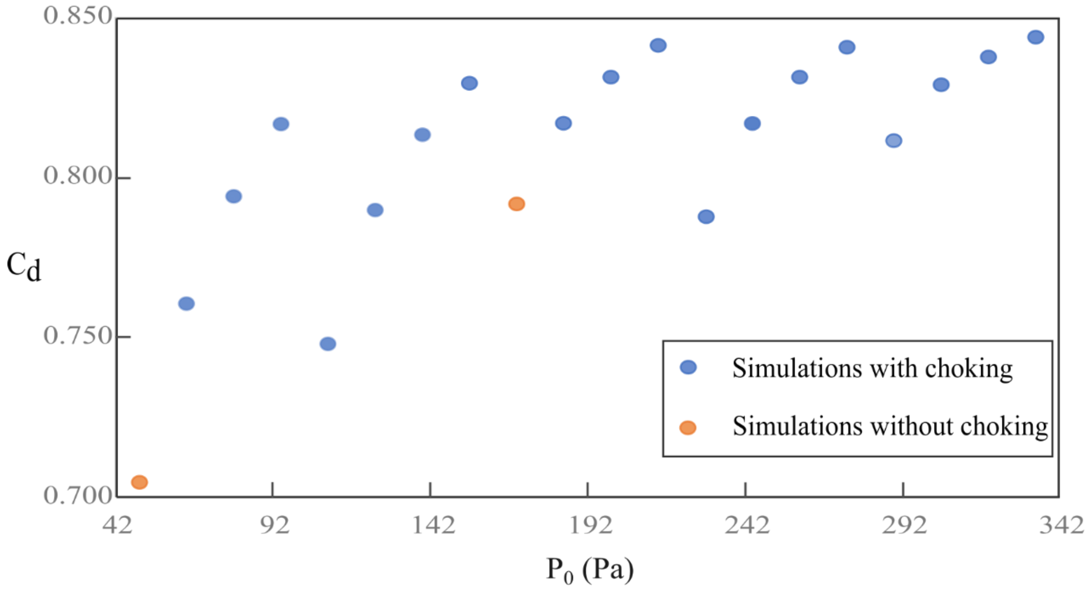

Figure 60 – C_d against P_0 for the laminar subset. The erratic behavior could not be fitted with polynomials tested.

Likewise, the plot of Cd (and Cd*) values could not present any adequate fitting with respect to β as shown in Figure 61.

The erratic behavior is similar to the simulation results of Metwally (2014), performed in a similar range for the Reynolds number Re. Thus, no correlation was obtained for the laminar subset and it should be allied with physical experiments in future research.

The simulations for the turbulent subset were found to present no recognizable pattern of C_d^* with parameter P_0. Instead, C_d^* showed polynomial fit with parameter β.

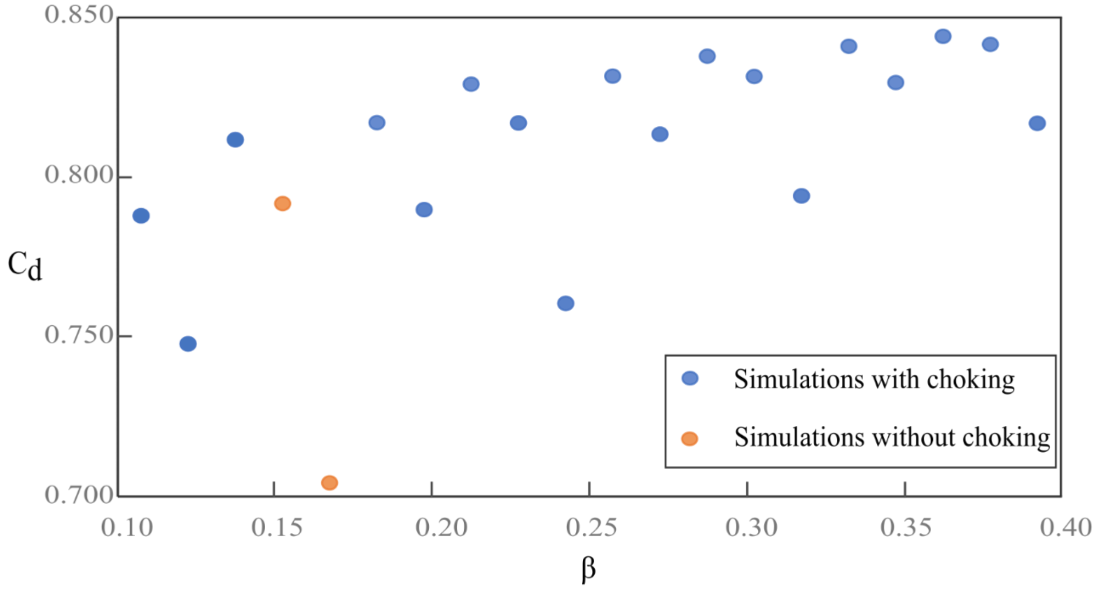

Figure 61 – C_d against β for the laminar subset. The erratic behavior could not be fitted with polynomials.

Thus, C_d (and C_d^*) values for the laminar subset are plotted against P_0 in Figure 62 and the behavior is noticeably erratic. No fitting polynomial function could be adjusted to data.

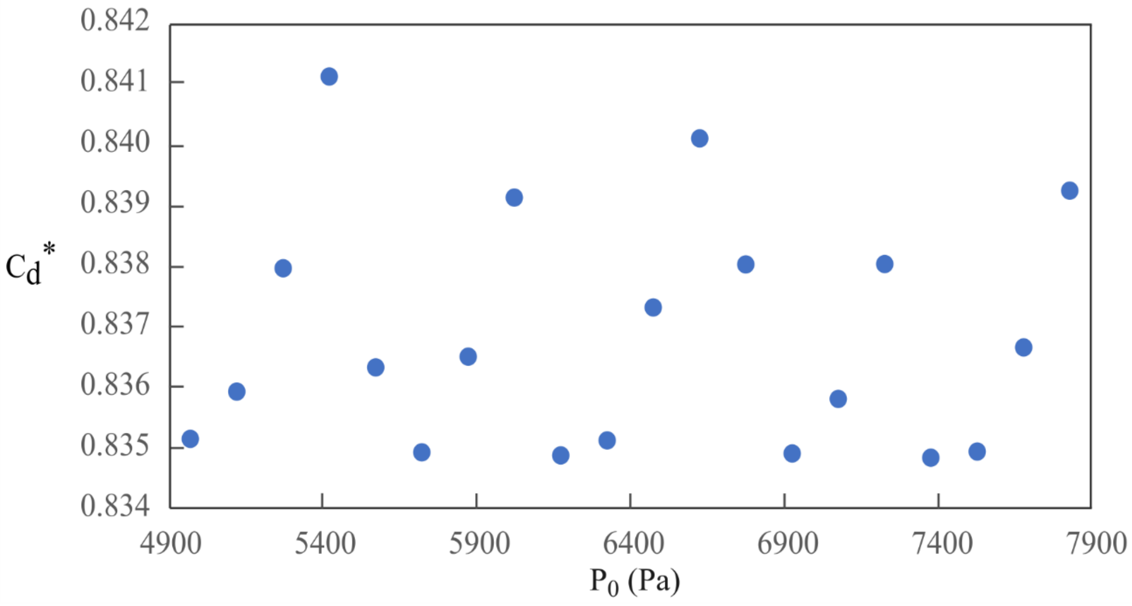

Figure 62 – C_d^* against P_0 for the turbulent subset. No fitting function was found.

As regards the factor β, C_d^* behaved well in a polynomial fashion. Therefore, fitting polynomials of degrees 1 to 8 were tested with the least-squares method.

The square of the standard error of the regression, s^2, is used to evaluate the fitting accuracy of each regression to the data:

$$s^2=\frac{\sum_1^n \varepsilon^2}{n\text{-}m\text{-}1} \qquad \text{Equation 65}$$

Where ε is the error between Cd* from the simulation and that from the predicting polynomial, n is the number of simulations (cases), and m is the degree of the polynomial.

Thus, Equation 65 is applied to all polynomials to compute s^2. The equations of the polynomials with the respective values of s^2 are presented in Table 14.

Table 14 – The polynomial fits for the correlation of C_d^* with β regarding the 20 turbulent cases.

m	Fitting equation	s^2 (• 10^7)
1	$0.0162\ \beta + 0{,}8327$	15.4
2	$0.1605\ \beta^2 – 0.0640\ \beta + 0.8416$	2.86
3	$– 0.6418\ \beta^3 + 0.6875\ \beta^2 – 0.1757\ \beta + 0.8494$	1.75
4	$6.6574\ \beta^4 – 7.2991\ \beta^3 + 3.0113\ \beta^2 – 0.5283\ \beta + 0.8678$	1.03
5	$– 34.832\ \beta^5 + 50.197\ \beta^4 – 28.213\ \beta^3 + 7.8121\ \beta^2 – 1.0522\ \beta + 0.8895$	1.04
6	$799.32\ \beta^6 – 1233.8\ \beta^5 + 775.67\ \beta^4 – 254.11\ \beta^3 + 45.8620\ \beta^2 – 4.3295\ \beta + 1.0020$	0.789
7	$– 3272.1\ \beta^7 + 6525.5\ \beta^6 – 5413.8\ \beta^5 + 2421.8\ \beta^4 – 630.93\ \beta^3 + 95.895\ \beta^2 – 7.8907\ \beta + 1.1067$	1.93
8	$37417\ \beta^8 – 78105\ \beta^7 + 70507\beta^6 – 35909\beta^5 + 11269\ \beta^4 – 2227.9\beta^3 + 270.76\ \beta^2 – 18.503\ \beta + 1.3801$	10.1

Also, the results of s^2 are plotted against the degree of the polynomials, as shown in Figure 63.

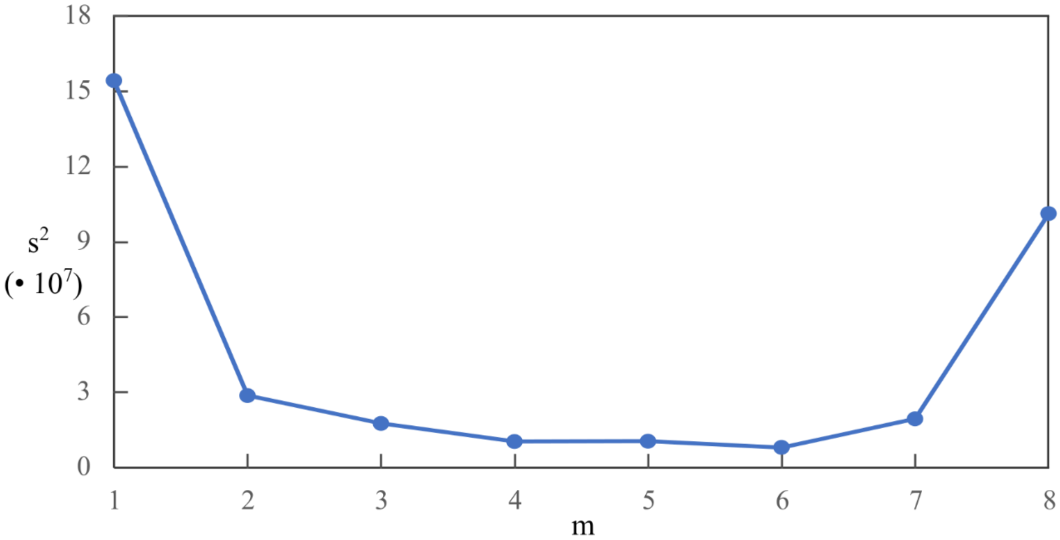

Figure 63 – The square of the standard error of the regressions s^2 against the degree of fitting polynomials m.

Aside from the linear fit and the 8th-degree polynomial, other polynomials approximate well the correlation of C_d^* with β. 6th and 2nd-degree constitute the best fit and the minimum-degree favorable fit.

In order to avoid overfitting, the 2nd-degree polynomial was chosen as a satisfactory fit to the data from simulations.

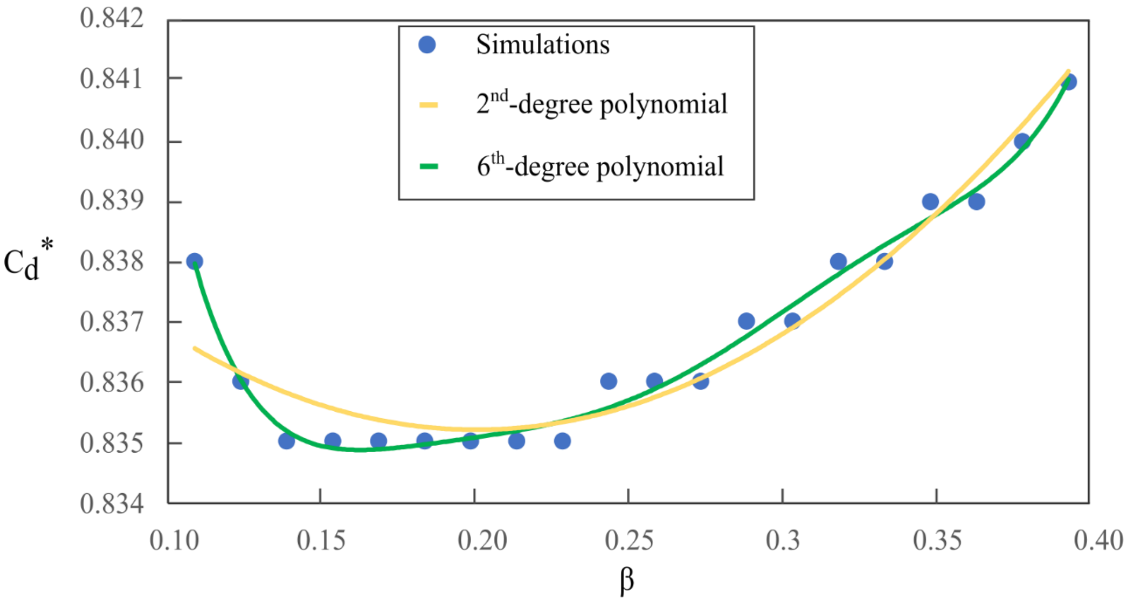

Figure 64 – Comparison of 2nd and 6th-degree polynomials in correlating C_d^* data with β. They constitute best fit and minimum-degree favorable fit, respectively.

Therefore, a correlation, show in Table 14, was attained for the turbulent subset with respect to the diameter ratio β.

Moreover, the values of C_d^* obtained from the simulations of the turbulent subset revealed to be very close to literature results, i.e., in the 0.82-0.84 range (GRACE; LAPPLE, 1951; JACKSON, 1964b; MILLER, 1983).

5.4.2 Correlation assessment by new simulated point in sampling space

In the sampling factor space, the new point with P_0=6775 Pa and β=0.34 was simulated through two unity simulations for which P_b/P_0=0.5 and P_b/P_0=0.4. The result was choked flow with C_d^*=0.838. Thus, the prediction error for the quadratic correlation given in second line of Table 14 could be assessed with respect to the output of the new simulation. With three-digit precision, the prediction error was zero. The synthesis of the correlation assessment is presented in Figure 65.

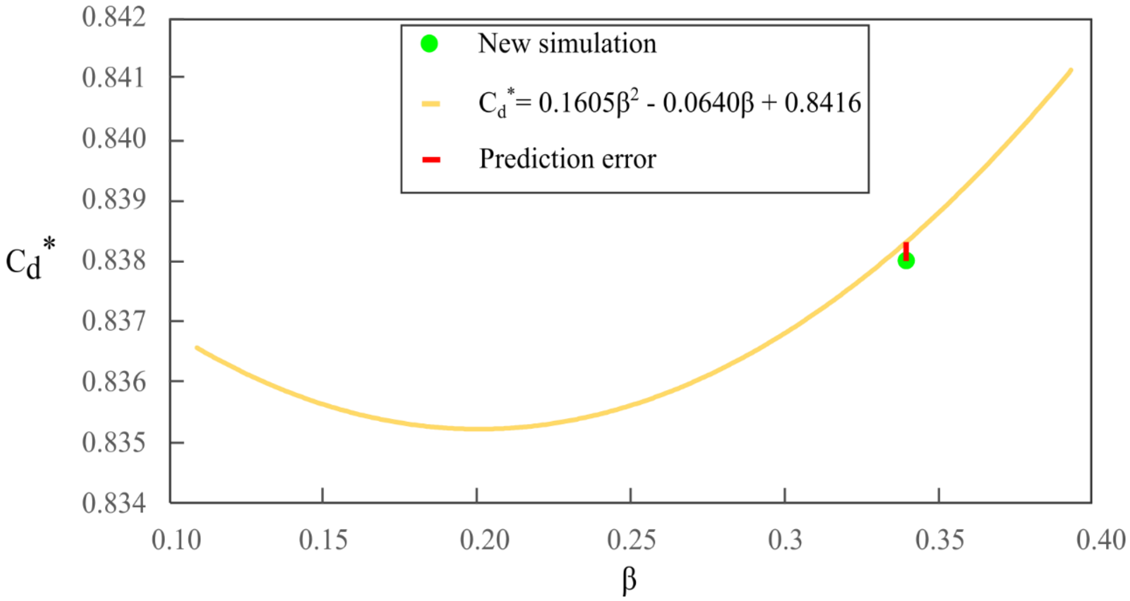

Figure 65 – Correlation assessment by new simulated point in sampling space. The prediction error with three-digit precision is zero and is depicted in red.

6 SUMMARY AND CONCLUSIONS

6.1 SUMMARY AND CONCLUSIONS

In the present work, a 2D AXSM CFD model was applied to study how the orifice discharge coefficient C_d^* behaves with two factors for the compressible flow of single-phase gaseous UF_6 through square-edged concentric orifices. The factors used were the diameters ratio β and the total inlet pressure P_0. Two subsets encompassing 20 case studies each were considered: i) laminar, and ii) turbulent.

The laminar subset was approached as an illustrative study, since no data is available in the literature in order to make a full validation. Several case studies did not present choking for the range of pressure ratio P_b/P_0 assumed, which was from 0.5 to 0.1. Moreover, erratic behavior was observed for C_d^* with respect to any of the factors even with only choked case studies were considered. In fact, the erratic behavior is similar to the simulation results of Metwally (2014), performed in a similar range for the Reynolds number Re. Thus, no correlation was obtained for the laminar subset and it might be work for further studies when allied with physical experiments.

As regards the turbulent subset of simulations, the C_d^* values found to be very close to literature values, i.e., in the 0.82-0.84 range (GRACE; LAPPLE, 1951; JACKSON, 1964b; MILLER, 1983). C_d^* also presented erratic behavior with P_0 and a fitting could not be attained with polynomial equations. C_d^* presented accurate polynomial fittings when correlated to β. Hence, polynomials of degrees 1 to 8 were tested and the 6th-degree polynomial was the best fit. The 2nd-degree polynomial was chosen as the fitting polynomial to avoid overfitting.

Even without experimental data nor performing a similarity analysis, it is remarkable how precise the calibration simulations fit with data from cases seen in literature in turbulent flow regimes. This depicts how powerful CFD is to framework and solve fluid flow problems. The correlation should be validated to be used in real case scenarios, with future work suggestion on collection of experimental data. Nonetheless, the process of obtaining the correlation serves the purpose of illustrative work and can be applied by working personnel of the sensitive nuclear area.

6.2 FUTURE WORK

As recommendations for future work, the choked flow of UF_6 can be further studied in the transition range as regards Reynolds number. This would implicate using more elaborate turbulence models to span the inlet total pressure to values between $4.9 \cdot 10^3$ and $7.9 \cdot 10^3$ Pa. Also, future works can focus on other parameters as factors such as pipe inside diameter, thickness-to-diameter ratio. In addition, uranium deposition could be inspected with some multiphase model.

7 REFERENCES

AMNACHE, A.; OMRI, M.; FRÉCHETTE, L. G. A silicon rectangular micro-orifice for gas flow measurement at moderate Reynolds numbers: design, fabrication and flow analyses. **Microfluidics and Nanofluidics**, v. 22, p. 1–10, 2018.

ANDERSON, B. W. **The analysis and design of pneumatic systems.** , 1967.

ANDERSON, J. D. **Fundamentals of Aerodynamics**. Sixth ed. [s.l: s.n.].

ANDERSON, J. D. **Hypersonic and High-Temperature Gas Dynamics, Third Edition**. [s.l: s.n.].

ARNBERG, B. T. Review of critical flowmeters for gas flow measurements. **Journal of Fluids Engineering, Transactions of the ASME**, v. 84, n. 4, p. 447–457, 1962.

BERTIN, J. J. J. J.; CUMMINGS, R. M. R. M. **Aerodynamics for engineers**. Sixth ed. [s.l.] Cambridge University Press, 2021.

BIRD, R. B.; STEWART, W. E.; LIGHTFOOT, E. N. **Transport Phenomena**. 2nd. ed. New York: John Wiley & Sons, Inc., 2002.

BLAZEK, J. **COMPUTATIONAL FLUID DYNAMICS Principles and Applications**. 3rd. ed. Oxford: Elsevier Ltd., 2015.

BOX, G. E. P.; HUNTER, J. S.; HUNTER, W. G. **Statistics for experimenters**. Second ed. Hoboken: John Wiley & Sons, Inc., 2005. v. 664

BRAIN, T.; REID, J. **Performance of small diameter cylindrical critical-flow nozzles**. [s.l: s.n.].

CELIK, I. B. et al. Procedure for estimation and reporting of uncertainty due to discretization in CFD applications. **Journal of Fluids Engineering, Transactions of the ASME**, v. 130, n. 7, p. 0780011–0780014, 2008.

CERVANTES, M. J.; ENGSTRÖM, T. F. Factorial design applied to CFD. **Journal of Fluids Engineering, Transactions of the ASME**, v. 126, n. 5, p. 791–798, 2004.

CLOSE, D. A.; PRATT, J. C. Improvements in collimator design for verification of uranium enrichment in gaseous centrifuge header pipes of diameter 4.45 cm and 10.16 cm. **Nuclear Inst. and Methods in Physics Research, A**, v. 257, n. 2, p. 406–411, 1987.

COHEN, K. P. **The Theory of isotope separation as applied to the large-scale production of U235**. [s.l.] McGraw-Hill, 1951. v. 1

DEWITT, R. **Uranium hexafluoride: a survey of the physico-chemical propertiesGat-280**. Portsmouth, OH (United States): [s.n.]. Disponível em: <http://scholar.google.com/scholar?hl=en&btnG=Search&q=intitle:URANIUM+HEXAFLUORIDE+:+A+SURVEY+O+F+THE+PHYSICO-CHEMICAL+PROPERTIES#0>.

EMDEN, R. Über die Ausströmungserscheinungen permanenter Gase. **Annalen der Physik**, v. 305, n. 9, p. 264–289, 1899a.

EMDEN, R. Über die Ausströmungserscheinungen permanenter Gase. **Annalen der Physik**, v. 305, n. 10, p. 426–453, 1899b.

FANG, L. et al. Numerical investigation on the flow characteristics and choking mechanism of cavitation-induced choked flow in a Venturi reactor. **Chemical Engineering Journal**, v. 423, n. May, p. 130234, 2021.

FERZIGER, J. H.; PERIC’, M.; STREET, R. L. **Computational Methods for Fluid Dynamics**. Fourth ed. Cham: Springer Nature Switzerland AG, 2020.

FLIEGNER, A. Ergebnisse einiger Versuche über das Ausströmen der atmosphärischen Luft. **Der Civilingenieur: Zeitschrift für das Ingenieurwesen**, p. 13–48, 1874.

FLIEGNER, A. Versuche über das Ausströmen der atmosphärischen Luft durch gut abgerundete Mündungen. **Der Civilingenieur: Zeitschrift für das Ingenieurwesen**, p. 443–510, 1877.

FLIEGNER, A. Versuche über das Ausströmen der atmosphärischen Luft durch Mündungen in dünner Wand. **Der Civilingenieur: Zeitschrift für das Ingenieurwesen**, p. 401–432, 1878.

FLUENT, A. ANSYS fluent theory guide 15.0. **ANSYS, Canonsburg, PA**, v. 33, 2013.

GOODE JR, W. D. et al. **Application of the HGSYSTEM/UF6 model to simulate atmospheric dispersion of UF6 releases from uranium enrichment plants**. [s.l.] Oak Ridge K-25 Site, 1995.

GRACE, H. P.; LAPPLE, C. E. **Discharge coefficients of small-diameter orifices and flow nozzles**. Transactions of the ASME, , 1951.

GUTERMUTH, M. F. Versuche über den Ausfluss des Wasserdampfes. **Zeitschrift des vereines deutscher Ingenieure**, p. 75–84, 1904.

HARLEY, J. C. et al. Gas flow in micro-channels. **Journal of Fluid Mechanics**, v. 284, p. 257–274, 1995.

HARTSHORN, L. The discharge of gases under high pressures. v. 32, p. 155–165, 1917.

HOLTZMANN, C. **Lehrbuch der theoretischen Mechanik**. Stuttgart: J. B. Metzler’schen Buchhandlung, 1861.

INB - INDÚSTRIAS NUCLEARES DO BRASIL. **Nuclear Fuel Cycle**. Disponível em: <http://www.inb.gov.br/en-us/Nossas-Atividades/nuclear-fuel-cycle>. Acesso em: 23 mar. 2022.

INC., A. ANSYS fluent user’s guide. **Ansys Fluent**, v. 15317, p. 2498, 2013.

JACKSON, R. A. The compressible discharge of air through small thick plate orifices. **Applied Scientific Research, Section A**, v. 13, p. 241–248, 1964a.

JACKSON, R. A. The compressible discharge of air through small thick plate orifices. **Applied Scientific Research, Section A**, v. 13, p. 241–248, 1964b.

KEMP, JR., J.; SREEKANTH, A. Preliminary results from an experimental investigation of nozzle wall boundary layer at Mach numbers ranging from 27 to 47. 1969.

KIRSHENBAUM, I. **THE PHYSICAL PROPERTIES OF URANIUM HEXA-FLUORIDE**. [s.l: s.n.].

KLEIJNEN, J. P. C. **Design and analysis of simulation experiments**. [s.l: s.n.]. v. 231

LOEPPKY, J. L.; SACKS, J.; WELCH, W. J. Choosing the sample size of a computer experiment: A practical guide. **Technometrics**, v. 51, n. 4, p. 366–376, 2009.

MAKHIJANI, A.; CHALMERS, L.; SMITH, B. Uranium enrichment. **Takoma Park, MD: Institute for Energy and Environmental Research for the Nuclear Policy Research Institute**, p. 1–47, 2004.

MALIK, M. N. et al. Mathematical modeling and computer simulation of transient flow in centrifuge cascade pipe network with optimizing techniques. **Computers and Mathematics with Applications**, v. 36, n. 4, p. 63–76, 1998.

METWALLY, M. Impacts of Short Tube Orifice Flow and Geometrical Parameters on Flow Discharge Coefficient Characteristics. **International Journal of Engineering Research & Technology**, v. 3, n. 1, p. 412–419, 2014.

MIGLIORINI, P. J. Modeling and Simulation of Gas Centrifuge Cascades for Enhancing the Efficiency of IAEA Safeguards. n. 434, p. 1–15, 2016.

MILLER, R. W. Flow measurement engineering handbook. 1983.

NILPUENG, K.; WONGWISES, S. Choked flow mechanism of HFC-134a flowing through short-tube orifices. **Experimental Thermal and Fluid Science**, v. 35, n. 2, p. 347–354, 2011.

OECD-NEA & IAEA. **Uranium 2020: Resources, Production and Demand. A Joint Report by the Nuclear Energy Agency and the International Atomic Energy AgencyNuclear Engineering International**. [s.l: s.n.].

OLIVER, G. D.; MILTON, H. T.; GRISARD, J. W. The Vapor Pressure and Critical Constants of Uranium Hexafluoride. **Journal of the American Chemical Society**, v. 75, n. 12, p. 2827–2829, 1953.

PALKIN, V. A. Optimization of a cascade with arbitrarily specified separation coefficients of the stages. **Atomic Energy**, v. 82, n. 4, p. 288–293, 1997.

PAULA, R. R. R. DE. **Modelagem matemática integral de sistemas de separação isotópica**. [s.l.] Tese (Doutorado) - Escola Politécnica da Universidade de São Paulo. Departamento de Engenharia Química, 2022.

PAULA, R. R. R. DE; MIGLIAVACCA, S. C. P.; GUARDANI, R. Study on the operating conditions of centrifuges and their individual separative power in a stage of an isotope separation cascade. **Annals of Nuclear Energy**, v. 177, p. 1–7, 2022.

PERRY, J. A. Critical flow through sharp-edged orifices. **Transactions of the ASME**, v. 71, n. 7, p. 757–763, 1949.

PIANTHONG, K. et al. Investigation and improvement of ejector refrigeration system using computational fluid dynamics technique. **Energy Conversion and Management**, v. 48, n. 9, p. 2556–2564, 2007.

POLING, B. E.; PRAUSNITZ, J. M.; O’CONNELL, J. P. **The Properties of GASES AND LIQUIDS**. 5. ed. [s.l.] McGraw-Hill Companies, Inc., 2001.

PONCELET, M. MÉCANIQUE PHYSIQUE ET EXPÉRIMENTALE. — Note sur les expériences de M. Pecqueur, relatives à l’écoulement de l’air dans les tubes, et sur d’autres expériences avec orifices en minces parois. **Comptes rendus hebdomadaires des séances de l’Académie des sciences**, v. 21, p. 178–198, 1845.

PORTOGHESE, C. C. P.; RODRIGUES, C. Comparative analysis of different approaches for theoretical simulation of ultracentrifuge isotopic separation cascades. **Separation Science and Technology**, v. 35, n. 5, p. 715–727, 2000.

REYNOLDS, O. **On the flow of gases**. Proceedings of the Manchester Literary and Philosophical Society. **Anais**...1885.

RICHARDSON, L. F. IX. The approximate arithmetical solution by finite differences of physical problems involving differential equations, with an application to the stresses in a masonry dam. **Philosophical Transactions of the Royal Society of London. Series A, Containing Papers of a Mathematical or Physical Character**, v. 210, n. 459–470, p. 307–357, 1910.

RICHARDSON, L. F.; GAUNT, J. A. VIII. The deferred approach to the limit. **Philosophical Transactions of the Royal Society of London. Series A, containing papers of a mathematical or physical character**, v. 226, n. 636–646, p. 299–361, 1927.

ROACHE, P. J. Perspective: A method for uniform reporting of grid refinement studies. **Journal of Fluids Engineering, Transactions of the ASME**, v. 116, n. 3, p. 405–413, 1994.

RODRIGUES, M. I.; IEMMA, A. F. **Experimental design and process optimization**.

RUPPEL, F. R. et al. **Application of a Kalman filter to UF6 gaseous diffusion plant freezer/sublimer systems**. [s.l.] Oak Ridge National Lab., 1992.

SAINT-VENANT, A. J. C. B. DE; WANTZEL, P. L. Mémoire et expériences sur l’écoulement de l’air, déterminé par des différences depression considérables. **J de I’École Polytechnique, Paris**, v. 16, p. 85–122, 1839.

SANTELER, D. J. Gasflow experiments in the transition region. **Journal of Vacuum Science & Technology A: Vacuum, Surfaces, and Films**, v. 12, p. 1744–1749, 1994.

SANTNER, T. J.; WILLIAMS, B. J.; NOTZ, W. I. **The Design and Analysis of Computer Experiments**. [s.l: s.n.].

SHAPIRO, A. H. **The dynamics and thermodynamics of compressible fluid flow**. 1th. ed. New York: The Ronald Press Company, 1953. v. 1

SREEKANTH, A. K. Transition flow through short circular tubes. **Physics of Fluids**, v. 8, n. 11, p. 1951–1956, 1965.

STODOLA, A. **Dampf- und Gasturbinen mit einem Anhang über die Aussichten der Wärmekraftmaschinen**. Sechste ed. Berlin, Heidelberg: [s.n.].

STOKES, G. G. Report on recent researches in hydrodynamics. **Brit. Assoc. Rep**, v. 1, n. 1, p. 20, 1846.

TIETJENS, O. G. Flow of gases at a rate exceeding the acoustic velocity. **Transactions of the ASME**, v. 53, n. 4, p. 49–58, 1931.

VAN DAM, E. R. et al. Maximin Latin hypercube designs in two dimensions. **Operations Research**, v. 55, n. 1, p. 158–169, 2007.

VIANA, F. A. C. A Tutorial on Latin Hypercube Design of Experiments. **Quality and Reliability Engineering International**, v. 32, n. 5, p. 1975–1985, 2016.

WEIR, A. J.; YORK, J. L.; MORRISON, R. B. Two- and three-dimensional flow of air through square-edged sonic orifices. **Transactions of the ASME**, v. 78, n. 3, p. 481–488, 1956.

WEISBACH, J. Versuche über die Ausströmung der Luft unter hohem Druck. **Der Civilingenieur: Zeitschrift für das Ingenieurwesen**, v. 12, p. 1–32, 1866.

WILDE, H. LXII. On the velocity with which air rushes into a vacuum, and on some phenomena attending the discharge of atmospheres of higher into atmospheres of lower density. **The London, Edinburgh, and Dublin Philosophical Magazine and Journal of Science**, v. 20, n. 127, p. 531–544, 29 dez. 1885.

WOOD, H. G. Analysis of Feed Effects on a Single-Stage Gas Centrifuge Cascade. **Separation Science and Technology**, v. 30, n. 13, p. 2631–2657, 1995.

ZEUNER, G. Resultate experimenteller Untersuchungen über das Ausströmen der Luft bei starkem Überdruck. **Der Civilingenieur: Zeitschrift für das Ingenieurwesen**, p. 1–12, 1874.

ZEUNER, G. **Technische Thermodynamik**. Dritte ed. Leipzig: Arthur Felix, 1905.